# Study of molecular clouds in the vicinity of supernova remnants as sources of very-high-energy gamma-ray emission

## Untersuchung von Molekülwolken in der Nähe von Supernova-Überresten als Quellen hochenergetischer Gammastrahlung

Der Naturwissenschaftlichen Fakultät
der Friedrich-Alexander-Universität Erlangen-Nürnberg
zur Erlangung des Doktorgrades Dr. rer. nat.

vorgelegt von
Stephanie Häffner
aus Nürnberg

Als Dissertation genehmigt
von der Naturwissenschaftlichen Fakultät
der Friedrich-Alexander-Universität Erlangen-Nürnberg
Tag der mündlichen Prüfung: 7. November 2014

Vorsitzender des Promotionorgans: Prof. Johannes Barth, PhD

Gutachter/in: Prof. Dr. Christian Stegmann
Prof. Dr. Gisela Anton

## Abstract

H.E.S.S. is an imaging atmospheric Cherenkov telescope system for studies of cosmic $\gamma$-ray sources. The H.E.S.S. experiment provides with the H.E.S.S. Galactic Plane Survey the largest data set for such sources in the TeV energy band for the inner Galactic plane, which is very well suitable for population studies.

This thesis presents studies of molecular clouds in the vicinity of supernova remnants as sources of very-high-energy $\gamma$-ray emission. $\gamma$-ray emitting molecular clouds near supernova remnants provide a good environment to test the propagation of high-energy particles through the insterstellar medium as well as to probe the acceleration of hadrons at supernova remnants. The studies are focusing on the molecular clouds of the Galactic Ring Survey, which is the most comprehensive public catalogue of molecular clouds with estimated distances and masses. The spatial coincidence of molecular clouds from the Galactic Ring Survey with $\gamma$-ray emission in the H.E.S.S. Galactic Plane Survey is analysed in this thesis. The level of random coincidences is obtained with simulations of molecular cloud populations. It has been demonstrated that most molecular clouds of the Galactic Ring Survey are only spatially coincident by chance with $\gamma$-ray emission. However, the fraction of spatially coincident clouds with $3.5 < \log_{10}[(M_{\mathrm{MC}}/d_{\mathrm{MC}}^2)/(\mathrm{M}_\odot/\mathrm{kpc}^2)] < 4$ is found to be substantially larger than the level of random coincidence, with $M_{\mathrm{MC}}$ denoting the mass of the cloud and $d_{\mathrm{MC}}$ its distance to Earth. However, this enhancement cannot established as significant connection between the molecular clouds of the Galactic Ring Survey and the emission in the H.E.S.S. Galactic Plane Survey since the probability to get the fraction of spatially coincident clouds due to random coincidences is still $3.9 \cdot 10^{-3}$, $5.1 \cdot 10^{-4}$ and $4.5 \cdot 10^{-4}$ tested on $\gamma$-ray signifcance maps generated with correlation radii of 0.2°, 0.3° and 0.4°, respectively. Therefore, the derived results can only be interpreted as a hint for $\gamma$-ray emitting clouds in the vicinity of supernova remnants.

Furthermore, this thesis presents a systematic search for regions populated with molecular clouds near supernova remnants which are potentially detectable with H.E.S.S. The search-results emphasise regions with more than one potentially detectable cloud as well as regions around supernova remnants with well known properties. In addition, the study of molecular clouds near supernova remnants resulted in a constraint on the normalisation of the diffusion coefficient at 10 GeV to be smaller than $10^{28}\,\mathrm{cm}^{-2}\,\mathrm{s}^{-1}$, even if it was not possible to derive a limit on the energy dependence of the diffusion coefficient.

The surrounding of the supernova remnant 3C391 is one interesting region with potentially detectable molecular clouds. The analysis of about 80 hours of observation with the H.E.S.S. experiment reveals significant $\gamma$-ray emission from that region. The morphological and spectral properties of the observed emission are discussed. The scenario of a supernova remnant/molecular cloud association is tested. However, it is not possible to establish this scenario due to the underlying large-scale diffusive $\gamma$-ray emission and the adjacent source HESS J1848–018.

## Kurzfassung

H.E.S.S. ist ein System von abbildenden atmosphärischen Cherenkov-Teleskopen zum Nachweis von Quellen kosmischer Gammastrahlung. Das H.E.S.S. Experiment besitzt mit dem H.E.S.S. Galactic Plane Survey den größten zusammenhängenden Datensatz im TeV Energieband für den inneren Bereich der Galaktischen Ebene. Dieser eignet sich hervorragend für Populations-Studien.
In der vorliegenden Dissertation werden die Ergebnisse verschiedene Untersuchungen zu Molekülwolken in der Umgebung von Supernova-Überresten als Quellen hochenergetischer Gammastrahlung vorgelegt. Gammastrahlungsemittierende Molekülwolken bieten eine sehr gute Möglichkeit, um Informationen über die Ausbreitung hochenergetischer Teilchen durch das interstellare Medium sowie über die Beschleunigung von Hadronen in Supernova-Überresten zu gewinnen. Die Untersuchungen dieser Arbeit konzentrieren sich hauptsächlich auf die Molekülwolken des Galactic Ring Survey, dem umfassendsten veröffentlichten Katalog von Molekülwolken mit berechneten Entfernungen und Massen.
In dieser Arbeit wird die räumliche Koinzidenz der Molekülwolken des Galactic Ring Survey mit Gammastrahlung im H.E.S.S. Galactic Plane Survey untersucht. Der Anteil an Zufallskoinzidenzen wird mit Hilfe von simulierten Molekülwolkenpopulationen ermittelt. Ein erhöhter Anteil an räumlich konzidenten Wolken wird in dem Bereich $3.5 < \log_{10}[(M_{\mathrm{MC}}/d_{\mathrm{MC}}^2)/(\mathrm{M}_\odot/\mathrm{kpc}^2)] < 4$ beobachtet, wobei $M_{\mathrm{MC}}$ die Masse der Molekülwolken und $d_{\mathrm{MC}}$ ihre Distanz bezeichnen. Es kann jedoch kein signifikanter Zusammenhang zwischen diesen Wolken und der beobachteten Gammastrahlung hergestellt werden, da die Wahrscheinlichkeiten, dass das beobachtete Verhältnis von räumlich koinzidenten Wolken von Zufallskoinzidenzen auf Signifikanzkarten mit Korrelationsradien von 0.2°, 0.3° und 0.4° verursacht wird, $3.9 \cdot 10^{-3}$, $5.1 \cdot 10^{-4}$, beziehungsweise $4.5 \cdot 10^{-4}$ betragen. Diese Ergebnis kann aber als Hinweis auf Gammastrahlungsemission von Wolken in der Nähe von Supernova-Überresten interpretiert werden.
Des Weiteren wird in dieser Dissertation eine Suche nach Regionen vorgestellt, in denen sich mit H.E.S.S. detektierbare Molekülwolken in der Nähe von Supernova-Überresten befinden. Die Ergebnisse dieser Suche heben Regionen mit mehr als einer möglichen nachweisbaren Wolke hervor sowie Regionen um Supernova-Überreste, die gut abgeschätzte Eigenschaften haben. Durch die Untersuchung von Molekülwolken in der Umgebung von Supernova-Überresten konnte außerdem mit Hilfe von simulierten Populationen eine obere Grenze auf die durchschnittliche Normalisierung des Diffusionkoeffizienten bei 10 GeV von $10^{28}\,\mathrm{cm}^{-2}\,\mathrm{s}^{-1}$ bestimmt werden. Die Energieabhängigkeit des Diffusionskoeffizienten für hochenergetische Teilchen kann leider nicht mit der hier vorgestellten Strategie beschränkt werden.
Die Umgebung des Supernova-Überrestes 3C391 ist eine der Regionen, die bei der Suche nach möglichen nachweisbaren Molekülwolken aufgezeigt wurde. Die Analyse von 80 Stunden an Beobachtungsdaten des H.E.S.S. Experimentes zeigt hier signifikante Gammastrahlung. Die morphologischen und spektralen Eigenschaften der Emission werden in dieser Arbeit diskutiert, ebenso wie das Emissionszenario einer Molekülwolke in der Umgebung von 3C391. Eine Verknüpfung der beobachteten Emission mit einer Supernova-Überrest/Molekülwolken-Assoziation ist aufgrund großräumiger, diffuser Gammastrahlung und der benachbarten Quelle HESS J1848–018 nicht möglich.

# Contents

CHAPTER 1

# Introduction

Victor Hess discovered in the 1910s the cosmic radiation explaining the rising radiation at increasing altitudes in the atmosphere (Hess, 1912). This radiation was named "cosmic rays" in the 1920s by Robert A. Millikan. At that time mainly particles such as atomic nuclei, protons and electrons were examined and the compositon of the cosmic rays unknown. In the first half of the 20th century many discoveries of previous unknown particles were made by observing cosmic rays with cloud chamber experiments. With this method Anderson (1933) discovered the positron, Anderson & Neddermeyer (1936) the muon as well as Rochester & Butler (1947) the pion and kaon. Even though the second half of the 20th century saw the dawn of accelerator physics and the development of today's powerful particle accelerators, such as the LHC[1], which achieves proton beam energies up to a few TeV, the cosmic-ray observations reveal particles with energies up to more than $10^{20}$ eV.

Up to now the cosmic-ray energy spectrum and composition has been measured to a very high accuracy over more than twelve decades in energy. Cosmic rays comprise, as observed at the top of the Earth's atmosphere, about 87 % protons, 12 % helium nuclei, 2 % electrons and 1 % heavier nuclei (Longair, 2011). The cosmic-ray energy spectrum can be described by a power law with a spectral index $\approx -2.7$ over a wide range of energies. At energies above $10^{13}$ eV there are two distinct features with changes in the spectral index, the "knee" at $10^{15} - 10^{16}$ eV and the "ankle" around $10^{18.5}$ eV.

Cosmic rays up to energies of about $10^{15} - 10^{16}$ eV are assumed to be of Galactic origin. In this picture, the knee indicates the maximum energy to which particles are accelerated within our Galaxy. Hence, the most common interpretation of the knee is the transition between a Galactic and extragalactic component, since, for the exemplary case of a proton with an energy of $10^{18}$ eV moving in the Galactic magnetic field with typical values of about 5 $\mu$G, the gyro-radius[2] is larger than the thickness of the Galactic disk and the particles are thus no longer confined within the Galaxy, see, e.g., Longair (2011).

The origin of cosmic rays has not been determined yet, but since the 1930s supernova remnants have been considered as prime candidates for sources of the Galactic cosmic-ray component (Baade & Zwicky, 1934). Meanwhile, it is not clear which type of particles are

[1] **L**arge **H**adron **C**ollider

[2] also known as Larmor radius or cyclotron radius

accelerated at supernova remnants: mainly leptons (electrons and positrons) or hadrons (mainly protons) and with which ratio. Observations of non-thermal X-ray emission from supernova remnants reveal leptons with energies up to 100 TeV. Today's imaging atmospheric Cherenkov telescope systems such as H.E.S.S.[3], MAGIC[4] and VERITAS[5] detected $\gamma$-ray emission in the very-high-energy domain (energies $\geq 100$ GeV) from more than ten supernova remnants. For most of the supernova remnants it is not clear whether the observed $\gamma$-ray emission is produced by accelerated leptons or hadrons. Leptons can produce $\gamma$-ray emission via inverse Compton scattering off photon fields such as starlight or the cosmic microwave background. Accelerated hadrons can interact with the ambient medium and produce $\gamma$-rays via proton-proton collision and subsequent neutral pion decay, $\pi^0 \rightarrow \gamma\gamma$.

Recently, the *Fermi*-LAT[6] Collaboration reported the first detection of pion-decay signatures in the GeV $\gamma$-ray emission of the supernova remnants W44 and IC 443 (Ackermann et al., 2013). This signature in the $\gamma$-ray emission from W44 in the GeV regime was confirmend by observations with *AGILE*[7] (Cardillo et al., 2014). The detection of GeV $\gamma$-ray emission outside the supernova remnant W44 coincident with ambient molecular clouds strengthens these results (Uchiyama et al., 2012). Molecular clouds near supernova remnants provide a suitable environment to probe hadronic acceleration in supernova remnants, as $\gamma$-ray emission coincident with molecular clouds proves the hadronic origin of the emission. Leptonic emisson processes, except possibly bremsstrahlung in the Galactic centre region, are negligible regarding the $\gamma$-ray emission of clouds in the TeV energy band.

Apart from the possibility to probe hadronic acceleration in supernova remnants, $\gamma$-ray emitting molecular clouds close to supernova remnants are also good laboratories to study the propagation properties of high-energy particles as extensively done for the region around the supernova remnant W28. The detection of TeV $\gamma$-ray emission from the W28 region coincident with molecular clouds was reported by the H.E.S.S. Collaboration (Aharonian et al., 2008b). The emission is visible in three distinct regions: two emission regions are coincident with molecular clouds offset from the supernova remnant, one is coincident with a molecular clouds in the shock region. The common explanation for the emission are hadrons accelerated in the shock of a supernova remnant and afterwards escaped from the acceleration site, as illustrated in Fig. 1.1. These high-energy particles then can interact with molecular clouds in the vicinity of the supernova remnant and produce $\gamma$-ray emission due to proton-proton interaction and subsequent pion decay. The very-high-energy $\gamma$-ray emission can be detected with ground based imaging Cherenkov telescopes as explained in Chapter 4. Molecular clouds with typical densities of a few hundred molecules per cm$^3$ provide an increased amount of target material for the accelerated particles, which may give rise to $\gamma$-ray emission via the neutral pion decay. The emission in the W28 region at the shock of the supernova remnant and offset is also detected in the GeV energy regime with the Fermi-LAT instrument (Abdo et al., 2010; Hanabata et al., 2014). The W28 region is the best studied region for constraining the propagation properties of high-energy particles traversing magnetic turbulences in the interstellar medium. The motion of charged particles due to scattering off magnetic irregularities can be described by diffusion as discussed, e.g., in Longair (2011).

[3] **H**igh **E**nergy **S**tereoscopic **S**ystem
[4] **M**ajor **A**tmospheric **G**amma-Ray **I**maging **C**herenkov Telescopes
[5] **V**ery **E**nergetic **R**adiation **I**maging **T**elescope **A**rray **S**ystem
[6] **L**arge **A**rea **T**elescope
[7] **A**stro-rivelatore **G**amma a **I**mmagini **LE**ggero

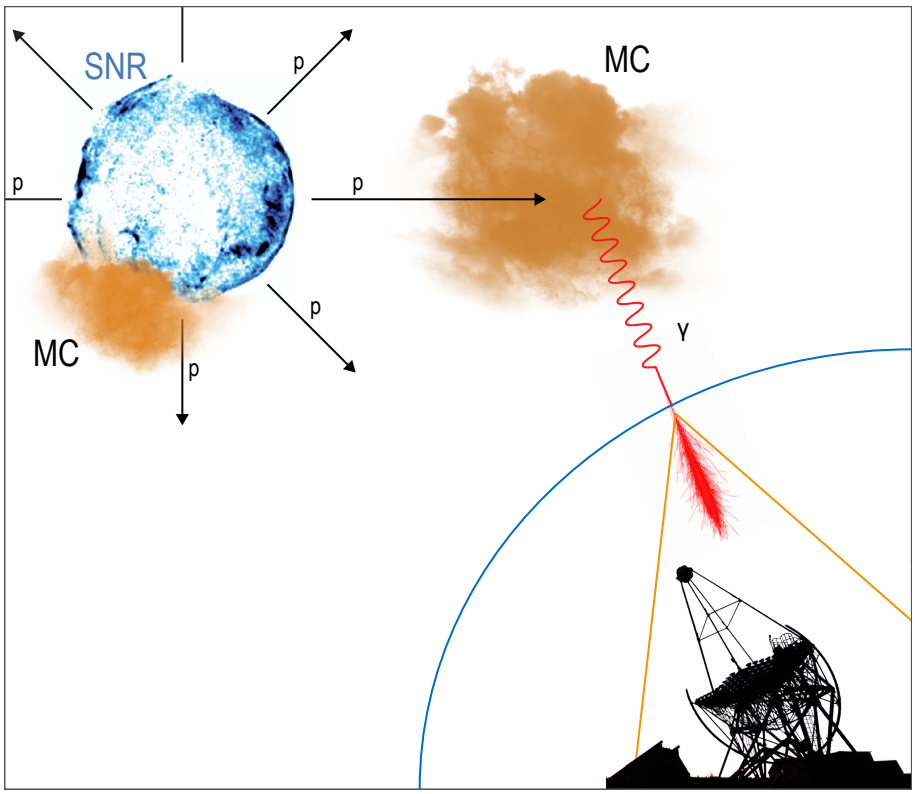


**Figure 1.1:** Illustrative sketch of $\gamma$-ray emitting molecular clouds (MCs) near a supernova remnant (SNR). The shell of the supernova remnant is extracted from the *Chandra* observation with ID 3837 and the image of the telescope is credited to F. Acero and H.Gast.

The application of isotropic diffusion models to the W28 region (Gabici et al., 2010; Li & Chen, 2010; Ohira et al., 2011; Yan et al., 2012) reveals that the diffusion coefficient at 10 GeV is suppressed by more than one order of magnitude compared to the Galactic average value of $\approx 10^{28}\,\mathrm{cm}^2\,\mathrm{s}^{-1}$ (Strong et al., 2007). Numerical simulations of the propagation of particles with energies of about 100 TeV − 10 PeV predict anisotropic diffusion with some filamentary structures on scales up to more than hundred parsec around a given cosmic ray source (Giacinti et al., 2012). The application of an anisotropic diffusion model to the W28 region (Nava & Gabici, 2013) resulted in a diffusion coefficient in the order of $10^{28}\,\mathrm{cm}^2\,\mathrm{s}^{-1}$, whereas an isotropic diffusion coefficient is one and a half orders of magnitude smaller. To get further insights into the propagation of high-energy particles studies of further supernova remnant/molecular cloud associations are mandatory.

With its comprehensive survey of the Galactic plane, the H.E.S.S. experiment povides with the H.E.S.S. Galactic Plane Survey the largest connected data set in the TeV band, covering more than 120° in longitude of the Galactic plane. The data set is thus very well suited for population studies in general. In this work, the H.E.S.S. Galactic Plane Survey, along with molecular clouds from the the Galactic Ring Survey (Jackson et al., 2006), is used to study $\gamma$-ray emitting molecular clouds. The Galactic Ring Survey covers the region between 18° and 56° Galactic longitude and between −1.0° and 1.0° Galactic lattitude. Distances and masses for about 750 molecular clouds were derived (Rathborne et al., 2009; Roman-Duval et al., 2009, 2010). These molecular clouds are used in this work to explore various aspects of molecular clouds near supernova remnants as sources for very-high-energy $\gamma$-ray emission.

This work is structured as follows: an introduction to supernova remnants, their evolution and our current notion of mechanisms of particle acceleration at shock fronts of supernova remnants is given in Chapter 2. $\gamma$-ray emission processes, the hadronic scenario via pion decay as well as leptonic scenarios via inverse Compton scattering and bremsstrahlung, are outlined here.
Chapter 3 introduces the general properties of molecular clouds and three scenarios for $\gamma$-ray emitting molecular clouds: passive molecular clouds embedded in the so-called "cosmic-ray sea", molecular clouds interacting with a shock of a supernova remnant, and molecular clouds offset from the supernova remnant illuminated by particles escaping from the remnant.
The H.E.S.S. experiment and the H.E.S.S. Galactic Plane Survey, used in this work to study $\gamma$-ray emitting molecular clouds, are introduced in Chapter 4.
The method and results of testing spatial coincidence of the molecular clouds of the Galactic Ring Survey with $\gamma$-ray emission in the H.E.S.S. Galactic Plane Survey are presented in Chapter 5. The level of random coincidences is estimated with simulated molecular clouds populations.
In Chapter 6 the search strategy for regions populated with potentially detectable $\gamma$-ray emitting molecular clouds is introduced. The results of the search as well as a constraint on the diffusion coefficient are presented.
One of those regions, that were revealed as particulary promising by the search in Chapter 6, is the region around the supernova remnant 3C391. A closer look at that region is presented in Chapter 7 using observations of the H.E.S.S. experiment as well as radio observations from the Galactic Ring Survey.
A summary and outlook of this work is given in Chapter 8.

CHAPTER 2

# Supernova remnants

As introduced in Chapter 1 supernova remnants (SNRs) are prime candidates to be sources of cosmic rays. In this work, $\gamma$-ray emitting molecular clouds near supernova remnants as sources of very-high-energy $\gamma$-ray emission are explored. Therefore, an introduction to supernova remnants is given in this Chapter. Section 2.1 briefly summarises which informations on accelerated particles can be achieved from the observation of supernova remnants. The Sections 2.2 and 2.3 outline the evolution of supernova remnants and acceleration processes at the shock front of supernova remnants. Since $\gamma$-ray emission can be produced both by accelerated leptons and hadrons, the corresponding radiation processes are described in Section 2.4.

## 2.1 Observation of supernova remnants

Supernova remnants are visible in different energy bands across the electromagnetic spectrum, from the radio band up to TeV $\gamma$ rays. More than 300 supernova remnants have been discovered in the radio band (see, e.g., Green (2009); Ferrand & Safi-Harb (2012)). A prominent example is the remnant of the historical supernova 1006 shown in Fig. 2.1. A composed image of radio, optical and X-ray observations is shown in Fig. 2.1(a) along with the TeV $\gamma$-ray sky map in Fig. 2.1(b). The TeV sky map shows excess counts derived after background subtraction. The dashed circles in Fig. 2.1(b) represents the radio size of the supernova remnant. The TeV emission from this remnant is spatially coincident with the regions with the strongest X-ray emission.
The nonthermal radio spectra of supernov remnants are interpreted as synchroton emission from relativistic electrons accelerated at the shock of the supernova remnant. The polarisation of the radio synchroton emission gives information about the magnetic field structure in the remnant. The observed X-ray emission consists of non-thermal and thermal emission. The thermal component stems from the heated gas within the shock, whereas the non-thermal emission is produced by electrons in the energy range $(10 - 100)$ TeV. Narrow filaments observed in X-rays indicate high magnetic fields near the shock front. Both the non-thermal X-ray and radio emission are of leptonic origin. The observed GeV and TeV emission can

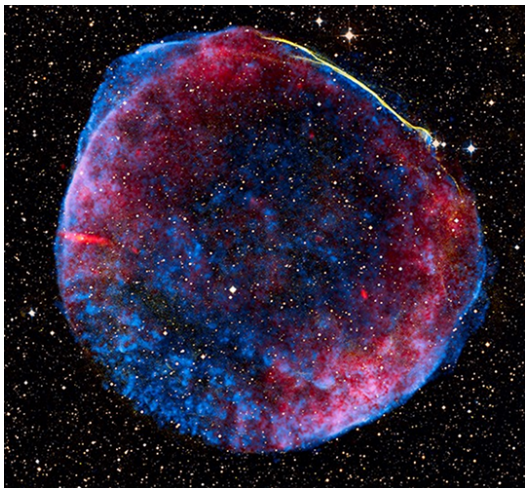

(a) Composed image of observations of the remnant of supernova 1006. The radio data are coloured in red, optical in yellow and the X-ray data in blue. Image credit: NASA, ESA, Zolt Levay (STScI).

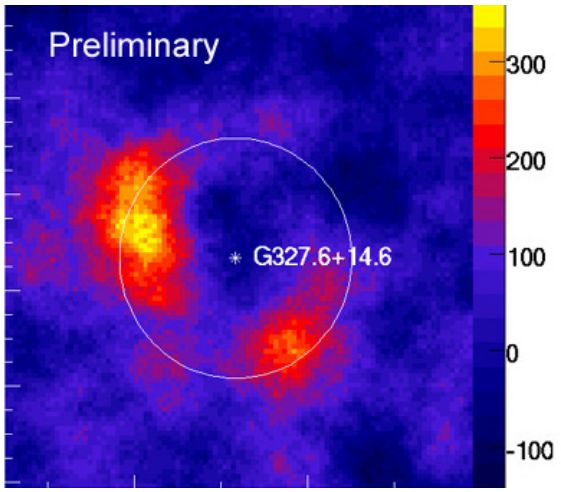


(b) Skymap with TeV $\gamma$-ray excess counts of the supernova 1006 obtained with the H.E.S.S. experiment (H.E.S.S. collaboration, 2008).

**Figure 2.1:** Observation of the remnant of supernova 1006 in the radio, optical, X-ray and TeV energy band.

be produced either by leptons due to inverse Compton scattering and bremsstrahlung or by hadrons via pion decay. Observations of different remnants show that particles are accelerated in the free expansion phase and the Sedov phase. For a more detailed discussion and review of recent observations see Helder et al. (2012).

## 2.2 Evolution of supernova remnants

The fate of a star - both its evolution and death - depends on its mass. Massive stars ($M \geq 8M_{\odot}$, with the solar mass $M_{\odot}$) typically end in a supernova explosion triggered by the collapse of the iron core after the star burned all the nuclear energy and the gravitational pressure surpasses the radiation pressure. The implosion of the core leads to a neutron star or black hole as leftover. These supernovae are also called core-collapse supernovae. However, less heavy stars that have already reached the state of a white dwarf can also explode in a supernova if they accrete material from a massive companion star until reaching the Chandrasekhar mass of about $1.3\,\mathrm{M}_{\odot}$ and fulfilling the conditions for a thermonuclear explosion. Even though these two mechanisms leading to a supernova explosion are different, the typical energy released in a supernova explosion $E_{\mathrm{SN}}$ is in the order of $10^{51}$ erg.
After the explosion the stellar ejecta expand into the ambient medium and form a so-called supernova remnant. Typical velocities are $\mathrm{v}_{\mathrm{eject}} \approx 10^4\,\mathrm{km\,s^{-1}}$ and due to the supersonic speed of the ejecta a shock front is formed. The shock front sweeps up the ambient medium during the expansion and the shock velocity of the foward shock decreases. As a consequence a second shock, also called reverse shock, is formed. Observations of supernova remnants in different energy bands from radio to $\gamma$ rays show that particles get accelerated at the shock fronts during different stages in the evolution of an supernova remnant. The potential acceleration mechanism via diffusive shock acceleration is described in Section 2.3.

The simplified evolution of a core-collapse supernova remnant can be broken down to four phases, as discussed in Woltjer (1972) and Padmanabhan (2001).

**Phase I**: This phase is usually called *free expansion phase*. The mass $M_{\mathrm{swp}}$ swept up by the shock from the ambient medium is negligible and the shock expands freely into a homogenous medium as long as $M_{\mathrm{swp}} \ll (4\pi/3)\rho_{ISM}R_{\mathrm{s}}^3$ is fulfilled. $\rho_{\mathrm{ISM}}$ is the density of the ambient medium and $R_s$ is the foward shock radius. The initial velocity $\mathrm{v}_0$ of the ejected mass $M_{\mathrm{ej}}$ after the explosion is

$$\mathrm{v}_0 = \sqrt{\frac{2E_{\mathrm{SN}}}{M_{\mathrm{ej}}}} = 10^9\,\mathrm{cms}^{-1}\left(\frac{E_{\mathrm{SN}}}{10^{51}\,\mathrm{erg}}\right)^{1/2}\left(\frac{M_{\mathrm{ej}}}{1\,\mathrm{M}_\odot}\right)^{-1/2}, \tag{2.1}$$

larger than the speed of sound in the medium. Therefore, a shock front is formed. The ejected mass $M_{\mathrm{ej}}$ is about the same as the swept-up mass. The radius increases linearly with time until the swept-up mass dominates the expansion process. The characteristic timescale $t_{\mathrm{Sedov}}$ of this phase until the beginning of the following *Sedov phase*[1] and the radius $r_{\mathrm{Sedov}}$ of the remnant depend on the density of the ambient medium $\rho_{\mathrm{ISM}}$. The free expansion phase ends after the characteristic timescale of

$$t_{\mathrm{Sedov}} \simeq 200\,\mathrm{yr}\left(\frac{E_{\mathrm{SN}}}{10^{51}\,\mathrm{erg}}\right)^{-1/2}\left(\frac{\rho_{\mathrm{ISM}}}{10^{-24}\mathrm{gm\,cm}^{-3}}\right)^{-1/3} \tag{2.2}$$

with a radius of the supernova remnant of

$$r_{\mathrm{Sedov}} = \left(\frac{3M_{\mathrm{ej}}}{4\pi\rho_{\mathrm{ISM}}}\right)^{1/3} = 2.1\,\mathrm{pc}\left(\frac{M_{\mathrm{ej}}}{1\,\mathrm{M}_\odot}\right)\left(\frac{n_0}{1\,\mathrm{cm}^{-3}}\right)^{-1/3}, \tag{2.3}$$

with the number density $n_0$ of the ambient medium.
**Phase II**: This phase is called *Sedov Phase*. Radiative losses $\mathrm{d}E/\mathrm{d}t$ are still negligible since $\int(\mathrm{d}E/\mathrm{d}t)\mathrm{d}t \ll E_{\mathrm{SN}}$. Kinetic and thermal energies are conserved. The radius of the supernova remnant evolves as

$$r \simeq 0.3\,\mathrm{pc}\left(\frac{E_{\mathrm{SN}}}{10^{51}\,\mathrm{erg}}\right)^{1/5}\left(\frac{n_0}{1\,\mathrm{cm}^{-3}}\right)^{-1/5}\left(\frac{t}{\mathrm{yr}}\right)^{2/5}. \tag{2.4}$$

The shock velocity $\mathrm{v}_{\mathrm{shock}}$ decreases with increasing radius

$$\mathrm{v}_{\mathrm{shock}} \simeq 5000\,\mathrm{km\,s}^{-1}\left(\frac{r}{2\,\mathrm{pc}}\right)^{-3}\frac{E_{\mathrm{SN}}}{10^{51}\,\mathrm{erg}}\left(\frac{n_0}{1\,\mathrm{cm}^{-3}}\right)^{-1} \tag{2.5}$$

and the heated gas reaches temperatures of about $3\cdot10^6\,\mathrm{K}$. The emitted thermal radiation is visible in X-rays.
At the end of this phase the shock velocity is slowed down to $\approx 200\,\mathrm{km\,s}^{-1}$ and the radiative losses dominate. The outer shell of the shock decelerates first, allowing the inner material to catch up. During the deceleration process a shock wave at the inner edge is formed that leads to a heating of the matter in the outer shell. The transition between this phase and the *radiation phase* afterwards occurs after a time

$$t_{\mathrm{rad}} = 3\cdot10^4\left(\frac{T}{10^6\mathrm{K}}\right)^{-5/6}\left(\frac{E_{\mathrm{SN}}}{10^{51}\,\mathrm{erg}}\right)^{1/3}\left(\frac{n_0}{1\,\mathrm{cm}^{-3}}\right)^{-1/3}\mathrm{yr}. \tag{2.6}$$

[1] named after the russian physicist Leonid I. Sedov

**Table 2.1:** Characteristic values for the radius $r$, shock velocity v and swept-up mass $M_{\mathrm{swp}}$ for the transition between the different phases of the evolution of an supernova remnant. These values are taken from Woltjer (1972).

| Transition between phases | $t$ [yr] | $r$ [pc] | v [$\mathrm{km\,s^{-1}}$] | $M_{\mathrm{swp}}$ [$M_\odot$] |
|---|---|---|---|---|
| I - II | 90 | 0.9 | $10^4$ | 0.2 |
| II - III | $22 \cdot 10^3$ | 11 | 200 | 180 |
| III - IV | $750 \cdot 10^3$ | 30 | 10 | 3600 |

A more detailed description of the evolution during the non-radiative stages (phases I and II) is given in Truelove & McKee (1999).

**Phase III** ($t > t_{\mathrm{rad}}$): The radiation cooling is dominant and the temperature of the matter behind the shock decreases. The radial momentum of the shell is nearly constant and the expanding shock piles up interstellar gas comparable to a snow plough piling up snow. The name *snow plough phase* refers to this. The radius increases with $R(t) \propto t^{1/4}$.

**Phase IV**: In this last phase the shock velocity drops to $(10 - 100\,\mathrm{km\,s^{-1}})$ in about $(1 - 5) \cdot 10^5\,\mathrm{yr}$. The remnant loses its structure and the accumulated matter disperses into the interstellar medium.

Typical values for the phase duration, radius of the remnant, shock velocity and swept-up material for this simplified picture for a homogenous environment are summarised in Table 2.1.

## 2.3 Particle acceleration at shock fronts of supernova remnants

Detection of non-thermal emission from supernova remnants from radio to TeV energy range established them as sites of powerful particle acceleration. The proposed acceleration mechanism is diffusive shock acceleration at the shock front of the supernova remnant. The general concept was developed contemporaneously in the late 1970s by Krymskii (1977), Axford et al. (1977), Bell (1978a,b) and Blandford & Ostriker (1978) as first-order Fermi acceleration. The idea is that particles cross the shock of the supernova remnant many times, bounce off magnetic turbulences in the up- and down-stream regions of the shock and gain energy. Fermi (1949) originally proposed the acceleration of cosmic rays by collisions with randomly moving magnetic fields in the interstellar space of the galaxy. For historically reasons, in Section 2.3.1 the so-called “second-order” Fermi acceleration is discussed. The diffusive shock acceleration and “first-order” Fermi acceleration occuring at strong shocks are introduced in Secion 2.3.2.

### 2.3.1 Second-order Fermi acceleration

The discussion of Fermi’s approach presented here is based on Longair (2011). Fermi suggested in 1949 that particles could collide with magnetic irregularities in the interstellar

medium, in the following just called magnetic mirrors. These mirrors are moving randomly with a typical velocity $v_M$. The mirror mass is much larger than the particle's mass and simply assumed to be infinite for the calculation of the collision between a particle and a moving mirror. The energy $E'$ of the particle in the frame of the moving cloud is

$$E' = \gamma(E + p v_M \cos\theta), \tag{2.7}$$

where $\gamma = 1/\sqrt{1 - v_M^2/c^2}$, $c$ is the speed of light and $\theta$ is the angle between the particle trajectory and the velocity direction of the mirror. The x-component of the particle's momentum $p$ in the mirror frame is

$$p'_x = p' \cdot \cos\theta' = \gamma\left(p\cos\theta + \frac{v_M \cdot E}{c^2}\right). \tag{2.8}$$

Energy and momentum are conserved during the collision, therefore $E'_{before} = E'_{after}$ and $p'_x = -p'_x$. The energy of the particle after the collision in the observer frame is

$$E'' = \gamma(E' + v_M \cdot p'_x) = \gamma^2 \cdot E\left[1 + \frac{2 \cdot v_M \cdot v}{c^2} + \left(\frac{v_M}{c}\right)\right] \tag{2.9}$$

with the particle's velocity v. The average energy gain per collision for the particle after expanding Eq. 2.9 to second order in $v_M/c$ and averaging over $\theta$ for all angles between 0 and $\pi$ reads

$$\left\langle \frac{\Delta E}{E} \right\rangle = \frac{8}{3}\left(\frac{v_M}{c}\right)^2. \tag{2.10}$$

This leads to an energy gain of second order in $v_M/c$ and to a power-law energy spectrum of accelerated particles which is observed from non-thermal sources. But Fermi's proposed acceleration mechanism is not efficient for random velocities of interstellar clouds with $v_M/c \leq 10^{-4}$. Furthermore the mean free path of cosmic rays in the interstellar medium is $\approx 0.1$ pc. This results in only a few collisions per year and, therefore, the energy gain is too slow to explain the cosmic-ray energies observed.

### 2.3.2 First-order Fermi acceleration

The diffusive acceleration in strong shock waves as proposed by Krymskii (1977), Axford et al. (1977), Bell (1978a), Bell (1978b) and Blandford & Ostriker (1978) results in an energy gain first order of the shock velocity $v_s$ and gives an energy spectrum with power-law form with a spectral index $\approx -2$.
The discussion of the ansatz of Bell (1978a) in the following paragraphs is based on Longair (2011) and illustrated in Fig. 2.2. The acceleration of particles takes place at the shock front that is formed in a supernova explosion. The shock is represented by the dashed line in Fig. 2.2. The fluid velocities before and after a hydrodynamical shock, moving with velocity $v_s$, are different. The particles are assumed to propagate with a speed much larger than the shock velocity $v_p \gg v_s$ and take no notice of the shock itself because their gyro radius is much larger than the shock thickness. The upstream fluid velocity is $v_{up} \approx v_s$ in the frame of the shock and the downstream velocity is $v_{down} = v_s/4$ for strong shocks as illustrated in Fig. 2.2(b). This dependency follows from the continuity equation

$$\rho_{up} \cdot v_{up} = \rho_{up} \cdot v_s = \rho_{down} \cdot v_{down}. \tag{2.11}$$

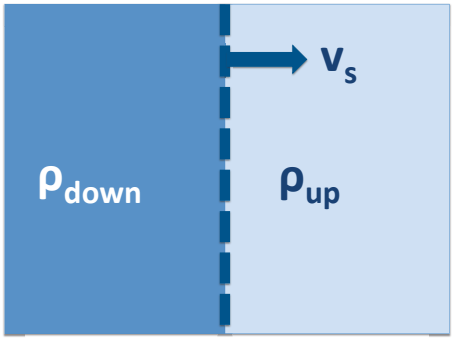


(a) A strong shock is moving with velocity $v_s$ through a medium with density $\rho_{up}$. Behind the shock in the downstream region the medium has the density $\rho_{down}$.

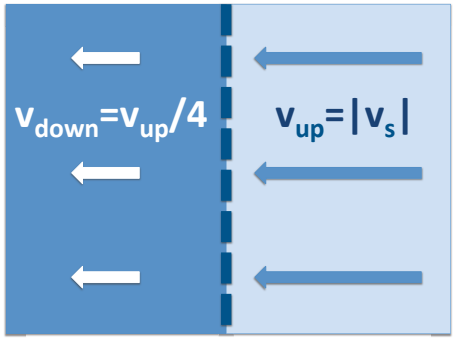


(b) Reference system of the shock.

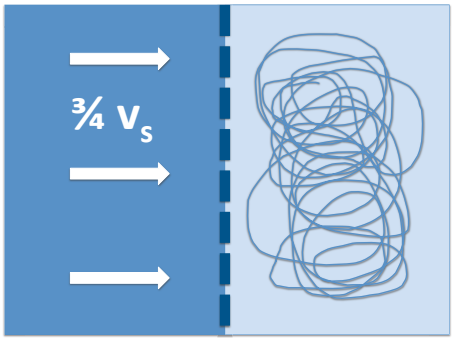


(c) Reference system of the upstreaming gas.

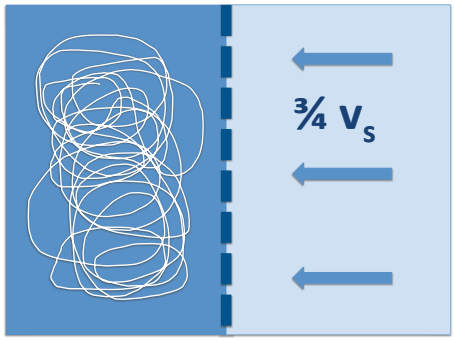


(d) Reference system of the downstreaming gas.

**Figure 2.2:** The dynamics of high-energy particles in the vicinity of a strong shock. The figure is adapted from Longair (2011).

$\rho_{up}$ and $\rho_{down}$ are the up- and downstream densities and, in the case of strong shock, $\rho_{up}/\rho_{down} = (\tau+1)/(\tau-1)$ with $\tau$ denoting the ratio of the specific heat capacities. For a fully ionised or monoatomic gas is $\tau = 5/3$ and, hence, $v_{down} = v_s/4$.
In the reference system of the upstream gas (see Fig. 2.2(c) ), the particle velocity distribution is isotropic and the downstream gas is moving with $3v_s/4$. Particles cross the shock and gain energy by scattering head-on off the downstream fluid. After the scattering the velocity distribution is now isotropic in the frame of the downstream fluid and the upstream fluid has a relative velocity of $3v_s/4$ in the system of the downstream fluid as illustrated in Fig. 2.2(d). After crossing the shock the particles bounce off the upstream fluid and again gain energy. Therefore, the particles gain an amount of energy $\propto v_s/c$ with each crossing of the shock. Performing a Lorentz transformation between the different systems and averaging over all angles gives a fractional energy increase per shock crossing of

$$\left\langle \frac{\Delta E}{E} \right\rangle = \frac{4}{3}\left(\frac{v_s}{c}\right). \tag{2.12}$$

The approach discussed above shows that particles gain energy while crossing the shock and scattering off magnetic turbulences in the up- and downstream region. Bell (1978a) proposed the backreaction of the accelerated charged cosmic rays as source for the magnetic turbulences by resonant Alfvén waves. Alfvén waves are generated by particles with velocities larger than the critical speed $v_A \approx \frac{B}{\sqrt{4\pi\rho}}$ in a medium with density $\rho$ and a magnetic field $B$. For the definition of the Alfvèn speed and a more in-depth discussion of plasma physics see e.g. Kulsrud (2005).
Both Fermi acceleration processes, first and second order, naturally result in a spectral energy distribution following a power law. This is shown below, following again Longair (2011): If the energy of a particle after one collision is $E = \beta E_0$ and there is a probability $P$ that the particle remains in the shock after the collision then there are $N_0 \cdot P^k$ particles left in the shock after $k$ collisions with energies $\beta^k E_0$. Eliminating $k$ gives

$$\frac{\ln(N/N_0)}{\ln(E/E_0)} = \frac{\ln P}{\ln \beta} \tag{2.13}$$

and therefore

$$\frac{N}{N_0} = \left(\frac{E}{E_0}\right)^{\ln P/\ln\beta} \tag{2.14}$$

and the energy distribution follows a power law:

$$N(E)\mathrm{d}E = \text{constant} \cdot E^{-1+(\ln P/\ln\beta)}. \tag{2.15}$$

The spectral index of the power law from Eq. 2.15 depends on the probability $P$ that particles remain in the shock and on the energy gain $\beta$. The argumentation by Bell (1978a) gives $P = 1 - v_s/c$ and $\beta = E/E_0 = 1 + (4v_s)/(3c)$. Inserting these values into Eq. 2.15 results in an energy spectrum with power-law form and spectral index of $-2$:

$$N(E)\mathrm{d}E \propto E^{-2}\mathrm{d}E. \tag{2.16}$$

This result was also derived in different approaches by Krymskii (1977), Axford et al. (1977) and Blandford & Ostriker (1978) by solving the transport equation for propagation of cosmic rays (see e.g. Drury (1983) and for the derivation of the equation Skilling (1975))

$$\frac{\partial d}{\partial t} + \mathbf{U} \cdot \bigtriangledown f = \bigtriangledown(\kappa \bigtriangledown f) + \frac{1}{3} \cdot \mathbf{U} p \frac{\partial f}{\partial p} + \frac{1}{p^2} \frac{\partial}{\partial} \left( p^2 D \frac{\partial f}{\partial p} \right) \tag{2.17}$$

for a special shock geometry and certain boundary conditions. $f$ is the isotropic part of the distribution function of cosmic rays and depends on the momentum $p$, location $\mathbf{x}$ and time $t$. $U$ is the velocity of the magnetic irregularities. $\kappa$ is the (anisotropic) diffusion tensor and $D$ the diffusion coefficient in momentum space. Both approaches, the microscopic one by Bell (1978a) and the macroscopic one by Krymskii (1977), Axford et al. (1977), Blandford & Ostriker (1978), do not treat backreaction and modifications of the shock due to the accelerated cosmic rays and are therefore called "test-particle" approaches.
As stated by Malkov & O'C Drury (2001), the above introduced approaches only work if "particle injection, particle confinement and shock robustness" are given. Particle injection means that at least a few particles have to cross the shock front from the down- to the upstream region. Particle confinement prevents the particles to propagate freely and the shock has to be stable in the sense that the pressure of the accelerated particles does not completly wash out the shock. These conditions were implicitly assumed in the 1970s, but are still subject to discussion (for the injection problem, see, e.g., Amano & Hoshino (2012)).
Current research takes the backreaction of the cosmic ray pressure onto the shock of the supernova remnant self-consistently in a so-called "Non-linear diffusive shock acceleration" into account. The methods used there are fully numerical simulations solving a time-dependent diffusion-convection equation, stationary Monte Carlo simulations of the particle population and approaching with semi-analytical solutions of the stationary diffusion equation coupled to gas-dynamic equations. Further references and a comparison of these different methods can be found in Caprioli et al. (2010). Magnetic field amplification in shocks are subjects of current discussion, for a recent review see, e.g., Schure et al. (2012), as well as the impact of clumpy environment onto the shock structure, see, e.g., Obergaulinger et al. (2014).

## 2.4 Gamma-ray emission processes

The previous section introduced the general idea how particles are accelerated at the shock front of a supernova remnant via diffusive shock acceleration. Observations of supernova remnants from the radio band up to TeV energies prove the existence of high-energy particles within the remnant. Different emission processes are responsible for the emission of photons in different energy bands as illustrated in Fig. 2.3.
The $\gamma$-ray emission is modeled for electrons and hadrons with the spectral form of a power law with spectral index $\Gamma = -2$ and an exponential cutoff at an energy of 100 TeV. The emission in the radio and X-ray regime is produced by leptons via synchrotron radiation and is displayed in green on Fig. 2.3. The blue curve shows the photon spectrum produced via the bremsstrahlung mechanism. This radiation depends on the density of the medium. Inverse Compton scattering from high-energy electrons off photon fields, i.e. the cosmic microwave background and starlight (red dotted and red solid curves in Fig. 2.3 ), leads to emission peaking in the TeV energy band and is produced by the same lepton population as the synchrotron emission. TeV $\gamma$-ray emission can also be produced by high-energy protons colliding with atoms of the interstellar medium or molecular clouds producing pions and in the subsquent neutral pion decay $\gamma$-rays as illustrated by the magenta line on the lower panel of Fig. 2.3. The photon emission by secondary electrons produced in the decay processes

is neglected. The hadronic and leptonic radiation processes are discussed in the following Sections 2.4.1 and 2.4.2.

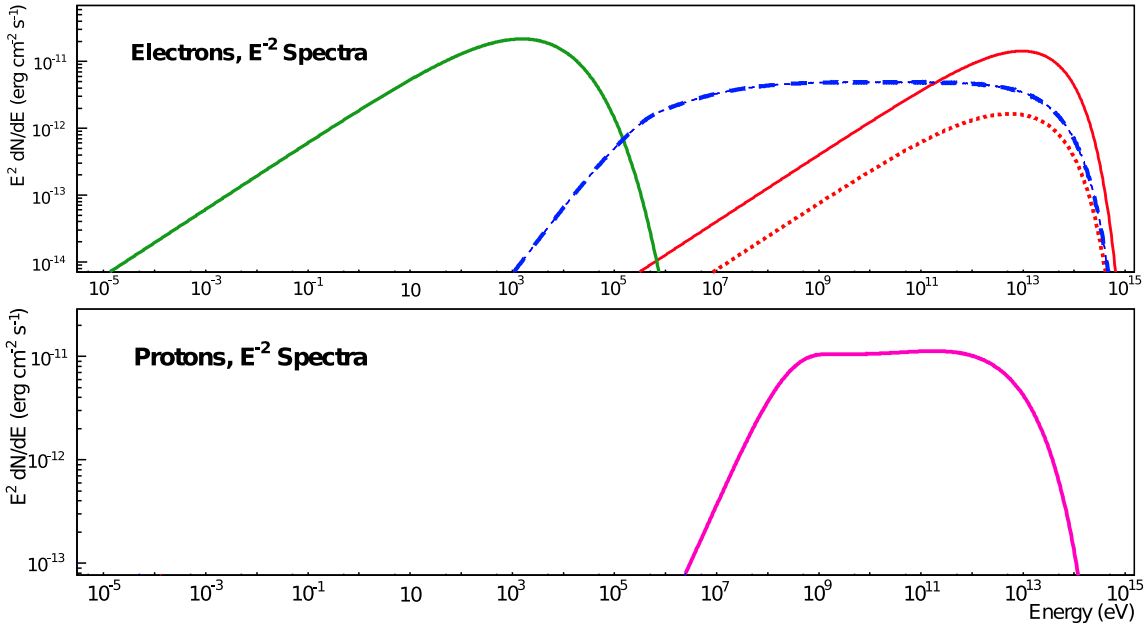


**Figure 2.3:** Photon spectra from leptonic and hadronic radiation processes as a function of energy. *Upper panel*: Photon emission by electrons. Synchrotron radiation (green), bremsstrahlung (blue) and inverse Compton scattering on the cosmic microwave background and infrared photon fields (red dotted) as well on starlight (red solid) for electrons with a spectral form of a power law with a spectral index $\Gamma = -2$ and an exponential cut off at 100 TeV.
*Lower Panel*: $\gamma$-rays from proton-proton collisions via $\pi^0$ decay (magenta). The underlying proton spectrum is a power law with spectral index $\Gamma = -2$ and an exponential cutoff at 100 TeV.
This figure is adapted from Hinton & Hofmann (2009).

## 2.4.1 Hadronic scenario

$\gamma$-ray emission can be produced by protons (p) colliding with interstellar material, mainly hydrogen, and subsequent decay of secondary particles. The main contribution originates from the decay of the neutral $\pi^0$ meson into two $\gamma$ rays:

$$p + p \rightarrow \pi^0 + X \text{ and } \pi^0 \rightarrow \gamma + \gamma. \tag{2.18}$$

The $\pi^0$ has a mass of $m_{\pi^0} \approx 135\,\mathrm{MeV/c^2}$ and the mean lifetime is about $8.4 \cdot 10^{-17}$ s.
In proton-proton collision also $\eta$ mesons are produced. Those likewise have decay channels producing $\gamma$ rays and their contribution to the total number of $\gamma$ rays is up to 25 % depending on the photon energy. This is considered in the calculations by Kelner et al. (2006).
The resulting $\gamma$-ray flux from pion-decay in an energy intervall $[E_\gamma, E_\gamma + \mathrm{d}E_\gamma]$ can be calculated following Kelner et al. (2006) as

$$\frac{\mathrm{d}N_\gamma}{\mathrm{d}E_\gamma} = c\, n_\mathrm{H} \int_{E_\gamma}^{\infty} \sigma_\mathrm{inel}(E_\mathrm{p}) J_\mathrm{p}(E_\mathrm{p}) F_\gamma \left( \frac{E_\gamma}{E_\mathrm{p}}, E_\mathrm{p} \right) \frac{\mathrm{d}E_\mathrm{p}}{E_\mathrm{p}}, \tag{2.19}$$

where $c$ is the speed of light, $n_\mathrm{H}$ the density of the medium and $J_\mathrm{p}(E_\mathrm{p})$ is the proton flux at a certain proton energy $E_\mathrm{p}$. $\sigma_\mathrm{inel}$ is the inelastic cross section of proton-proton interactions

and can be parametrised as

$$\sigma_{\mathrm{inel}}(E_{\mathrm{p}}) = (34.3 + 1.88L + 0.25L^2) \cdot \left[1 - \left(\frac{E_{\mathrm{th}}}{E_{\mathrm{p}}}\right)^4\right]^2 \mathrm{mb}. \tag{2.20}$$

$L$ is defined as $L = \ln(E_{\mathrm{p}}/1\,\mathrm{TeV})$ and the threshold energy $E_{\mathrm{th}}$ for protons to produce $\pi^0$ mesons is $1.2 \cdot 10^{-3}$ TeV. The function $F_\gamma\left(\frac{E_\gamma}{E_{\mathrm{p}}}, E_{\mathrm{p}}\right)$ from Eq. 2.19 describes the spectrum of $\gamma$-rays from the $\pi^0$- and $\eta$-meson decay channels for a certain proton energy $E_{\mathrm{p}}$:

$$F_\gamma(x, E_{\mathrm{p}}) = B_\gamma \frac{\ln(x)}{x} \left(\frac{1 - x^{\beta_\gamma}}{1 + k_\gamma x^{\beta_\gamma}(1 - x^{\beta_\gamma})}\right)^4 \left[\frac{1}{\ln(x)} - \frac{4\beta_\gamma x^{\beta_\gamma}}{1 - x^{\beta_\gamma}} - \frac{4k_\gamma \beta_\gamma x^{\beta_\gamma}(1 - s x^{\beta_\gamma})}{1 + k_\gamma x^{\beta_\gamma}(1 - x^{\beta_\gamma})}\right] \tag{2.21}$$

with $x = E_\gamma / E_{\mathrm{p}}$. The parameters $B_\gamma$, $\beta_\gamma$ and $k_\gamma$ and the function itself were derived by Kelner et al. (2006) from least square fits to the spectra obtained in simulations. These parameters depend on $L$:

$$B_\gamma = 1.30 + 0.14\,L + 0.011\,L^2, \tag{2.22}$$

$$\beta_\gamma = \frac{1}{1.70 + 0.11\,L + 0.008\,L^2} \tag{2.23}$$

and

$$k_\gamma = \frac{1}{0.801 + 0.049\,L + 0.014\,L^2}. \tag{2.24}$$

In general, the spectral form of the proton population is conserved in the $\gamma$-ray emission and the produced photons receive about one tenth of the primary proton energy. For the total photon flux as described above a factor of 1.45 is multiplied to account for the contribution by nuclei heavier than helium present in the interstellar medium and cosmic radiation (Dermer, 1986).

### 2.4.2 Leptonic scenario

$\gamma$ rays are emitted by electrons (in the following also positrons are included in the term "electrons") losing energy in magnetic fields, dense medium or scattering off photon fields. Only photons emitted by bremsstrahlung or those having gained energy via inverse Compton scattering can be observered in the TeV energy range, whereas the synchrotron radiation of electrons is typically emitted in radio to X-ray energy bands. The same electron population is responsible for the emission from synchrotron and inverse Compton emission, thus, synchrotron emission is also discussed shortly in this section apart from the bremsstrahlung and inverse Compton process.

#### Bremsstrahlung

The term bremsstrahlung is used for the radiation emitted by charged particles scattering off the electromagnetic potential of an atom and deceleration in matter. In astrophysics the bremsstrahlung from relativistic electrons plays an important role, especially in the GeV energy range. Strong et al. (2000) discussed the bremsstrahlung emission and photon spectra in great detail along with its relevance for the low-energy $\gamma$-ray astronomy.
Following the discussion in Blumenthal & Gould (1970) the energy spectrum of the emitted photons depends on the density $n_{\mathrm{Z}}$ and atomic number $Z$ of the medium. The photon

spectrum $\mathrm{d}N/\mathrm{d}E_\gamma$ for a given electron energy distribution is the integral of the bremsstrahlung spectrum for the electrons with a specific initial energy $E_\mathrm{i}$ over the whole energy range

$$\frac{\mathrm{d}N}{\mathrm{d}E_\gamma} = \int \mathrm{d}E_\mathrm{i} N_\mathrm{e}(E_\mathrm{i}) \cdot \frac{\mathrm{d}N_\mathrm{i}}{\mathrm{d}E_\gamma}. \tag{2.25}$$

The emission spectrum from a single electron can be written, under the assumption that electrons mainly scatter off the Coloumb field of hydrogen atoms, as

$$\frac{\mathrm{d}N_\mathrm{i}}{\mathrm{d}E_\gamma} = c \cdot \rho_\mathrm{i} \frac{\mathrm{d}\sigma}{\mathrm{d}E_\gamma}. \tag{2.26}$$

$\rho_\mathrm{i}$ is the hydrogen density of the medium the electron propagates through. The expression for the differential cross section $\mathrm{d}\sigma/\mathrm{d}E_\gamma$ for the bremsstrahlung process is composed of the fine stucture constant $\alpha$, the classical eletron radius $r_0$ and an energy-dependent factor $f(E_\gamma/E_\mathrm{e})$ :

$$\frac{\mathrm{d}\sigma}{\mathrm{d}E_\gamma} = \alpha \cdot r_0^2 \frac{f(E_\gamma/E_\mathrm{e})}{E_\gamma}. \tag{2.27}$$

Under the assumption that hydrogen plasma is weakly shielding Blumenthal & Gould (1970) estimated

$$f(\epsilon) = \Phi_\mathrm{weak} \cdot \left[1 + (1-\epsilon)^2 + \frac{2}{3}(1-\epsilon)\right], \tag{2.28}$$

with $\epsilon = E_\gamma/E_\mathrm{e}$ and $\Phi_\mathrm{weak}$ defined as

$$\Phi_\mathrm{weak} = 4(Z^2 + Z_\mathrm{el}) \left\{ \ln\left[\frac{2E_\mathrm{e}(E_\mathrm{i} - E_\gamma)}{E_\gamma}\right] - \frac{1}{2} \right\}. \tag{2.29}$$

$Z$ is the atomic number of the element the medium consists of and $Z_\mathrm{el}$ is the number of electrons.
In general, the spectral form of the bremsstrahlung emitted by relativistic electrons in a dense medium mainly depends on the underlying electron spectrum. TeV bremsstrahlung and X-ray synchrotron radiation of a source are related, because the emission is produced by the same electron population.

### Synchrotron radiation

Synchrotron radiation is emitted when charged particles are accelerated radially, for example electrons gyrating in a magnetic field. In the following only electrons will be discussed, since the energy loss of the particle and, therefore, the emitted radiation is suppressed for protons and ions because of much larger particle mass. This emission process dominates the non-thermal radiation in the radio to X-ray regime. A charged particle moving in a magnetic field with a strength $B$ loses the following amount of energy per time unit

$$\frac{\mathrm{d}E}{\mathrm{d}t} = -\frac{4}{3}\sigma_\mathrm{T}\gamma^2\beta^2 c U_\mathrm{B}. \tag{2.30}$$

$U_\mathrm{B}$ is the energy density of the magnetic field, $\beta = \mathrm{v}/c$ the ratio of the particle's velocity and the speed of light. $\sigma_\mathrm{T}$ is the Thomson cross section $\sigma_\mathrm{T} = 8\pi r_0^2/3 = 6.653 \cdot 10^{-29}\,\mathrm{m}^2$. Depending on the energy of the charged particle the Thomson cross section has to be replaced by the Klein-Nishina cross section (for the exact formula see, e.g., Longair (2011)).

According to Reynolds (2008) and references therein the synchrotron emission of an electron with energy $E$ rises continuously up to a maximum energy

$$h\nu_{\mathrm{m}} = 1.93(E/100\,\mathrm{TeV})^2(B/10\,\mu\mathrm{G})\,\mathrm{keV} \tag{2.31}$$

and drops exponentially beyond this energy.
The energy of the emitted photons in a frequency range $\nu$ to $\nu+\mathrm{d}\nu$ radiated by a distribution of electrons in the energy range $E$ to $E+\mathrm{d}E$ can be expressed as

$$J(\nu)\mathrm{d}\nu = \left(-\frac{\mathrm{d}E}{\mathrm{d}t}N(E)\mathrm{d}E\right). \tag{2.32}$$

Following Longair (2011) and substituting $E = \gamma m_{\mathrm{e}}c^2 = \sqrt{\nu/\nu_{\mathrm{g}}}m_{\mathrm{e}}c^2$ with $\nu_{\mathrm{g}} = e\cdot B/(2\pi m_{\mathrm{e}})$, differentiating for $\mathrm{d}E$ and replacing $\mathrm{d}E/\mathrm{d}t$ with Eq. 2.30 gives

$$J(\nu) \propto B^{(p+1)/2}\nu^{-(p-1)/2} \tag{2.33}$$

with $p$ denoting the slope of the electron energy spectrum.
The electron energy $E_{\mathrm{e}}$ required for X-ray radiation at a specific energy is, according to Reynolds (2008),

$$E_{\mathrm{e}} = 72\left(\frac{h\nu_{\text{X-ray}}}{1\,\mathrm{keV}}\right)^{\frac{1}{2}}\left(\frac{B}{10\,\mu\mathrm{G}}\right)\mathrm{TeV}. \tag{2.34}$$

The observation of non-thermal X-ray emission in supernova remnants thus demonstrates the presence of high-energy electrons accelerated up to energies of $\approx 100\,\mathrm{TeV}$.

### Inverse Compton effect

The inverse Compton effect describes the scattering of high-energy electrons off photon fields at lower energies. Electrons transfer energy to the photons and, therefore, loose energy. The energy loss of the electrons can be written similiar to Equ. 2.30

$$\frac{\mathrm{d}E}{\mathrm{d}t} = -\frac{4}{3}\sigma_{\mathrm{T}}\gamma^2\beta^2 c u_{\mathrm{rad}}, \tag{2.35}$$

with the energy density of the photon field $u_{\mathrm{rad}}$ replacing the magnetic energy density. In the Thomson regime only a small fraction of the electron energy is transfered to the photon. This is in contrast to the the Klein-Nishina-regime where the Thomson cross section is replaced with the Klein-Nishina cross section $\sigma_{\mathrm{KN}}$. For small energies $\sigma_{\mathrm{KN}} \approx \sigma_{\mathrm{T}}$, whereas in the ultra-relativistic limit ($\gamma \gg 1$)

$$\sigma_{\mathrm{KN}} = \pi r_0^2\frac{1}{x}\left(\ln(2x)+\frac{1}{2}\right) \tag{2.36}$$

with $x = h\nu/m_{\mathrm{e}}c^2$ and the classical electron radius $r_0$.
Blumenthal & Gould (1970) calculated the spectral emissivity $I(\nu)$ under the assumption of an isotropic photon field in the ultra-relativistic regime as

$$I(\nu)\mathrm{d}\nu = \frac{3\sigma_{\mathrm{T}}c}{16\gamma^4}\nu\left[2\nu\cdot\ln\left(\frac{\nu}{4\gamma^2\nu_0}+\nu+4\gamma^2\nu_0-\frac{\nu^2}{2\gamma^2\nu_0}\right)\right]\mathrm{d}\nu. \tag{2.37}$$

The maximal energy a photon can gain by head-on collision with an electron is given by

$$h\nu_{max} \approx 4\gamma^2 h\nu. \tag{2.38}$$

Relevant photon fields in astrophysics are the cosmic microwave background (CMB), infrared light emitted by dust and optical starlight. Inverse Compton scattering of electrons off these photon fields are the standard scenario to explain, for example, the observed TeV $\gamma$-ray radiation from pulsar wind nebulae (see e.g. Gaensler & Slane (2006) and references therein).

CHAPTER 3

# Gamma-ray emitting molecular clouds

Today's imaging atmospheric Cherenkov telescope systems such as H.E.S.S., MAGIC and VERITAS detected $\gamma$-ray emission in the TeV energy range from more than ten supernova remnants. For most of the supernova remnants it is not clear whether the observed $\gamma$-ray emission is mainly produced by accelerated leptons or hadrons. Molecular clouds near supernova remnants provide a suitable environment to probe hadronic acceleration in supernova remnants, as $\gamma$-ray emission coincident with molecular clouds proves the hadronic origin of the emission. Leptonic emisson processes, except possibly bremsstrahlung in the Galactic centre region, are negligible regarding the $\gamma$-ray emission of clouds in the TeV energy band. Apart from the possibility to probe hadronic acceleration in supernova remnants, $\gamma$-ray emitting molecular clouds close to remnants are also good laboratories to study propagation properties of high-energy particles through the interstellar medium from the remnant to the cloud.
The general properties of molecular clouds are outlined in Section 3.1. Three scenarios leading to $\gamma$-ray emission from molecular clouds are discussed in this chapter. Section 3.2 describes the scenario of "passive molecular clouds", clouds only embedded in the cosmic ray sea without a individual source nearby. Molecular clouds near cosmic ray sources such as molecular clouds interacting with the shock of a supernova remnant are introduced in Section 3.3 and molecular clouds illuminated by escaped particles from the supernova remnant in Section 3.4.

## 3.1 General properties of molecular clouds

Dense accumulations of molecular gas within the interstellar medium are usually referred to as "molecular clouds". Molecular clouds can be observed directly using molecular line emission at radio wavelengths. The main constituent is molecular hydrogen ($H_2$). Since $H_2$ does not posses a permanent dipole moment, thus, no transitions are excited at low temperatures as usually found in the environment of molecular clouds. For $H_2$ line emission to be produced, temperatures of about 150 K are required - much higher than commonly found in molecular clouds. Hence, other molecules are used as tracers for $H_2$ such as the

carbon monoxide molecule (CO). The most commonly used emission line, according to Fukui & Kawamura (2010), is the rotational transition $^{12}C^{16}O(J = 1-0)$ with a frequence of 115.27120 GHz[1].
$^{12}C^{16}O(J = 1-0)$ has an excitation energy of $\approx 5$ K and a critical density of $\approx 1000\,\mathrm{cm}^{-3}$. Simplified, the critical density is the density at which the line emission gets observable. Line emissions of other transitions or molecules have different excitation energies and critical densities, thus the density distribution of the interstellar medium can be probed using different molecules or different transitions as tracers.
The $H_2$ column density and the cloud mass can be estimated from the intensity of the CO line emission $W(^{12}C^{16}O(J = 1-0))$ via the conversion factor $X_{CO}$:

$$N_{H_2} = X_{CO} \cdot W(^{12}C^{16}O(J = 1-0)). \tag{3.1}$$

With the exception of the Galactic centre, in the galactic plane $X_{CO}$ has a typical value of $\approx 2 \cdot 10^{20}(\mathrm{K\ km\ s^{-1}})^{-1}$ and can be determined via measurements of the virial mass of the cloud, dust emission, extinction and from GeV $\gamma$-ray emission along the Galactic plane. The conversion factor and methods to estimate it are discussed in detail in the recent review of Bolatto et al. (2013).
The first observation of CO emission was reported by Wilson et al. (1970) observed in the galactic interstellar medium from the Orion nebula. Subsequent radio surveys in the 1970s and '80s established molecular clouds as major constituents of the Galactic interstellar medium (see e.g. the review of Fukui & Kawamura (2010) and references therein). CO emission was also detected in other galaxies (Combes et al., 1977). The first complete CO survey of the Galactic plane was published by Dame et al. (1987). Since then Galactic CO emission has been observed not only from molecular clouds and giant molecular clouds (GMCs; molecular clouds with masses of about $\geq 10^5\,M_\odot$ and sizes around 50 pc) but also as cold CO "bridges" between the spiral arms and extending beyond the galactic disk. Giant molecular clouds are located mostly in the spiral arms and are known since the early 1980s to harbour star forming regions (Blitz & Thaddeus, 1980). Molecular clouds have no homogenous density distribution as it is clearly visible in Fig. 3.1 for the molecular cloud complex in the W44 region, but a rather clotted structure with dense cores, often called clumps. This figure shows $^{13}$CO emission from the Galactic Ring Survey (Jackson et al., 2006) integrated over velocities between 30 km s$^{-1}$ and 65 km s$^{-1}$. This molecular cloud complex is located at a distance of about 2.5 kpc to Earth and an angular distance of 0.2° at this distance corresponds to a length of $\approx 9$ pc. Current instruments resolve complex structures of nearby clouds down to the milliparsec scale, e.g., (Falgarone et al., 2009).
The magnetic field within molecular clouds can be estimated, e.g., by observing the polarized emission of dust or using the Zeeman effect in HI, OH and CN line emission. The maximum interstellar magnetic field strength is $\approx 10\,\mu$G up to densities of $300\,\mathrm{cm}^{-3}$ and increases at higher densities following a power law with index $\approx 2/3$. These numbers and a very detailed discussion on the different methods for the magnetic field estimation can be found in the recent review by Crutcher (2012).
The distances of molecular clouds can be determined via the so-called kinematic distance method. The disk of the Milky Way is rotating and therefore the Doppler shift of the observed molecular line gives the relative line-of-sight velocity $V_R$ of the cloud. This is the projection of the orbital velocity $V_{MC}$ of the molecular cloud onto the line of sight as shown for the three molecular clouds on Fig. 3.2. The galactocentric radius $R$, i.e., the distance of the cloud to

[1] http://www.cv.nrao.edu/php/splat/

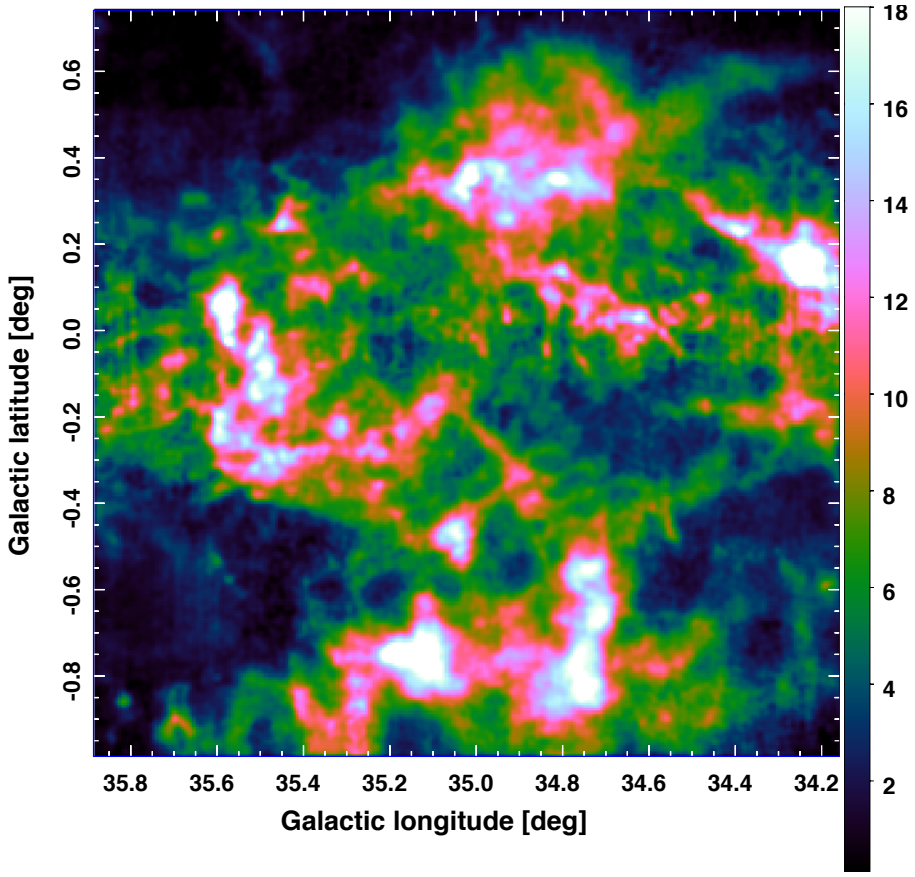


**Figure 3.1:** $^{13}$CO line emission, integrated over the velocities between 30 km s$^{-1}$ and 65 km s$^{-1}$, in units of [K km s$^{-1}$] of the molecular cloud complex in the W44 region. Data from the Galactic Ring Survey (Jackson et al., 2006) were used for this image.

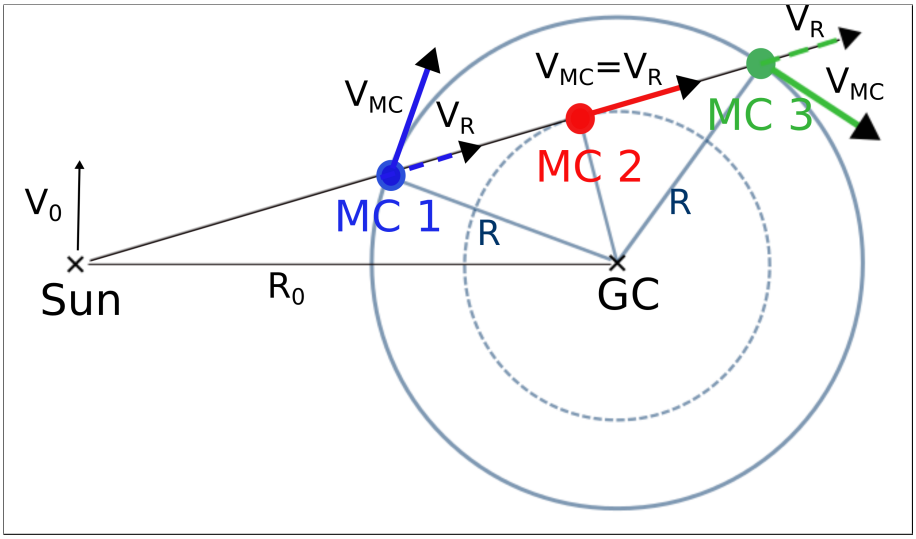


**Figure 3.2:** Three molecular clouds have different distances but the same line-of-sight velocity $V_R$. The cloud 2 is located at the tangent point where the orbital velocity $V_{MC}$ is equal to the line-of-sight velocity $V_R$. The illustration is adapted from Roman-Duval et al. (2009).

the Galactic centre (GC), can be determined with rotation curves of the galaxy, e.g. Brand & Blitz (1993). The distance $d$ of the molecular cloud to the sun can be calculated, e.g., (Roman-Duval et al., 2009), as

$$d = R_0 \cdot \cos(l) \pm \sqrt{R^2 - R_0^2 \cdot \sin^2(l)} \tag{3.2}$$

with the longitude position $l$ of the cloud and the galactocentric radius $R_0$ of the sun. The the clouds 1 and 3 on Fig. 3.2 have different distances but the same line-of-sight velocity. This is called "near-far ambiguity" and can only be resolved with additional information, e.g., by looking for absorption features in HI emission as done by Roman-Duval et al. (2009), except a cloud is located on the tangent point like cloud 2 in Fig. 3.2. In that specific case, the near and far distances are identical.

## 3.2 Passive molecular clouds

Cosmic rays at GeV energies remain in the Galaxy for about $\sim 10^7$yr (Ptuskin, 2012). The particles got accelerated by individual sources, but lose the information of their origin and contribute to the so-called "cosmic ray sea" (see, e.g., Casanova et al., 2010). Molecular clouds are embedded in this cosmic ray sea and provide "passive" targets for cosmic ray hadrons to interact and produce $\gamma$-ray emission via neutral pion decay. The integral $\gamma$-ray flux $F_\gamma$ above an energy threshold $E$ depends on the cosmic ray flux, on the molecular cloud mass $M_{\mathrm{MC}}$ and on the distance $D$ (Aharonian, 1991):

$$F_\gamma(\geqslant E) = 1.5 \cdot 10^{-13} \left(\frac{E}{1\,\mathrm{TeV}}\right)^{-1.75} \left(\frac{M_5}{D_{\mathrm{kpc}}^2}\right) \mathrm{cm}^{-2}\,\mathrm{s}^{-1}. \tag{3.3}$$

$M_5$ is the mass of the molecular cloud in units of $10^5 \mathrm{M}_\odot$, $D_{\mathrm{kpc}}$ the distance of the cloud in units of kpc and this approximation is only valid for energies much larger than 1 GeV.
$\gamma$-ray emission from local molecular clouds is observed in the GeV energy range and can be used to probe the level of the cosmic ray sea at different locations of the Galaxy (Issa & Wolfendale, 1981). Passive molecular clouds have not been detected so far in the TeV energy range because of the low expected fluxes and their extension, but the future experiment CTA observatory should be capable of observing nearby clouds (Pedaletti et al., 2013) and also of investigating the morphology of $\gamma$-ray emission and compare it to the structures of $H_2$ emission in the Galaxy (Casanova et al., 2010).

## 3.3 Molecular clouds interacting with shocks of supernova remnants

Associations of supernova remnants with star-forming regions are established $\gamma$-ray sources in GeV astronomy since the 1970s (Montmerle, 1979). These regions are embedded in molecular clouds and therefore the ambient medium provides dense target material for hadrons accelerated in the supernova remnant and $\gamma$-ray emission due to pion decay is observed. In those regions either the supernova explodes within the dense medium, where particle acceleration cannot take place efficiently due to the low shock speed, or the remnant expands into a nearby cloud (Aharonian et al., 1994). Supernova remnants that interact with molecular clouds are bright sources detected with the *Fermi-LAT* satellite in the GeV energy range (see Thompson et al. (2012) and references therein) and are also strong in the TeV energy band (e.g., Aharonian et al., 2008a,b). The $\gamma$-ray emission produced by supernova remnant shocks that overtake molecular clouds is spatially coincident with the shell of the supernova remnant or at least some parts of it (Aharonian et al., 1994). The observed $\gamma$-ray spectrum reflects the spectrum of accelerated hadrons in the shock of a supernova remnant.

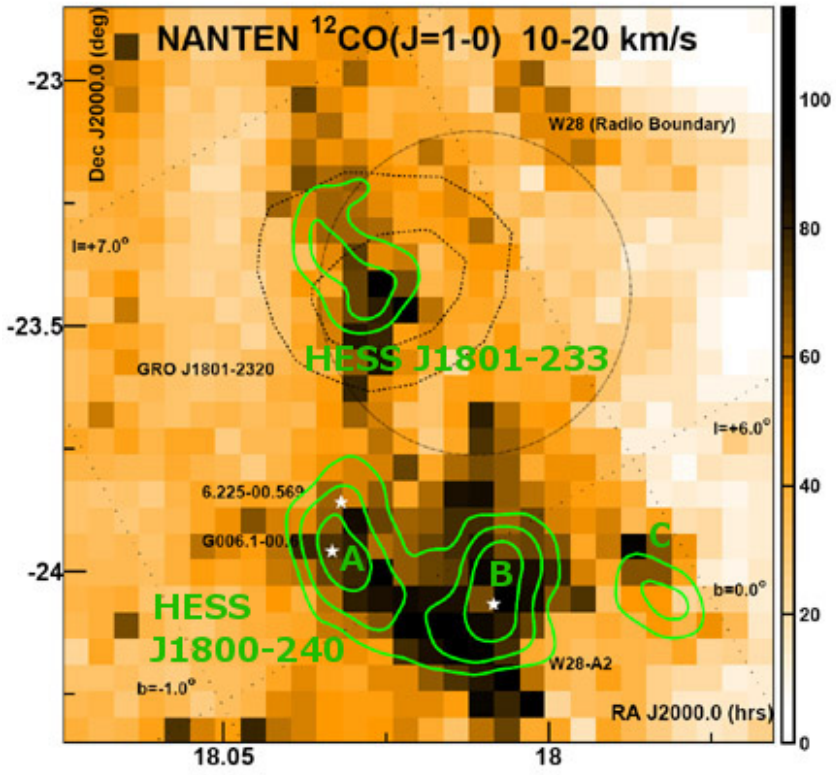


**Figure 3.3:** The region around the supernova remnant W28. The $^{12}$CO emission is overlaid with the 4, 5 and 6 $\sigma$ contours of the TeV $\gamma$-ray emission observed by H.E.S.S in green. The figure is taken from H.E.S.S. collaboration (2007).

The interaction of the shock of a supernova remnant with a molecular cloud is usually established with observation of OH 1720 MHz maser emission within the extent of the remnant (see, e.g., Frail et al., 1996). This type of emission is defined by compact narrow emission lines and high effective temperatures and is produced by OH molecules colliding with $H_2$ molecules. This process takes place in the compressed and heated material behind

the shock. Maser emission is also observed in star-forming regions, albeit at different wavelengths. Following Jiang et al. (2010) other evidence for supernova remnant/molecular cloud interactions includes: line broadening in molecular emission or asymmetric profile, line emission with large high-to-low excitation line ratio, near infrared emission due to shock excitation and morphological agreement of the molecular emission with supernova remnant features. A detailed list of known galactic supernova remnants/molecular cloud associations can be found in the appendix of Jiang et al. (2010). In about half of the listed regions $\gamma$-ray emission is observed.
A prominent example for a supernova remnant/molecular cloud association observed in the TeV (Aharonian et al., 2008b) and GeV bands (Abdo et al., 2010) is the supernova remnant W28. The CO emission from this region is shown in Fig. 3.3. The TeV $\gamma$-ray emission observed with H.E.S.S. is indicated by the green contour lines. The H.E.S.S. source HESS J1801–233 is coincident with a molecular cloud clearly visible in CO emission. The black circle indicates the radio size and position of W28. The $\gamma$-ray emission is spatially coincident with parts of the shell of the supernova remnant and the molecular cloud. But not only the source HESS J1801–233 is associated to the supernova remnant, but also the three sources HESS J1800–240 A,B and C (Aharonian et al., 2008b). They are also coincident with dense molecular material and the $\gamma$-ray emission observed there is interpreted as pion decay from accelerated particles escaped from the remnant and propagated through the interstellar medium illuminating the molecular clouds.

## 3.4 Illuminated molecular clouds

As the example of the W28 region illustrates, accelerated particles do not remain confined within the supernova remnant forever, they escape from it and propagate through the interstellar medium. Dense environment near the supernova remnants provides target material for proton collisions and the subsequent pion decay produces $\gamma$-ray emission observable with current imaging Cherenkov telescope systems, e.g. by the H.E.S.S. experiment (Aharonian et al., 2008b; Gabici et al., 2009).
This work studies the potential $\gamma$-ray emission of molecular clouds near supernova remnants as discussed in Chapter 6 with the help of the model by Gabici et al. (2009). This model predicts the $\gamma$-ray emission for particles escaping the acceleration region and interacting with nearby clouds. It is described in the following paragraphs.
The proposed model by Gabici et al. (2009) considers a supernova having exploded in a medium of density $n$ with a total energy release of $E_{\mathrm{SN}} \approx 10^{51}$erg. The remnant is assumed to be already in the Sedov phase in which the shock radius $R$ and velocity $u$ scale with time as $R \propto t^{2/5}$ and $u \propto t^{-3/5}$ (see Chapter 2.2). At first the highest energetic particles are leaving, but the maximum momentum of particles remain in the shock $p_{\mathrm{max}}$ is decreasing with time as $p_{\mathrm{max}} \propto t^{-\delta}$, and later on only particles with lower and lower energy remain confined in the supernova remnant. Gabici et al. (2009) assume an index $\delta$ of 2.48. This corresponds to a maximum momentum of 5 PeV at a time of 200 yr and 1 GeV at a time of $5 \cdot 10^4$ y$r$.
The escaped particles propagate from the remnant into the interstellar medium. This propagation can be described by a diffusion with energy-dependent diffusion length $D(E)$. Up to now, the exact process of high-energetic particles propagating through the interstellar medium is still a case of discussion see e.g. (see, e.g., Ptuskin, 2012; Giacinti et al., 2012; Aloisio & Blasi, 2013), but for the purpose of this work, the simplified assumption of an

isotropic energy dependent diffusion coefficient is sufficient. More complex models need more detailed information on the individual regions than obtainable from the molecular cloud and supernova remnant catalogues. The diffusion coefficient is calculated as

$$D(E) = D_{10}\left(\frac{E}{10\,\mathrm{GeV}}\right)^{s}\mathrm{cm}^2\ \mathrm{s}^{-1} \tag{3.4}$$

with $s \in [0.3; 0.7]$. $D_{10}$ is the normalisation at 10 GeV of the diffusion coefficient. The Galactic average is $D_{10} \approx 10^{28}$ (Strong et al., 2007), but the local value in dense regions near supernova remnants might be lower by up to two orders of magnitudes due to a stronger and more turbulent magnetic field (Gabici et al. (2010); Li & Chen (2010); Ohira et al. (2011); Yan et al. (2012)).

The spectrum of escaped particles from the remnant is calculated solving the diffusion equation:

$$\frac{\partial f_{\mathrm{out}}}{\partial t}(R,p,t) = D(p)\nabla^2 f_{\mathrm{out}}(R,p,t) + q_{\mathrm{esc}}(p,t)\delta(R). \tag{3.5}$$

$q_{esc}$(p,t) is the spectrum of run-away particles at a certain time $t$ with momentum $p$. Under the assumption that the time evolution of the maximum momentum of particles in the shock $p_{\mathrm{max}}$ follows a power-law function of time, Eq. 3.5 can be solved analytically by the distribution function $f_{\mathrm{out}}$ dependent on the time $t$, the distance of the cloud to the centre $R$ of the supernova remnant and energy $E$:

$$f_{out}(t,R,E) = \frac{\eta E_{\mathrm{SN}}}{\pi^{3/2}\ln(E_{\mathrm{max}}/E_{\mathrm{min}})}\frac{e^{-\left(\frac{R}{R_d}\right)^2}}{R_d^3}E^{-2}. \tag{3.6}$$

$\eta E_{\mathrm{SN}}$ is the amount of the explosion energy converted into the acceleration of particles, $E_{\mathrm{min}}$ and $E_{\mathrm{max}}$ are the minimum and maximum energies of particles accelerated during the Sedov phase of the remnant. $R_{\mathrm{d}} = \sqrt{4D(E)(t-\chi(E))}$ is the diffusion length of a particle with energy $E$. The time $\chi$ after the supernova explosion at which particles with energy E are escaping from the remnant is calculated as $\chi = t_{\mathrm{Sedov}}(E/E_{\mathrm{max}})^{-1/\delta}$ with $t_{\mathrm{Sedov}}$ being the time when the supernova remnant entered the Sedov phase.

The spectrum of protons at any given distance to the remnant and any specific moment in time can be calculated using the distribution function from equation 3.6, adding the flux of the cosmic ray sea as it is observed at Earth, $J_{\mathrm{CR}} = 2.2(E/\mathrm{GeV})^{-2.75}\mathrm{cm}^{-2}\,\mathrm{s}^{-1}\,\mathrm{GeV}^{-1}\,\mathrm{sr}^{-1}$ (Dermer, 1986), and using the parameterisation by Kelner et al. (2006) for the calculation of the $\gamma$-ray emission due to pion decay.

Figure 3.4 shows the expected $\gamma$-ray energy spectrum for a molecular cloud with a mass of $10^5\,\mathrm{M}_\odot$ and distance to Earth of 1 kpc, located 100 pc to a supernova remnant. The spectra are calculated for a diffusion coefficient $D_{10}$ of $10^{28}$ and $\eta E_{\mathrm{SN}} = 0.3 \cdot 10^{51}$erg. The black dotted line shows the spectrum 500 yr after the explosion, the red dash-dotted line refers to 2000 yr, the blue long-dashed one to 8000 yr and the green short-dashed one to 32000 yr. The $\gamma$-ray spectrum arising solely from the cosmic-ray sea is shown with a solid black line for comparison. The spectrum of $\gamma$-rays emitted by the cloud is clearly time-dependent. The contribution of the escaped particles at the cloud location has a peak in the $E^2\,\mathrm{d}N/\mathrm{d}E$ distribution for small times at energies between $(10^{14} - 10^{15})$ eV, because at that time only the most energetic particles already escaped from the remnant and arrived at the cloud location. With time the maximum moves to lower energies because particles with lower and lower energies escape from the remnant and reach the cloud.

Fig. 3.4 only shows the $\gamma$-ray emission from pion-decay, not considering secondary electrons produced in charged pion decays and their emission processes. Pion decay dominates the

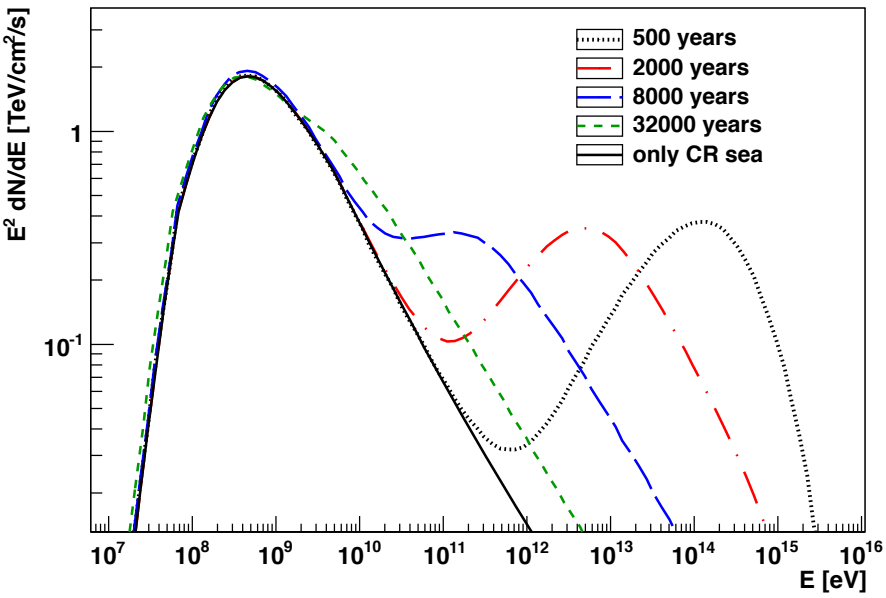


**Figure 3.4:** $\gamma$-ray flux in dependence of energy for a molecular cloud with a mass of $10^5\,M_\odot$ and distance to Earth of 1 kpc located 100 pc to a supernova remnant for various ages of a supernova remnant. The black solid line represents the expeceted spectrum only from the cosmic-ray (CR) sea.

$\gamma$-ray emission from illuminated molecular clouds as shown, e.g., in Gabici et al. (2009) and the emission from the secondary produced eletrons is neglectable in the TeV energy range. Cosmic rays above 1 GeV can freely penetrate a molecular cloud when the diffusion coefficient is not significantly lower than the Galactic average (Gabici et al., 2007, 2009). For times $>$ 2000 yr less energetic cosmic rays reach the cloud and synchrotron emission from the produced electrons is breaking off at lower energies. This naturally explains a high TeV-to-keV flux ratio and illuminated molecular clouds might be an explanation for TeV sources without significant counterparts in other wavelengths, often called “dark” TeV sources.

Several supernova remnant have been discovered in the TeV energy band (for a recent review see Aharonian (2013)), but until now no source with particle energies up to $10^{15}$ eV, so called “Pevatrons” have been observed despite the commonly paradigm of supernova remnants as sources of the cosmic rays up to energies of $10^{15}$ eV. One reason might be that particles are accelerated only in early stages of the evolution of a supernova remnant to those high energies with the maximum energy quickly decreasing with time. Hence, one has to be rather lucky to observe a supernova remnant while emitting cosmic rays beyond 100 TeV (Aharonian, 2013). In the context of the search for Pevatron sources it might be interesting to look at supernova remnants with dense environment because there the escaped particles remain observable for a longer period of time than in the remnant itself.

$\gamma$-ray emitting molecular clouds near supernova remnants also provide the unique environment to study propagation properties of high-energy particles as extensively shown for the W28 region as discussed in Chapter 1. This work presents in Section 6.3 a constraint on the average normalisation of the diffusion coefficient $D_{10}$ in dense regions near supernova remnants with the help of this scenario.

CHAPTER 4

# The H.E.S.S. experiment

Since the discovery of the Crab nebula with imaging atmospheric Cherenkov telescopes in 1989 by the Whipple telescope[1] (Weekes et al., 1989), this technique has been leading to numerous discoveries of cosmic $\gamma$-ray sources in the TeV energy regime and is introduced in Section 4.1. The number of TeV sources in dependence of the time is shown in Fig. 4.1 for the current experiments H.E.S.S., MAGIC and VERITAS individually. Since the beginning of operation the H.E.S.S. experiment has been participating significantly to enlarge the number of $\gamma$-ray sources, both Galactic and extra-galactic ones. The next large increase for the number of detected TeV sources is expected to arise with the future observatory CTA[2]. Until now more than 140 individual $\gamma$-ray sources have been detected and this huge number makes population studies possible. The H.E.S.S. experiment provides with the H.E.S.S. Galactic Plane Survey a very suitable data set for population studies as shown for pulsar wind nebula (H.E.S.S. Collaboration et al., 2014a) and supernova remnants (H.E.S.S. Collaboration et al., 2014b). The H.E.S.S. experiment is introduced in section 4.2. Both the experimental setup as well as the reconstruction and analysis steps are explained. The data set of the H.E.S.S. Galactic Plane Survey and its sources are discribed in Section 4.3.

## 4.1 Ground-based detection of gamma rays

High-energy $\gamma$ rays cannot be observed directly with ground-based instruments due to the opacity of the Earth's atmosphere for photons in this energy range. Instruments optimised to detect $\gamma$ rays at GeV energies avoid this problem using direct photon detection on satellite-borne experiments, but the much lower photon fluxes in the TeV energy range require larger collection areas than realisable in space. Therefore, ground-based $\gamma$-ray astronomy observes the secondary particles produced in the interaction of the TeV photons with the atmosphere and thus uses the atmosphere as a "calorimeter". The secondary particles in the airshower emit Cherenkov light which can be detected by optical instruments on Earth. The properties

[1] named after the American astronomer Fred Lawrence Whipple
[2] **C**herenkov **T**elescope **A**rray

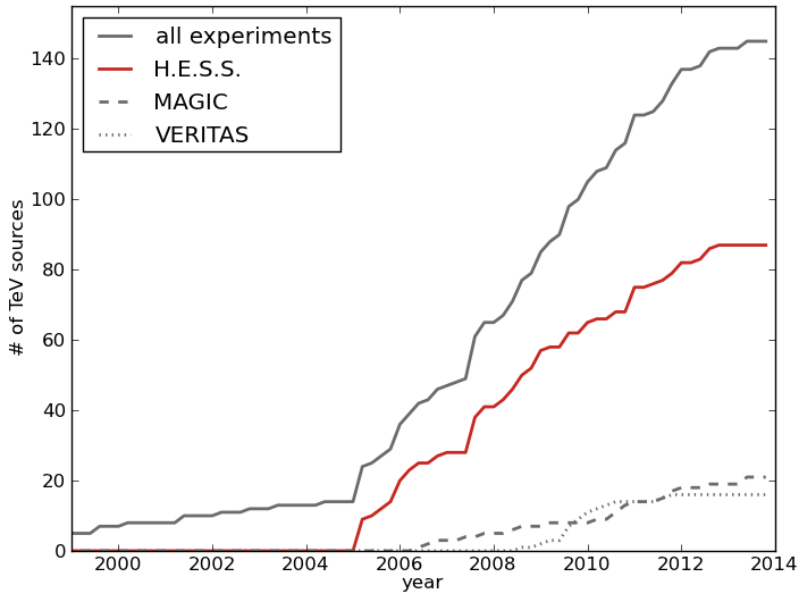


**Figure 4.1:** The number of detected TeV $\gamma$-ray sources in dependence of the year. The number of detections for the experiments H.E.S.S. (red line), MAGIC (black dashed line) and VERITAS (black dotted line) are listed seperately. These numbers are taken from the TeV source catalogue TeVCat. Image credit: the H.E.S.S. Collaboration.

of the primary $\gamma$ rays are reconstructed from images of the Cherenkov light emitted from the charged secondary particles in the air shower.

### 4.1.1 Air showers

Air showers consist of a cascade of secondary particles produced when a highly energetic particle hits the atmosphere. If the primary particle is a photon, it will at some point interact with the Coulomb field of an atmospheric atom and produce an electron-positron pair. The newly generated electron and positron will subsequently generate photons via bremsstrahlung, those again generate new electron-positron pairs. With each interaction the energy of the produced particles decreases and the cross sections for the different processes change with energy. The cascade stops when the production of bremsstrahlung is suppressed once the ionisation and excitation of the atmospheric atoms become the dominant processes. In a very similar way, high-energy electrons can also initiate electromagnetic air showers. Here, the first interaction process is the emission of a photon via bremsstrahlung instead of the pair production.
In the following a simple model introduced by Heitler (1954) is described (see Fig. 4.2). This model considers only bremsstrahlung and pair production for particle creation in electromagnetic air showers. For both processes the same interaction length is used. It is further assumed, that the energy of all secondary particles is equipartitioned. The induced air shower consists of $N(x) = 2^{(x/X_0)}$ particles after a distance $x$ and $n = x/X_0$ branchings. $X_0$, the radiation length, is defined as the mean distance over which a high-energy electron loses all but $1/e$ of its energy via bremsstrahlung. It is also $7/9$ of the mean free path for pair production by a high energy photon (Beringer et al., 2012). In this simple picture it is assumed both interaction lengths for relativistic electrons and photons are equal. $X_0$ has a

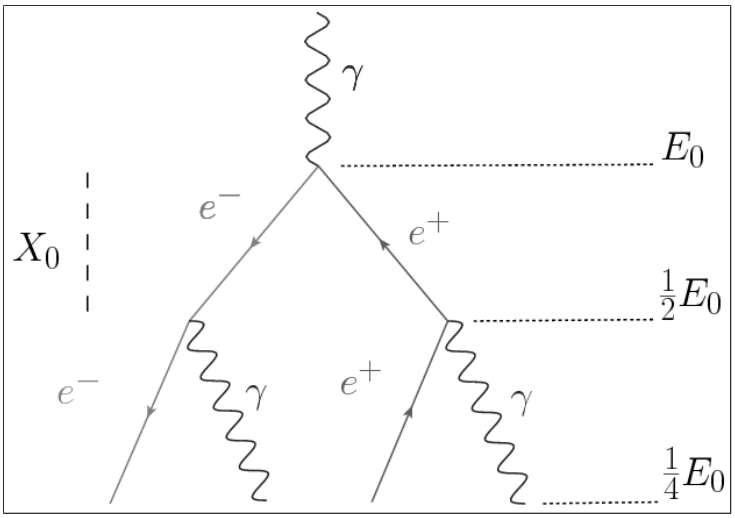


**Figure 4.2:** Heitler model for the evolution of an electromagnetic air shower.

value of $3.72\,\mathrm{g\,cm^{-2}}$ in air (Beringer et al., 2012). Each of the produced $N(x)$ particles for a primary particle with an energy of $E_0$ has an average energy of $E(x) = E_0 \cdot 2^{(-x/X_0)} = E_0/N(x)$. The shower reaches it maximal lateral extent in the atmosphere at a depth of

$$X_{\mathrm{max}} = \frac{\ln(E_0/E_\mathrm{c})}{\ln 2} \cdot X_0, \tag{4.1}$$

with the critical energy $E_\mathrm{c}$ where the shower cascade ends as average collisional energy losses begin to exceed radiative losses. The value of $E_\mathrm{c}$ in air is $\approx 80\,\mathrm{MeV}$. The number of particles at the shower maximum extent can be calculated as

$$N_{\mathrm{max}} = 2^{X_{\mathrm{max}}/X_0} = \frac{E_0}{E_\mathrm{c}}. \tag{4.2}$$

This simple model described above predicts a rising number of secondary particles in the shower with increasing energy and also a larger depth of the shower maximum. Realistic shower simulations that also consider energy-loss processes during shower formation and other higher order interaction processes confirm these general properties. An air shower induced by a 1 TeV $\gamma$ ray typically reaches its shower maximum at $\approx 10\,\mathrm{km}$ above sea level.

### Comparison of photon and hadron induced air showers

So far the discussion covered only air showers induced by high-energy photons and electrons. However, the cosmic ray flux measured here at Earth mainly consists of hadrons, especially protons or light atomic nuclei. These particles also induce air showers when interacting with the Earth's atmosphere, so-called "hadronic air showers". Due to different processes which include hadronic interactions those showers exhibit a different evolution compared to purely electromagnetic showers. The main differences are discussed in the following. A more detailed discussion can be found, e.g., in Longair (1992) or Aharonian et al. (2008). The incoming hadron scatters inelastically with the nuclei of an atmospheric molecule and secondary particles like pions, kaons are produced via the strong interaction. Contrary to an electromagnetic air shower the hadronic one consists both of hadronic and electromagnetic sub showers. The electromagnetic sub showers are produced by the decay of charged and neutral mesons.

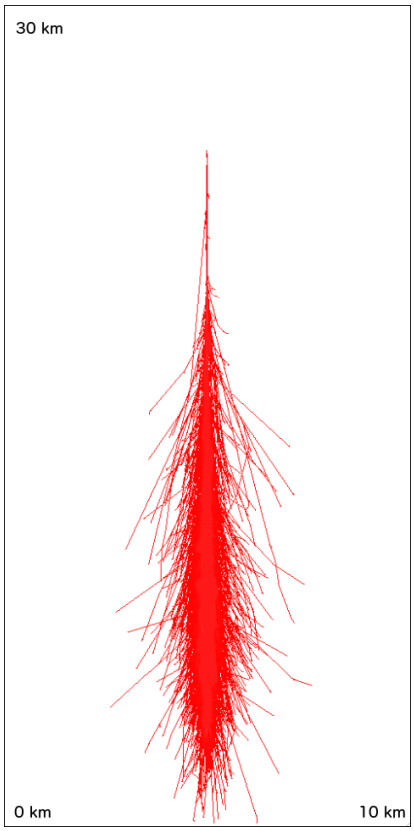


(a) $\gamma$-ray-induced air shower with a primary energy of 300 GeV and first-interaction height of 23 km.

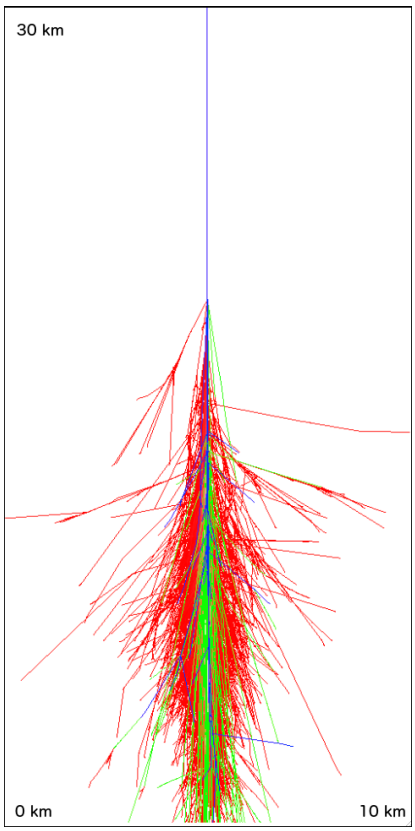


(b) hadron-induced air shower with a primary energy of 1 TeV and first-interaction heigth of 18 km.

**Figure 4.3:** Simulations of a photon and hadron-induced air shower (with courtesy of K. Valerius). A $\gamma$-ray-initiated air shower consists only of an electromagnetic component (illustrated in red), whereas the hadron-induced shower has apart from the blue coloured hadronic component, a distinct muon component coloured in green and electromagnetic sub showers illustrated in red.

The different shower components in an electromagnetic and hadronic shower are illustrated in Figure 4.3. The electromagnetic shower induced by a photon consists only of the electromagnetic component whereas the air shower initiated by a hadron exhibits, apart from the hadronic sub shower also an electromagnetic component and a distinct muon component. The different evolution of hadronic and electromagnetic showers allows a clear distinction. Protons with TeV energies have a longer mean free path than the radiation length for a photon in air. Therefore, the depth of the maximum shower extent is deeper for hadronic showers than for electromagnetic ones at comparable energies. The lateral extension of a hadronic shower is larger than for an electromagnetic one, because the lateral development is mainly constrained by the mean scattering angle of the interactions and the one for Coulomb scattering in electromagnetic showers is smaller than the average scattering angle for hadronic processes. Hadronic showers are less regular and have more fluctuations than electromagnetic ones due to more complex multi-particle processes involved in the shower evolution.

### 4.1.2 Imaging atmospheric Cherenkov telescopes

Ground-based $\gamma$-ray instruments observe the Cherenkov light of the charged relativistic secondary particles of a photon-induced air shower as illustrated in Fig. 4.4(a). Charged particles emit light, if their speed v is larger than the speed of light within a medium of refractive index $n$. The ambient medium around the charged particle is polarised. During the depolarisation coherent light is emitted and the wave fronts superimpose. A light cone with an opening angle of $\cos\theta = 1/(\beta \cdot n)$ with $\beta = \mathrm{v}/c$ is formed. The refractive index changes with the atmospheric density. The opening angle of the Cherenkov cone of an air shower induced by a 1 TeV photon is typically $\approx 1^\circ$. This is illustrated in Fig. 4.4(a).
Cherenkov light has a continuous spectrum up to a "cutoff wavelength" that extends over the optical and ultraviolet (UV) region. The relative intensity $I$ depends on the wavelength $\lambda$ with $I \propto 1/\lambda^2$. The refractive index $n(\lambda)$ depends on the wavelength of the light and at the cutoff wavelength the condition $\mathrm{v} > c/n(\lambda)$ is no longer fulfilled.
The shower maximum of $\gamma$-ray-induced air showers typically occurs 10 km above sea level. Ozone molecules within the atmosphere absorb most Cherenkov photons in the UV range before they reach the ground. Rayleigh or Mie scattering off aerosol molecules in the atmosphere also reduces the intensity at optical wavelengths. Typically 100 photons per $\mathrm{m}^2$ can be observed at an altitude of 2000 $\mathrm{m}^2$ above sea level and, therefore, large collection areas are needed. IACTs observe the Cherenkov light in the blue optical band with mirrors and sensors optimised for these wavelengths. With an opening angle of $\approx 1^\circ$ one air shower illuminates an area with a diameter of about 260 m on ground. Every telescope within this area can observe the shower, as illustrated in Fig. 4.4(a), and that way large effective detector areas can be achieved. Figure 4.4(b) illustrates the basic observation principle. The Cherenkov light emitted by an air shower is collected by a reflector and projected onto a camera, which is positioned in the focal plane and takes an image of the shower. These shower images taken by the camera are the basis of the reconstruction of the primary particle's properties.

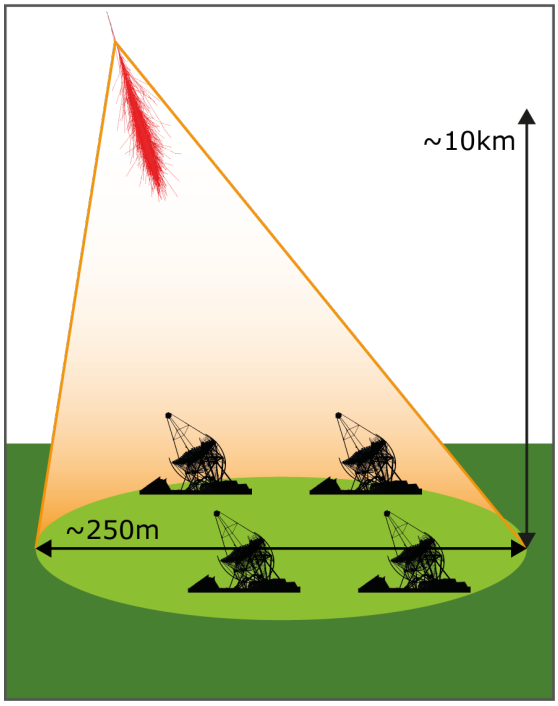


(a) A $\gamma$-ray interacts with the atmosphere and the initiated air shower emits Cherenkov light. All telescopes within the illuminated area can observe the shower.

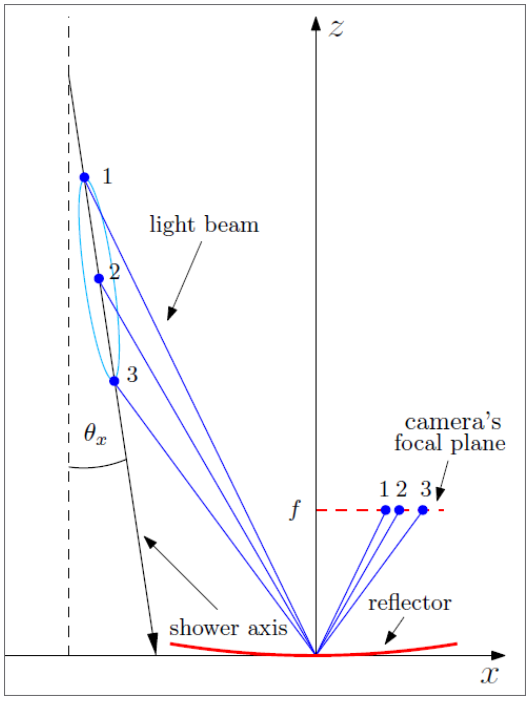


(b) Basic observation principle of an imaging atmospheriv Cherenkov telescope. The Cherenkov photons emitted by the air shower are collected with large reflectors and reflected onto the focal plane where a camera is positioned.

**Figure 4.4:** Observation of Cherenkov photons with telescopes, emitted by an air shower.

## 4.2 H.E.S.S. - The High Energy Stereoscopic System

**Figure 4.5:** View of the full H.E.S.S. array with the four 12 m telescopes and the 28 m H.E.S.S. II telescope (Credit: H.E.S.S. Collaboration, Frikkie van Greunen)

The name of the H.E.S.S. experiment stands for High Energy Stereoscopic System and, at the same time, honours Victor Hess who discovered cosmic rays in 1912 with balloon flights. The H.E.S.S. experiment is located in the Khomas Highlands of Namibia at $\approx 1800$ meters above sea level. This location was chosen for its good weather situation, many cloudless nights, no background light from nearby cities and the direct view to the Galactic Centre. The H.E.S.S. telescope array, shown in Fig. 4.5, consists of five telescopes. The four 12 m telescopes (CT1 through CT4) are placed in a square formation with a side length of 120 m and a fifth larger telescope is located in the middle of the square. The telescope positions of CT1 - CT4 were optimised for a maximum sensitivity at the design energy threshold of 100 GeV for the four-telescope array. The fifth telescope CT5 with a mirror area of 614 $m^2$ decreases the energy threshold further due to its large collection area. The four-telescope array (phase I) has been taking data since 2003; the fifth telescope had its first light in July 2012. In this work only data collected during phase I are used, therefore all following information and discussions are referring to the four-telescope system only. The information given here is taken from Aharonian et al. (2006), if not mentioned otherwise. Further information on CT5 and the H.E.S.S. phase II can be found at the website of the H.E.S.S. experiment (Hofmann, 2012).
The reflector of each of the four H.E.S.S. phase I telescopes consists of 382 round mirror facets with a diameter of 60 cm which are mounted on a hexagonal dish structure with a flat-to-flat diameter of 12 m. This results in a reflector area of 108 $m^2$ for each telescope. The mirrors are arranged in Davies-Cotton layout (Davies & Cotton, 1957) to achieve good images of the shower also for showers further away from the optical axis. This is attained by all reflector facets having the same focal length $f$ equal to the focal length of the whole telescope and mounted on a sphere with radius $f$. The mirror facets consist of a glass substrate and are coated with aluminum and a protective quartz layer. Due to environmental influences like weather and sand, the reflectivity of the mirrors degrades over time and between April 2010 and October 2011 all mirrors of the four telescopes were replaced. Figure 4.6 shows the

dish structure of CT3 during the mirror exchange in April 2010. A detailed description of the mirror system and alignment can be found in Bernloehr et al. (2003) and Cornils et al. (2003).

**Figure 4.6:** The telescope CT3 during mirror exchange in April 2010. The round mirrors, each with a diameter of 60 cm, are mounted on a steel structure. The camera is positioned on a four-arm system in the focal plane with 15 m distance to the reflector plane.

Each camera of the four 12 m telescopes consists of photo-multiplier tubes and is mounted on a four-arm system at the focal distance of the telescope of 15 m. The photo-multiplier tubes are arranged in a hexagonal array and are enclosed by Winston Cones[3] (Welford & Winston, 1978) to collect the light that would fall between the tubes and also to limit the field of view to minimise the ambient background light. The field of view of a single photo-multiplies tube relates to 0.16° in diameter on the sky and all photo-multiplies tubes combined yield for the whole camera a field of fiew of 5°. The photo-multiplier tubes are grouped together in 60 drawers; each drawer consisting of 16 photo-multiplier tubes. These drawers contain the trigger and readout electronics for the tubes, as well as the high voltage supply, control and monitoring electronics. The sample rate for one photo-multiplier tube is 1 GHz.
The H.E.S.S. experiment phase I uses a two-level trigger system. The first-level trigger works at the camera level and the second-level trigger (central trigger) requires at least two telescopes triggering in the first level coincidently. The H.E.S.S. phase I trigger and readout system is described in detail in Funk et al. (2004).
The first-level trigger requires that a sector threshold and a pixel threshold within the camera are exceeded. The camera is divided into overlapping sectors with each sector containing 64 pixels. The sector threshold requires a signal in 3 PMTs in one camera sector. The pixel threshold requires more than four photoelectrons per pixel. The central trigger receives all individual first-level information from the individual cameras and triggers if there is a coincidence from two or more triggers within a time window of 80 ns. The second-level trigger reduces the read-out rate due to blocking night-sky background and single muon events.

[3] named after their inventor Roland Winston

H.E.S.S. observations are usually divided into single runs, each with 28 minutes of observation time. Each observation is checked for hardware problems or bad weather conditions that could affect the data quality before being used for further analysis. Good quality observations usually consist of $\approx 10^3$ triggered events. The camera images are stored and used for the reconstruction of the properties of the primary particle. But, before the shower images can be used for direction and energy reconstruction, the camera images are calibrated. That means, for each pixel the null levels of the photo-multiplier tubes, so-called pedestals, are subtracted and the amplitude is converted from ADC to photoelectron values. The calibration is described in detail in Aharonian et al. (2004).

### 4.2.1 Event reconstruction and selection

The standard analysis (Aharonian et al., 2006) cleans the camera images before the reconstruction and only those pixels containing more than $i$ photoelectrons and possessing a neighbour with more than $j$ photoelectrons are kept. These are the so-called "tail cuts". Usually, values of 5 photoelectrons, respectively 10 photoelectrons are used for $i$ and $j$. The shape of the cleaned shower image is approximately an ellipse and the shower images are parameterised with so-called *Hillas parameters* (Hillas, 1985). The *centre of gravity*, *image size*, *orientation* of the ellipse in the camera coordinate system, *length* and *width* are calculated. The image size is defined as the number of photoelectrons contained in the cleaned image. *Length* is the semi-major axis of the ellipse and *width* refers to the semi-minor axis as illustrated in Fig. 4.7.

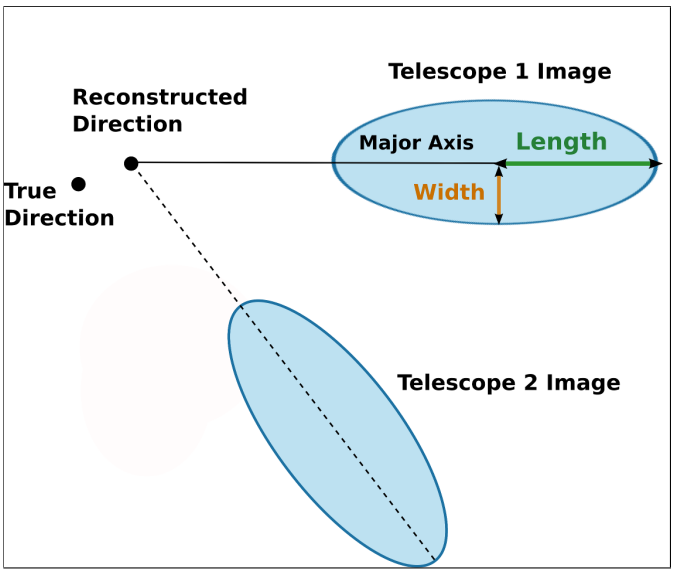


**Figure 4.7:** Schematic illustration of two shower images with the elliptic parametrisation. The width and length are the minor respectively major axis and the direction is reconstructed by the intersection of the major axes. Image adapted from Aharonian et al. (2006).

The *shower direction* is reconstructed by the intersection of the major axes of superimposed shower ellipses in the camera system. If the event is observed with more than two telescopes the intersection is made pairwise and the reconstructed direction is weighted according to the uncertainties in the involved camera images. The *impact distance* is defined as distance between impact point, where the extrapolated photon trajectory hits the ground, and the telescope and is derived from intersection of the major axes in the coordinate system of the telescope array.

The Hillas parameters of an event contain all information needed for the reconstruction of the shower direction, the depth of the shower maximum and the energy of the primary particle. The depth of shower maximum is calculated from atmospheric profiles using the height determined from the angular distance between the centre of gravity and the reconstructed direction and impact distance. The energy of the primary particle is determined from comparing the image size with Monte Carlo simulations depending on zenith angle, impact distance and optical efficiency.

As mentioned before, the mirror reflectivity and also the efficiency of the photo-multiplier tubes degrade with time and this decreases the image intensity compared with Monte Carlo simulation. This has to be taken into account deriving the particle energy from lookup tables and, therefore, the optical efficiency of the telescope system is monitored using single muon events. The degrading optical efficiency decreases the energy of the reconstructed particle and therefore a correction factor is applied. The detailed discussion on the energy correction can be found in Bolz (2004).

During the last years an advanced $\gamma$-ray likelihood reconstruction technique (de Naurois & Rolland, 2009) was developed, in the following referred to as "Model++ analysis". This method uses the derived Hillas parameters as starting point for a fitting procedure where real camera images are compared with predicted shower images that are calculated from a semi-analytical model of the Cherenkov light distribution in electromagnetic air showers. Semi-analytical shower model means that the distribution of charged particles in electromagnetic showers from Monte Carlo simulations are parametrised to get an analytical description. The primary particle properties like direction, impact, energy and depth of first interaction are derived in the fit.

The Model++ analysis provides better sensitivity to $\gamma$-ray induced air showers than the standard Hillas reconstruction and was, therefore, chosen for an in-depth analysis of the region around the supernova remnant 3C 391 (see Chapter 7). All information and equations in the following paragraphs, as not stated otherwise, are taken from de Naurois & Rolland (2009).

The properties of the primary particles are derived with a minimisation procedure that compares in each camera pixel the intensity of the real camera image with the predicted one from the model. The probability density (likelihood) $P(s|\mu, \sigma_\mathrm{p}, \sigma_\gamma)$ for observing a signal $s$ in a pixel for an expected value $\mu$ from the model prediction is described in Eq. 4.3. The photoelectron number $n$ is convolved with the photo-multiplier-tube resolution given by the width of the pedestal $\sigma_\mathrm{p}$ and the width of the single photo electron peak $\sigma_\gamma$.

$$P(s|\mu, \sigma_\mathrm{p}, \sigma_\gamma) = \sum_n \frac{\mu^n \exp(-\mu)}{n!\sqrt{2\pi(\sigma_p^2 + n\sigma_\gamma^2)}} \exp\left(-\frac{(s-n)^2}{2(\sigma_\mathrm{p}^2 + n\sigma_\gamma^2)}\right). \tag{4.3}$$

For each pixel the log-likelihood is defined as:

$$\ln L = -2 \cdot \ln P(s|\mu, \sigma_\mathrm{p}, \sigma_\gamma). \tag{4.4}$$

The Poisson distribution in Eq. 4.3 can be replaced for large $\mu$ by a Gaussian distribution with width $\sqrt{\mu}$ and the likelihood can be simplified to a convolution of two Gaussian distributions:

$$P(s|\mu \gg 0, \sigma_\mathrm{p}, \sigma_\gamma) \approx \frac{1}{\sqrt{2\pi(\sigma_\mathrm{p}^2 + \mu(1+\sigma_\gamma^2))}} \exp\left(-\frac{(s-\mu)^2}{2(\sigma_\mathrm{p}^2 + \mu(1+\sigma_\gamma^2))}\right). \tag{4.5}$$

The telescope log-likelihood is defined as the sum over the log-likelihood of all pixels:

$$\ln L_{\mathrm{tel}} = \sum_{i}^{N_{pix}} \ln L_i = -2 \sum_{i}^{N_{pix}} \ln P(s_i|\mu, \sigma_{\mathrm{p}}, \sigma_{\gamma}). \tag{4.6}$$

The minimisation procedure for obtaining the best parameters of the primary particle, such as direction, impact parameter, depth of first interaction and energy of the primary particle, uses this telescope log-likelihood. The optical efficiency of the telescope system, as monitored by single muon events, is taken into account at the event reconstruction level.
As already mentioned in Sec. 4.1.1, not only $\gamma$-rays induce air showers but also cosmic ray hadrons. The separation of $\gamma$-like events and hadronic (background) events takes place after the reconstruction. The differences in hadronic and electromagnetic shower images lead to a different quality of the fit of the camera image to an electromagnetic shower event. Figure 4.8 shows a simulated camera image of a 1 TeV $\gamma$-ray initiated air shower and of a 2.6 TeV proton induced one. The electromagnetic shower image has an elliptical shape and can be parametrised as an ellipse, whereas the image shape of an hadron induced air shower is more irregular because of the more complex shower evolution.

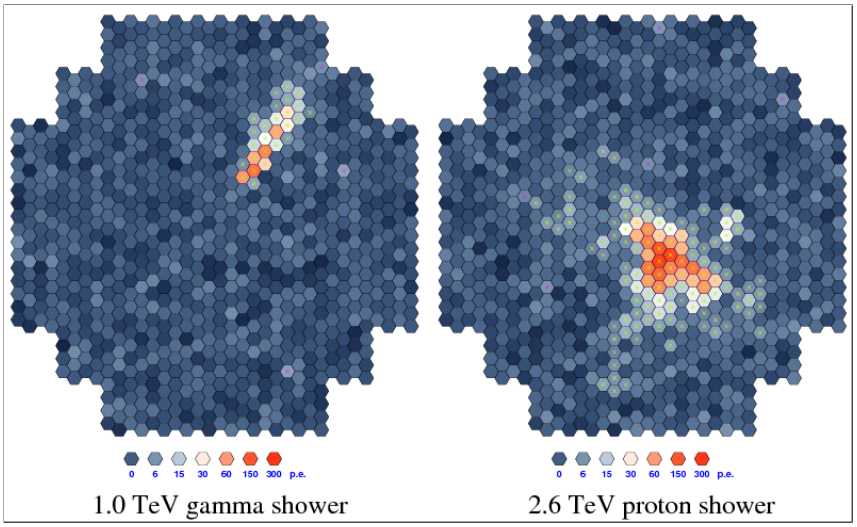


**Figure 4.8:** Camera image of a $\gamma$-ray initiated air shower and a hadron induced one. The shape of the electromagnetic shower image resembles an ellipse, whereas the image of the hadronic shower has a more irregular shape.
Image credit: Voelk & Bernloehr (2009).

For the discrimination of signal and background events a shower variable called *Goodness of Fit*, $G$, is defined as a normalised sum over all image pixels of the difference between the actual pixel log-likelihood and its expected value for an electromagnetic shower with the number of degrees of freedom $NdF$:

$$G = \frac{\sum_i^{N_{\mathrm{pix}}} [\ln L(s_i|\mu) - \langle \ln L \rangle|_{\mu_i}]}{\sqrt{2 \cdot NdF}}. \tag{4.7}$$

Similar to the Goodness of fit $G$ a variable *Shower Goodness* ($SG$) is defined that takes into account only pixels belonging to the shower core. The average value and variance of the $SG$ is stored in lookup tables as a function of image size and impact distance. The shower variable

**Table 4.1:** Selection criteria for $\gamma$/hadron separation for standard analysis, analysis of faint sources and loose selection for maximising the $\gamma$-ray efficiency of strong sources (de Naurois & Rolland, 2009). There are selection criteria applied to the minimal number of photoelectrons (min. charge), the maximum distance from the camera centre (max. nom. dist.), the number of triggered telescopes (tels), the mean scaled shower goodness (MSSG), the depth of first interaction ($t_0$) and the squared distance to the target position ($\theta^2_{\max}$).

| selection configuration | min. charge [p.e.] | max. nom. dist. [deg] | tels | $MSSG_{\max}$ | $t_0$ [$X_0$] | $\theta^2_{\max}$ [deg$^2$] |
|---|---|---|---|---|---|---|
| Standard | 60 | 2 | 2 | 0.6 | [-1,4] | 0.01 |
| Faint | 120 | 2 | 2 | 0.4 | [-1,4] | 0.005 |
| Loose | 40 | 2 | 2 | 0.9 | NA | 0.0125 |

*Mean Scaled Shower Goodness* ($MSSG$) is $G$ rescaled and the average for all telescopes $t$ is taken:

$$MSSG = \sum_t \frac{1}{\sqrt{N_{\text{Tel}}}} \left( \frac{G - \langle G \rangle}{\sigma_{\text{G}}} \right), \tag{4.8}$$

with the mean value $\langle G \rangle$ and the width of the distribution $\sigma_{\text{G}}$.
For a successful signal/background separation several selection criteria are used for each event the main separation is based on the $MSSG$ and the depth of first interaction $t_0$. Furthermore a selection on angular distance of the event to the target position ($\theta^2$) is applied. The criteria used in the Model++ analysis are summarised in Table 4.1. The different selection configurations are optimised for a standard analysis and for analysis of sources fainter than a few percent of the Crab flux, respectively. There is also the loose configuration for maximising the $\gamma$-ray efficiencies but with weaker background rejection.
The energy resolution for the Model++ analysis is better than 15% and in the central energy range between 500 GeV and 10 TeV even below 10%. The angular resolution depends on zenith angle, energy spectrum and optical efficiency, but typical values for the 68% containment radius of the point-spread function (PSF) are $0.06^\circ - 0.08^\circ$.

### 4.2.2 Signal identification and background subtraction

The potential $\gamma$-ray events are selected by applying constraints to the shower parameters of the reconstructed events. In the case of the Model++ analysis the selection configurations are listed in Table 4.1. But by the application of these cuts the background emission can not be fully removed. There are hadronic showers also passing the selection or diffuse $\gamma$-ray emission from hadrons interacting with interstellar material. To get rid of these events a background subtraction is applied. Apart from the region of interest, in the following also called "ON" region, there are one or more regions without any $\gamma$-ray sources chosen as "OFF" region(s). The level of events that passed the selection cuts within the OFF region is assumed to be equal to the number of background events in the ON region. The probable number of $\gamma$-ray excess events $N_\gamma$ is calculated as

$$N_\gamma = N_{\text{ON}} - \alpha N_{\text{OFF}}, \tag{4.9}$$

with the normalisation $\alpha$ to account for different observation times or geometrical areas for the ON and OFF regions. The significance $S$ of the excess events is calculated following Li &

Ma (1983) Eq. 17:

$$S = \sqrt{2}\left\{N_{\mathrm{ON}} \ln\left[\frac{1+\alpha}{\alpha}\left(\frac{N_{\mathrm{ON}}}{N_{\mathrm{ON}}+N_{\mathrm{OFF}}}\right)\right] + N_{\mathrm{OFF}} \ln\left[(1+\alpha)\left(\frac{N_{\mathrm{OFF}}}{N_{\mathrm{ON}}+N_{\mathrm{OFF}}}\right)\right]\right\}^{1/2}. \quad (4.10)$$

Li & Ma (1983) test the hypothesis, that there is no source and all observed $\gamma$ rays are background events with the maximum likelihood ratio method. If there are several trials $N$ to discover a $\gamma$-ray source, these trials have to be considered when discussing the so called "post-trial" significance of a certain source. The post-trial significance of a source can be determined by converting the pre-trial significance $S_{\mathrm{pre}}$ into a corresponding p-value $p_{\mathrm{pre}}$

$$p_{\mathrm{pre}} = \int_{S_{\mathrm{pre}}}^{\infty} \frac{1}{\sqrt{2\pi}} \exp\left(-\frac{x^2}{2}\right) \mathrm{d}x. \quad (4.11)$$

The pre- and post-trial p-values can be converted following

$$1 - p_{\mathrm{post}} = (1 - p_{\mathrm{pre}})^N. \quad (4.12)$$

Hence, the post-trial significance can be calculated from the post-trial p-value following Eq. 4.11.
All sources with a post-trial significance above $5\,\sigma$ are classified as firmely detected sources. For the estimation of the $\gamma$-ray excess in the ON region with reference to the OFF region one needs to consider that both regions may have different observation times, areas and also varying acceptance of events within the FoV of the camera. In general $\alpha$ is the ratio of the acceptance-weighted exposure integrated in time and angular space over the ON and OFF regions (Berge et al., 2007):

$$\alpha = \frac{\int_{ON} A^{\gamma}_{\mathrm{ON}}(x,y,z,E,t)\mathrm{d}x\mathrm{d}y\mathrm{d}z\mathrm{d}E\mathrm{d}t}{\int_{OFF} A^{\gamma}_{\mathrm{OFF}}(x,y,z,E,t)\mathrm{d}x\mathrm{d}y\mathrm{d}z\mathrm{d}E\mathrm{d}t}. \quad (4.13)$$

The $\gamma$-ray acceptance of the detector $A_{\mathrm{ON,OFF}}$ depends on the position $(x, y)$ in the field of view, the zenith angle $z$ of the observation, the energy $E$ of the event. The acceptance is assumed to be radial symmetric, but depends on the position in the field of view, the energy and zenith angle.
The aim of the background modeling is to estimate $\alpha$ and give $N_{\mathrm{OFF}}$, the number of events in the OFF region. An in-depth discussion of the $\gamma$-ray acceptance and different background techniques is given in Berge et al. (2007) and in the following only two background subtraction methods, the ring background and reflected background method, are discussed which are applied in the present work.

**Ring background**: In the ring background modeling the OFF region is chosen as a ring around a test position in celestial coordinates, as illustrated in Fig. 4.9(a). The method can be applied to any position in the FoV and is used mostly for the generation of significance or excess skymaps. The acceptance within the ring-shaped OFF region is not homogenous and therefore a correction of the acceptance has to be applied. $\alpha$ is the ratio of the ring area and the target area.
**Reflected background**: Most observations are taken in the so-called "wobble mode". The observation is not pointed directly to the region of interest but at a small offset (typically the offset is 0.5°) beside it. For the ON region there are $n$ OFF regions chosen with the same

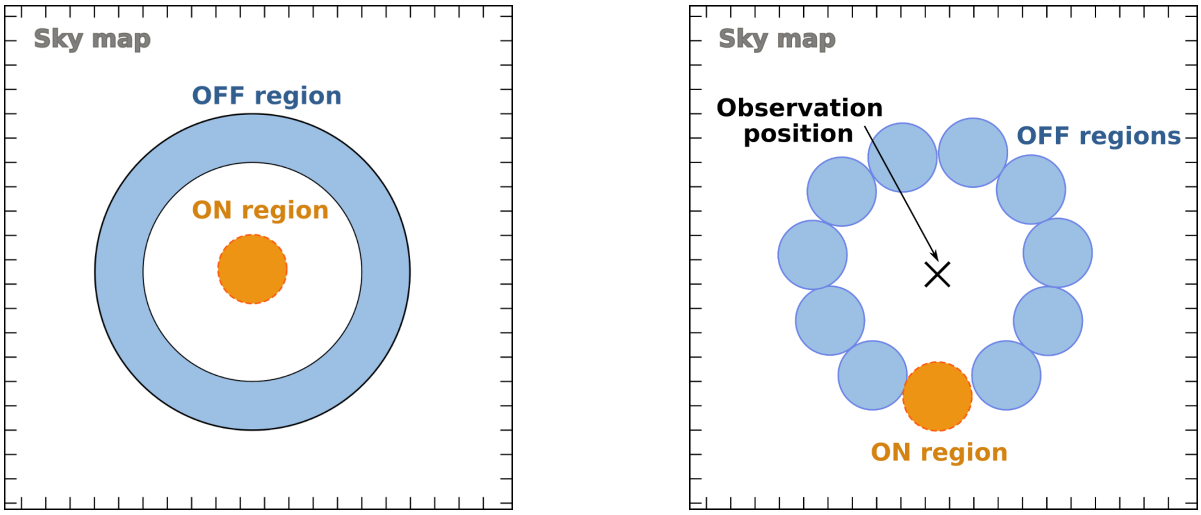


(a) Ring background method

(b) Reflected background method

**Figure 4.9:** Illustration of the ring background and reflected background methods. The illustrations are adapted from Berge et al. (2007)

distance to the camera centre as the ON region, forming a ring as illustrated in Fig. 4.9(b). The advantage of this method is that all OFF regions and the ON region have the same offset to the camera centre. Therefore, no further acceptance correction has to be taken into account and $\alpha$ is simply $1/n$. This background subtraction method is used to determine the $\gamma$-ray excess for the determination of the energy spectrum.
In both background modeling methods, regions which potentially contain $\gamma$-ray sources are excluded from the selection of OFF regions. Otherwise the level of background events is larger and the excess of $\gamma$-ray events is underestimated.

### 4.2.3 Spectrum determination

The flux of a $\gamma$-ray source and its energy distribution is an important tool to analyse which emission processes are taking place within a source. It can help to discriminate, for example, if the $\gamma$-ray emission from an observed supernova remnant is produced by accelerated leptons via inverse Compton scattering or by accelerated hadrons via pion decay. The differential source flux $F(E)$ is defined as the number of emitted $\gamma$-rays $N_\gamma$ per energy $E$, area $S$ and time $t$ interval:

$$F(E) = \frac{\mathrm{d}^3 N_\gamma(E)}{\mathrm{d}E\,\mathrm{d}S\,\mathrm{d}t}. \tag{4.14}$$

The energy here refers to the "true" energy of the emitted photons contrary to $E_{\mathrm{reco}}$, the energy that is reconstructed from the shower images. However, it is possible to get information on the underlying "true" energy spectrum using a foward-folding method (Piron et al., 2001). The basic principle is the folding of an assumed energy spectrum $F(E)$ with the effective area $A_{\mathrm{eff}}$ and the energy resolution $R_{\mathrm{E}}$ and multiplying this with the time interval $t_{\mathrm{obs}}$ to get a theoretical expected number of photons $n_{\mathrm{th}}$ for a given zenith angle $z$ and optical efficiency $o$ and the comparison of this number with the observed $\gamma$-ray excess. The following discussion of the spectrum determination is based on the H.E.S.S. internal documentation (de Naurois, 2014).
The number of expected excess counts $n_{\mathrm{th}}$ for an assumed spectral form $F(E)$ of the underlying

energy distribution can be calculated as

$$n_{\mathrm{th}} = t_{\mathrm{obs}} \cdot \int_{E_1'}^{E_2'} \mathrm{d}E' \int_0^{\infty} \mathrm{d}E\ F(E) \cdot A_{\mathrm{eff}}(E, z, \phi, o) \cdot R_{\mathrm{E}}(E, E', z, \phi, o). \tag{4.15}$$

This number is compared with the number of observed excess $\gamma$-rays in each energy bin and the difference between the observed and the expected number of events is quantified with a log-likelihood ($\mathrm{L} = \log(P)$) comparison. The probability $P$ to observe $N_{\mathrm{ON}}$ and $N_{\mathrm{OFF}}$ events when $N_\gamma$ excess events in a bin are expected is given by

$$P(N_{\mathrm{ON}}, N_{\mathrm{OFF}} \mid N_\gamma, N_{\mathrm{BG}}) = \frac{(N_\gamma + \beta N_{\mathrm{BG}})^{N_{\mathrm{ON}}}}{N_{\mathrm{ON}}!} e^{-(N_\gamma + \beta N_{\mathrm{BG}})} \cdot \frac{N_{\mathrm{BG}}^{N_{\mathrm{OFF}}}}{N_{\mathrm{OFF}}!} e^{-N_{\mathrm{BG}}}, \tag{4.16}$$

where $\beta$ is the ratio of the observation time for the ON and OFF regions and $N_{\mathrm{BG}}$ is the number of expected background events in the bin. This value is not known directly but chosen to maximise the log-likelihood $\mathrm{L} = \log(\mathrm{P})$ for a given $N_\gamma$. The uncertainties on the flux are determined from the covariance matrix of the fit.
The simplest form for the assumed underlying flux distribution can be described by a power law

$$F(E) = F_0 \left( \frac{E}{E_0} \right)^{-\Gamma}, \tag{4.17}$$

where $F_0$ is the normalisation of the energy flux at the reference energy $E_0$ and $\Gamma$ is called power-law index. Most spectral parameters depend on the reference energy. Therefore, $E_0$ is often set to the decorrelation energy at which the spectral parameters have the smallest uncertainties and are least uncorrelated.
The lower limit of the energy range for spectral determination is determined by the energy at which the effective area is 10 %. The upper energy limit is determined by the event with the highest reconstructed energy.
In the following the effective area and energy resolution are discussed.
**Effective Area:** The effective collection area $A_{\mathrm{eff}}$ is derived from Monte Carlo simulations and depends on energy $E$, zenith angle $z$, offset from the camera centre $\phi$, the optical efficiency $o$ and cuts used for the event selection.
The effective area of the analysis is determined from the effective area known from Monte Carlo simulations scaled with the ratio of the number of selected events during an analysis $N_{\mathrm{sel}}$ to the number of simulated events $N_{\mathrm{sim}}$ for the observation conditions:

$$A_{\mathrm{eff}} = \frac{N_{\mathrm{sel}}(E, z, \phi, o)}{N_{\mathrm{sim}}(E, z, \phi, o)} \cdot A_{\mathrm{MC}}(E, z, \phi, o). \tag{4.18}$$

Figure 4.10 shows exemplarily the dependencies of the effective area on the offset from the camera centre and on the zenith angle of the observation for standard cuts applied in the Model++ analysis. With increasing offset from the camera centre the effective area decreases in general as shown in Fig. 4.10(a). Figure 4.10(b) compares the effective areas for three different zenith angles. Increasing zenith angles of the observation lead to a shift in the energy range. At large zenith angles the photons emitted by the air shower have a longer way to propagate through the atmosphere and more emitted photons of the air showers are absorbed during the propagation through the atmosphere, which leads to a higher energy threshold. However, for air showers that emit more photons the effective area is increased due to the larger area on ground that is illuminated by the Cherenkov light cone at larger zenith angles.

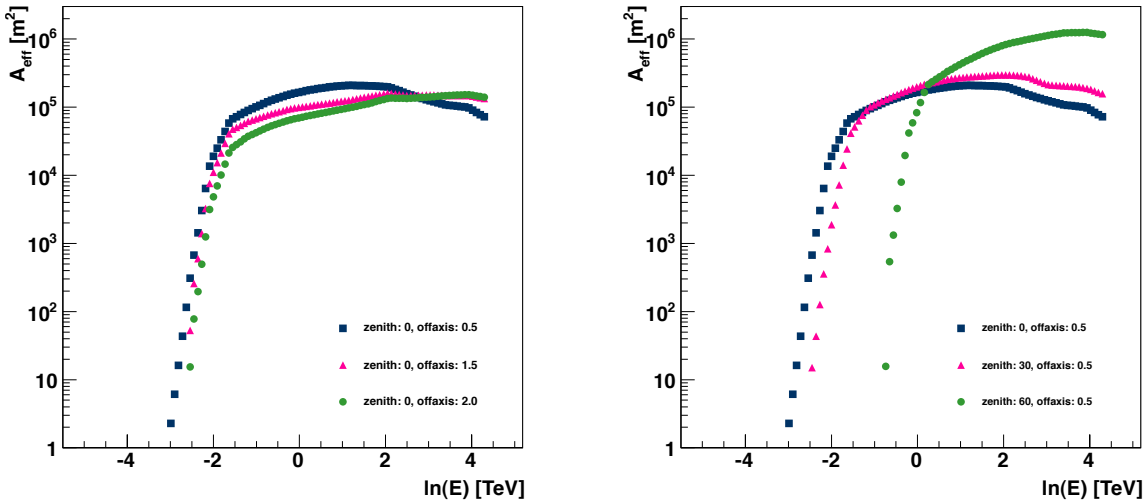


(a) The dependence of the effective area on energy and on the offset to the camera centre. This example shows the areas at zenith and 80% optical efficiency for offsets of 0.5° (blue), 0.5° (magenta) and 2.0° (green).

(b) The dependence of the effective area on energy and on the zenith angle of the observation. This example shows the areas for a fixed offset of 0.5° and 80% optical efficiency for zenith angles of 0° (blue), 30° (magenta) and 60° (green).

**Figure 4.10:** Two examples of the dependencies of the effective area $A_{\text{eff}}$ on the energy for various observation conditions.

**Energy Resolution:** The energy resolution $R_{\text{E}}$ can be described by a probability density function that is defined as the probability of observing an event with the reconstructed energy $E_{\text{reco}}$ that has a true energy $E_{\text{true}}$. It mainly depends on the zenith angle $z$, the true energy $E_{\text{true}}$ and the distance of the event to the camera centre. An exemplary distribution for a true energy $E_{\text{true}}$ of 10 TeV at a zenith angle of 30° and an offset of 0.5° is given in Fig. 4.11. The energy resolution is defined as the RMS of the $\Delta E/E_{\text{true}}$ distribution, with $\Delta E = E_{\text{reco}} - E_{\text{true}}$. The energy resolution for the Model++ analysis is better than 15 % for the whole energy range and in the central range (between 0.5 TeV and 10 TeV) better than 10 % (de Naurois & Rolland, 2009).

## 4.3 The H.E.S.S. Galactic Plane Survey

The H.E.S.S. Galactic Plane Survey is the largest connected data set of the inner Galaxy in the very-high-energy range and, therefore, very well suited for population studies. The $\gamma$-ray flux sensitivity and $\gamma$-ray significance maps of the H.E.S.S. Galactic Plane Survey are used in this work in Chapter 5 and Chapter 6 to test the spatial correlation of molecular clouds with $\gamma$-ray emission and to search for regions harbouring $\gamma$-ray emitting molecular clouds potentially detectable with H.E.S.S.

The H.E.S.S. Galactic Plane Survey covers the Galactic plane between 260° and 60° Galactic longitude and between −2.5° and +2.5° Galactic latitude. The data set consists of about 2800 hours of observations taken between 2004 and 2012. The data set of the H.E.S.S. Galactic Plane Survey has been analysed (Carrigan et al., 2013) using a multivariate analysis technique (Ohm et al., 2009) with a minimum image amplitude of 160 photoelectrons. This analysis has been cross-checked with the Model++ analysis described in Section 4.2.1. The exclusion

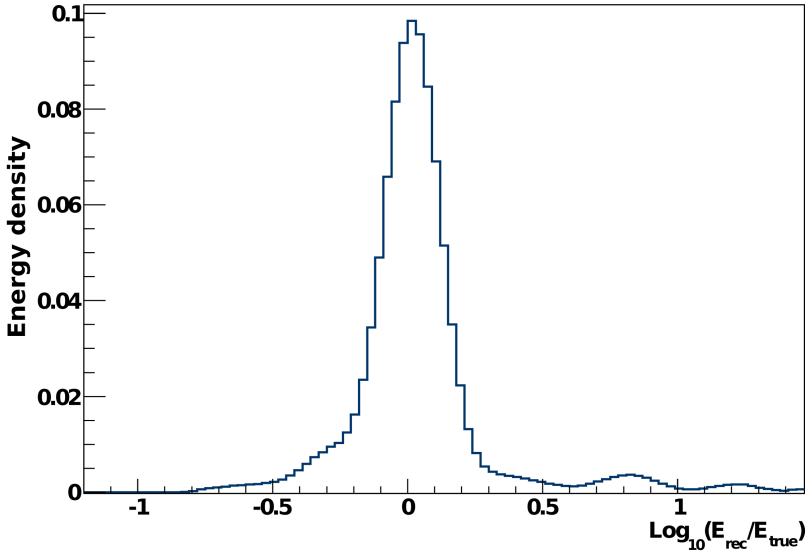


**Figure 4.11:** Energy density distribution of the reconstructed energy for events with a true energy of 10 TeV at a zenith angle of 30° and an offset of 0.5°.

regions are calculated using the adaptive method of Carrigan et al. (2012). Using an iterative approach, areas with known $\gamma$-ray emission are excluded from the background estimation. All maps generated from the data are produced using the ring-background method as described in Section 4.2.2 with a variable ring size (Carrigan et al., 2012). The significance for each bin of the sky map is calculated following Li & Ma (1983) as described in Section 4.2.2. The ON events within a predefined radius, in the following referred to as *correlation radius*, and the corresponding OFF events around each bin of the sky map are used for the calculation of significances. A correlation radius of 0.1° is suitable for point sources. For the search for extended emission also maps with the correlation radii of 0.2°, 0.3° and 0.4° were produced. The $\gamma$-ray sensitivity of the H.E.S.S. Galactic Plane Survey is not entirely uniform with regard to the Galactic longitude; the non-uniform distribution of measurement time over various regions of interest reults in a certain longitude dependence of the sensitivity. The sensitivity of the integral flux above 1 TeV for point-like sources, assuming a power-law spectrum with an index of 2.3, is better than 2% Crab Units (C.U.)[4] in the longitude range 283° to 59° at a latitude of −0.3° (Carrigan et al., 2013). For extended sources the flux sensitivity is worse than for point sources with the same flux as more background is collected due to the larger source region. The flux sensitivity for extended sources $S_{\text{extended}}$ can be aproximated as $S_{\text{extended}} = S_{\text{ps}} \cdot \theta_{\text{source}}/\theta_{\text{ps}}$, with the point-like sensitivity $S_{\text{ps}}$, the source extent $\theta_{\text{source}}$ and $\theta_{\text{ps}}$, the size of a point source.

A total of almost 150 TeV $\gamma$-ray sources are listed in the online catalogue TeVCat[5]. More than 60 of those sources were detected by H.E.S.S. and are located in the region covered by the H.E.S.S. Galactic Plane Survey. The H.E.S.S. sources, that are published or announced, are marked on the $\gamma$-ray significance map (Carrigan et al., 2013) in Fig. 4.12. The significance map shows the pre-trial significances using a correlation radius of 0.1°. A census of the $\gamma$-ray sources located in the region of the H.E.S.S. Galactic Plane Survey is shown in Fig. 4.13. Classification were adapted from TeVCat. In the following the individual source classes are

[4] here: $1\,\text{C.U.} = 2.26 \cdot 10^{-11}\,\text{cm}^{-2}\,\text{s}^{-1}$

[5] http://tevcat.uchicago.edu/

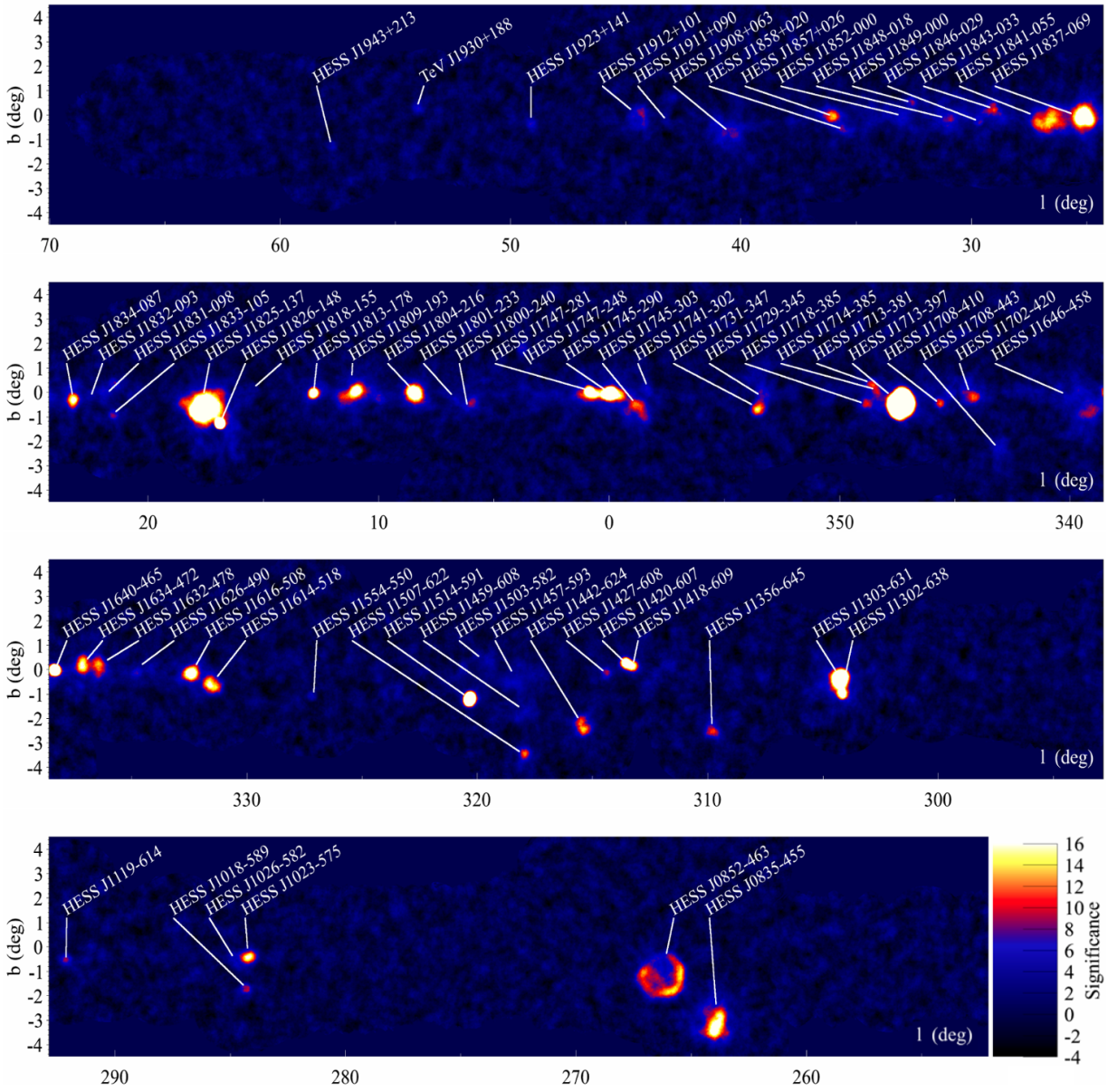


**Figure 4.12:** $\gamma$-ray significance map of the H.E.S.S. Galactic Plane Survey. The pre-trial significances using a correlation radius of 0.1° are shown. Published or announced H.E.S.S. sources are marked on the sky map. The image is taken from Carrigan et al. (2013).

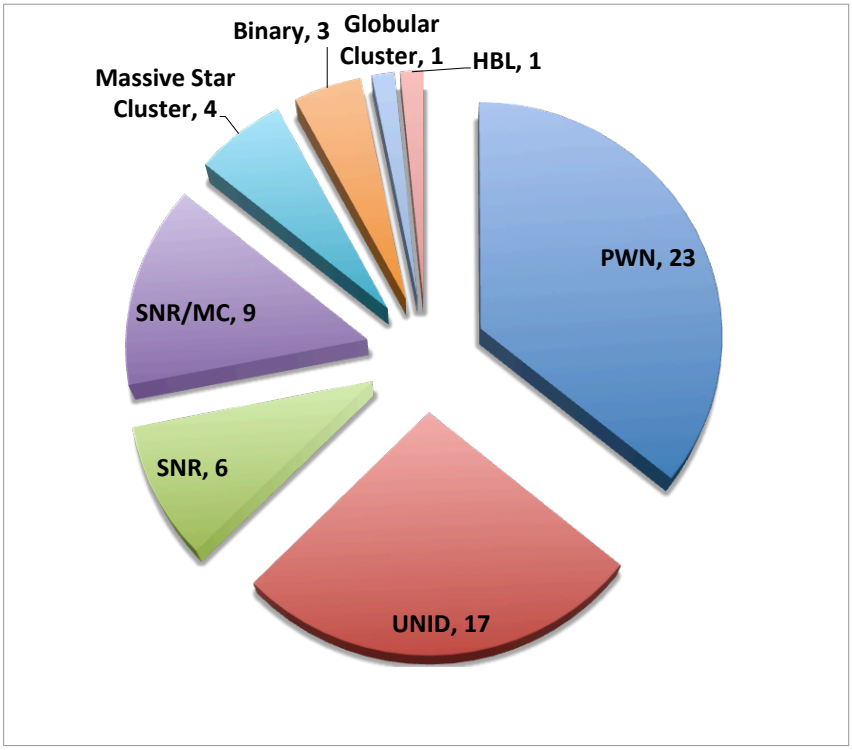


**Figure 4.13:** Classification of the H.E.S.S. sources within the range of the H.E.S.S. Galactic Plane Survey.

briefly introduced.

Pulsar wind nebulae (PWNe) are the largest source class. Pulsars are fast rotating neutron stars with high electric and magnetic fields. Pulsars lose their rotational energy via highly magnetised relativistic winds consisting of electrons and positrons. These winds form a bubble around the pulsar, the pulsar wind nebula. Pulsar wind nebulae are visible due to synchroton and inverse Compton emission in the radio, X-ray and TeV range. Pulsed $\gamma$-ray emission can be observed from the close vicinity of the pulsar and unpulsed emission from the pulsar wind nebula. The morphological appearance of the TeV emission of pulsar wind nebulae ranges from point-like, e.g., G21.5-0.9, to very extended, e.g., Vela X. This depends both on the evolutionary stage and on the age of the pulsar wind nebula and on its distance to Earth. More detailed information on the formation and evolution of pulsar wind nebulae can be found, e.g., in Gaensler & Slane (2006).

From six supernova remnants (SNR) TeV emission is observed, one with composite morphology and five supernova remnants where a shell is revealed. As discussed in detail in Section 2, particles get accelerated at the shock front formed after a supernova explosion. The observed TeV emission can originate either from leptons via inverse Compton scattering off low-energy photons or from hadrons interacting with the interstellar medium and producing $\gamma$-rays via pion decay.

Nine sources are classified as supernova remnant/molecular clouds interactions (SNR/MC). Molecular clouds interacting with the shock of a supernova remnant, as discussed in Section 3.3, as well as illuminated clouds offset from the supernova remnant, as described in Section 3.4, fall into this category. The most prominent example observed in the TeV energy band is the W28 region.

Four $\gamma$-ray sources belong to the category of stellar clusters among them Westerlund 1 and Westerlund 2. Stellar clusters contain young stars formed from the same giant molecular

cloud. The stars are loosely bound by gravitation and have a similiar age. Massive stellar clusters usually contain hot and massive Wolf-Rayet and OB stars. Their winds could be potential acceleration sites in single, binary or collective processes. Furthermore, stellar clusters also harbour pulsars and pulsar wind nebulae as well as remnants from previous supernova explosions. Thus, stellar clusters hold many individual potential acceleration sites as well as collective mechanisms like the collective cluster wind. More details on stellar clusters can be found, e.g., in Abramowski et al. (2012) for the example of Westerlund 1.
Contrary to stellar clusters, globular clusters contain old stellar systems. One $\gamma$-ray source is associated with a globular cluster, Terzan 5 (Abramowski et al., 2011). The emission possibly originates from the population of millisecond pulsars accumulated in the a globular cluster.
The TeV emission of three binary systems is observed in the region covered by the H.E.S.S. Galactic Plane Survey. A binary system often contains a compact object, such as a neutron star or stellar black hole, and a massive stellar companion. The $\gamma$-ray emission is variable on the timescale of the orbital period. Two potential acceleration sites are under discussion for the origin of the observed emission. One scenario is the interaction between the wind of the massive star and the wind of the pulsar, if the compact companion is a pulsar, forming a shock where particles are accelerated. The second scenario includes accretion of material from the stellar companion and the formation of jets. The potential acceleration mechanisms are discussed in depth, e.g., in the recent review by Dubus (2013).
At least one extragalactic source is located in the region covered by the H.E.S.S. Galactic Plane Survey, namely one high-frequency peaked BL Lac (HBL) object. This one source is located by chance in the Galactic plane and is no real Galactic source. BL Lac objects belongs to the class of active galactic nuclei. Galaxies harboring a supermassive black hole accreting matter are classified as active galactic nuclei. Most active galactic nuclei observed in the TeV range belong to the class of blazars, active galactic nuclei with a relativistic jet pointed directly to the observer. Detailed information on active galactic nuclei and potential emission mechanism for the TeV energy range as well as prospects for future imaging Cherenkov telescopes can be found, e.g., in the recent review of Reimer & Böttcher (2013).
A large fraction of the TeV sources listed in the TeVCat catalogue and located within the region of the H.E.S.S. Galactic Plane Survey are classified as unidentified, which means they either do not posses a clear counter part at other wavelengths or, on the contrary, are located in a very crowded field with too many potential multiwavelength associations.
The H.E.S.S. Galactic Plane Survey was introduced in this Section as the $\gamma$-ray flux sensitivity and $\gamma$-ray significance maps are used in Chapter 5 and Chapter 6. The census of the TeV sources located within the region covered by the H.E.S.S. Galactic Plane Survey is listed above to give an overview which kind of objects are visible in the TeV domain and indicate the presence of accelerated particles, both leptons and hadrons.

CHAPTER 5

# Spatial coincidence of gamma-ray emission with molecular clouds

The H.E.S.S. Galactic Plane Survey provides the largest connected data set of the inner Galactic Plane in the energy range above 100 GeV, therefore, it is very well suited for population studies. Molecular clouds provide a good target for hadrons of the cosmic-ray sea and hadrons accelerated in supernova remnants as discussed in Chapter 3. The $\gamma$-ray emission is produced via proton-proton interaction and subsequent neutral pion decay. So far, nine $\gamma$-ray sources have been classified as supernova-remnant/molecular cloud association within the H.E.S.S. Galactic Plane Survey. The analysis presented in this Chapter studies the spatial coincidence of molecular clouds of the Galactic Ring Survey with $\gamma$-ray emission in the H.E.S.S. Galactic Plane Survey to test if there is a statistically significant relation between those clouds and the $\gamma$-ray emission.
The molecular clouds identified in the Galactic Ring Survey are used in this study and the properties of these molecular clouds are introduced in Section 5.1. In Section 5.2 the criterion for spatial coincidence of these molecular clouds with observed $\gamma$-ray emission in the H.E.S.S. Galactic Plane Survey is discussed. It is expected that a large fraction of molecular clouds is coincident by chance with observed emission. The level of random coincidences is estimated in Section 5.3 using simulated populations of molecular clouds. An interpretation of the derived results is given in Section 5.4 and a brief conclusion in Section 5.5.

## 5.1 Molecular clouds of the Galactic Ring Survey

The Boston University - Five College Radio Astronomy Observatory (BU-FCRAO) Galactic Ring Survey (GRS) is a survey of $^{13}$CO emission that covers the region between 18° and 56° Galactic longitude and between −1° and +1° Galactic latitude (Jackson et al., 2006), a total area of about 75.4 deg$^2$. In the following, this survey is referred to as Galactic Ring Survey. The angular resolution is 46″ and the survey was sampled on a 22″ grid. The data set consists of 1 993 552 individual spectra. A total of 829 MCs and 6124 clumps have been identified within the data of the Galactic Ring Survey by Rathborne et al. (2009)

using a modification of the cluster finding algorithm CLUMPFIND (Williams et al., 1994). The algorithm searches through the three-dimensional data cube in longitude, latitude and velocity space for iso-brightness surfaces to identify emission features. To each identified cloud or clump a two-dimensional ellipse was fitted to parametrise the extent and position of the individual cloud or clump. The minor and major axes of the ellipses are equivalent to the projected cloud extent in those directions. Clumps are smaller, denser sites within molecular clouds where individual starformation occurs. The clumps have a mean size of 0.03° (Rathborne et al., 2009) which is much smaller than the angular resolution of current imaging Cherenkov telescope systems. During this work only the molecular clouds, not the clumps, identified in the Galactic Ring Survey are used. A selection of cloud properties are listed in Tab. 5.1.

**Table 5.1:** Selected properties of the molecular clouds of the Galactic Ring Survey. These values are taken from Table 4 in Rathborne et al. (2009).

| Properties | Min. | Max. | Mean | Std. dev. | Median |
|---|---|---|---|---|---|
| Linewidth [$\mathrm{km\,s^{-1}}$] | 0.6 | 9.8 | 3.6 | 1.4 | 3.4 |
| Semi-major Axis [°] | 0.06 | 1.16 | 0.41 | 0.15 | 0.41 |
| Semi-minor Axis [°] | 0.05 | 0.53 | 0.23 | 0.09 | 0.22 |
| Radius [pc] | 1.6 | 97.5 | 24.1 | 12.5 | 22.6 |
| $\log_{10}$(Density / $1\,\mathrm{cm^{-3}}$) | 0.6 | 2.8 | 1.7 | 0.4 | 1.7 |

Roman-Duval et al. (2009) determined for 750 molecular clouds of the Galactic Ring Survey the distance of the cloud to Earth solving the distance ambiguity by looking in neutral hydrogen emission data for self-absorption features. The masses of these 750 molecular clouds have been estimated by Roman-Duval et al. (2010). According to Roman-Duval et al. (2010) the molecular cloud population is affected by a Malmquist bias[1] due to the completeness limit increasing with distance. The authors estimated a minimum mass $M_{\mathrm{min}}$ for completeness of $M_{\mathrm{min}} = 50 d_{\mathrm{MC}}^2\,(\mathrm{M_\odot/kpc^2})$, with $d_{\mathrm{MC}}$ denoting the distance of the molecular cloud to Earth. Only clouds with a mass larger than the corresponding minimum mass are detectable within the Galactic Ring Survey. Emission from clouds with smaller masses than, for example, $200\,\mathrm{M_\odot}$ at a distance of 2 kpc or $5 \cdot 10^3\,\mathrm{M_\odot}$ at a distance of 10 kpc cannot be observed. Therefore, the catalogue below the minimum mass is not complete and suffers from observation bias. The catalogue is also affected by finite resolution and the method used to identify molecular clouds, as the applied algorithm detects well resolved, nearby molecular clouds as distinct objects, however, the same objects at much larger distances would be blended together and appear as one object (Roman-Duval et al., 2010).
Nevertheless, both biases discussed above do not affect the results derived in this work. This work studies $\gamma$-ray emitting molecular clouds in the TeV range and the expected $\gamma$-ray flux is proportional to the mass of the cloud over the distance squared. The minimum $\gamma$-ray flux originates from passive molecular clouds only embedded in the cosmic ray sea. Yet, it is not expected to detect any $\gamma$-ray emission from passive clouds with H.E.S.S. due to the low fluxes even for molecular clouds identified in the Galactic Ring Survey with the largest masses and small distances. Molecular clouds, that are not even observable in the radio band, are not expected to be detectable in TeV $\gamma$-rays. Therefore, the observation bias in the radio band does not influence much the results derived in this work for the TeV energy band. The

[1] A Malmquist bias describes the effect that systematically brighter objects are observed with increasing distance. It is named after the Swedish astronomer Gunnar Malmquist, but according to, e.g., Butkevich et al. (2005) that kind of effect was first discussed by Eddington (1913).

angular resolution of the H.E.S.S. Galactic Plane Survey is about one order of magnitude worse than the resolution in the radio band, hence, the finite resolution in the radio band is more than sufficient and the limitations are due to the worse resolution in the TeV band.

The Galactic Ring Survey is not the only Galactic radio survey with publicly available data, but it provides the largest published catalogue of molecular clouds with estimated masses and distances. The CO emission survey by Dame et al. (2001) covers the whole Galactic plane, but an identification of molecular clouds and determination of the distances and clouds from this survey are beyond the scope of this thesis. Therefore, the molecular cloud catalogue of the Galactic Ring Survey is used for studies in this work, even though it covers only about one quarter of the region of the H.E.S.S. Galactic Plane Survey.

## 5.2 Spatial matching of molecular clouds with gamma-ray emission in the H.E.S.S. Galactic Plane Survey

The aim of the analysis presented in this chapter is to test if there is a significant level of spatial coincidence of observed $\gamma$-ray emission in the H.E.S.S. Galactic Plane Survey with molecular clouds. If so, this would establish a connection between molecular clouds and sources of the H.E.S.S. Galactic Plane Survey. The sample of molecular clouds tested are the clouds identified within the Galactic Ring Survey with estimated masses and distances as introduced in Section 5.1.
In this work a cloud is defined to spatially match observed $\gamma$-ray emission, if the maximum significance from the H.E.S.S. Galactic Plane significance sky map is larger than $7.5\,\sigma$ within the region of the elliptic representation of the cloud. This is a very loose criterion, but so far associations of $\gamma$-ray emission with molecular clouds in case of supernova remnant/molecular cloud associations were mainly derived by the spatial matching of $\gamma$-ray emission and molecular line emission in the radio band and the exclusion of other counterparts. The individual morphology of each cloud is not available from catalogue data, therefore, the elliptic representation is taken for this test. The threshold of $7.5\,\sigma$ is chosen because the significance sky map covering the region of the Galactic Ring Survey has 192 800 bins and the post-trial significance of a pre-trial significance of $7.5\,\sigma$, even for $3 \cdot 192\,800$ trials, is larger than $5\,\sigma$, the treshold for detection of $\gamma$-ray emission. The factor 3 is chosen to allow the testing of more than one significance sky map generated with different correlation radii. Figure 5.1 shows the significance map of the H.E.S.S. Galactic Plane Survey generated with a correlation radius of 0.2° (Carrigan et al., 2013) overlaid with green ellipses representing all molecular clouds from the Galactic Ring Survey with estimated masses and distances. Appliying the defined coincidence criterion defined above, 294 of the 750 molecular clouds are spatially coincident with observed $\gamma$-ray emission on the $\gamma$-ray significance map with a correlation radius of 0.2°.

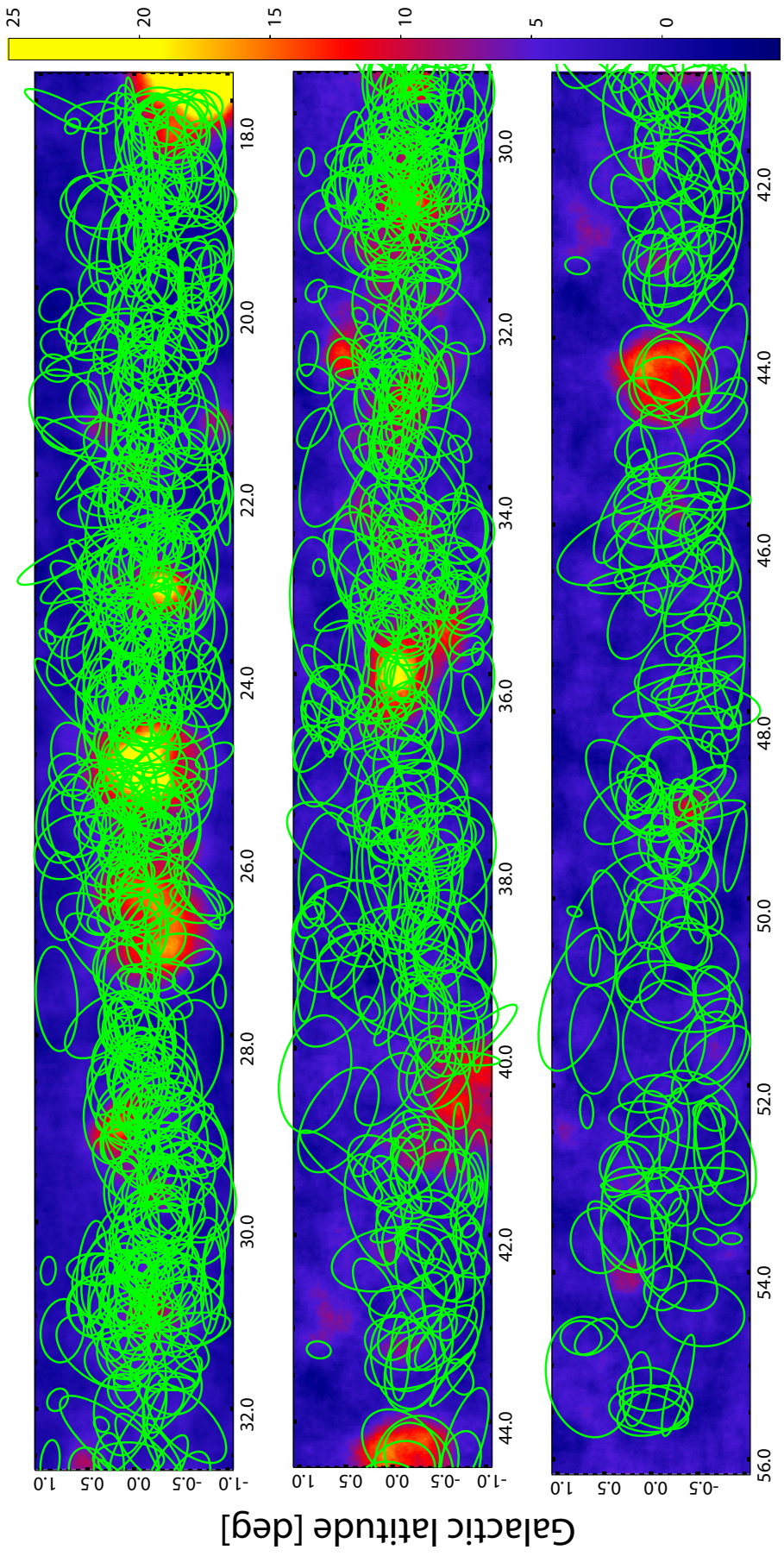


**Figure 5.1:** $\gamma$-ray significance map generated with a correlation radius of 0.2° (Carrigan et al., 2013). The ellipses for 750 molecular clouds from the Galactic Ring Survey are overlaid in green.

The fraction of molecular clouds spatially coincident with $\gamma$-ray emission is shown in Fig. 5.2 for different values of $M_{\mathrm{MC}}/d_{\mathrm{MC}}^2$, with $M_{\mathrm{MC}}$ the mass of the molecular cloud and $d_{\mathrm{MC}}$ its distance. The fraction of spatially coincident molecular clouds is shown in dependency of $M_{\mathrm{MC}}/d_{\mathrm{MC}}^2$, since the expected $\gamma$-ray flux from passive molecular clouds or molecular clouds near supernova remnants is directly proportional to this quantity as discussed in Chapter 3. The bin size for the bins in $\log_{10}[(M_{\mathrm{MC}}/d_{\mathrm{MC}}^2)/(\mathrm{M}_\odot/\mathrm{kpc}^2)]$ was chosen apriori and the bins are equidistant. The blue, solid error bars give the confidence interval at a 68.27% confidence level (CL), the black dashed ones at the 95.45% confidence level and the dotted ones at the 99.73% confidence level. For a one-dimensional Gaussian distribution these levels would refer to the $1\,\sigma$, $2\,\sigma$ and $3\,\sigma$ uncertanties.

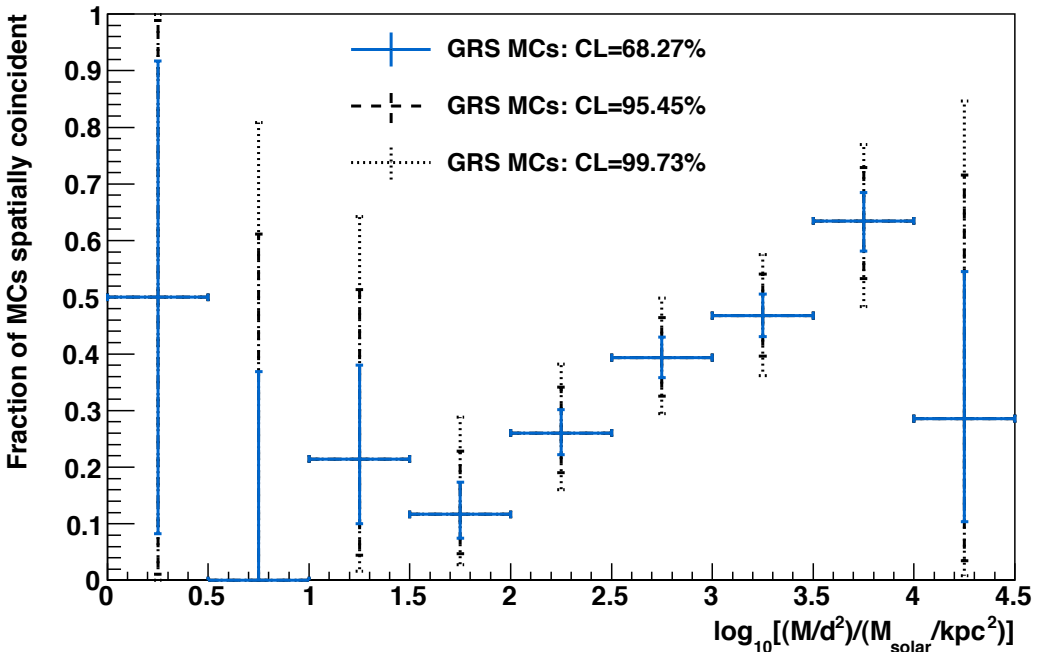


**Figure 5.2:** Fraction of molecular clouds (MCs) from the Galactic Ring Survey (GRS) spatially coincident with $\gamma$-ray emission in the H.E.S.S. Galactic Plane Survey. A threshold of $7.5\,\sigma$ was applied to a $\gamma$-ray significance map with a correlation radius of 0.2°.

The confidence intervals of the fraction of spatially coincident clouds are estimated for a binomial distribution according to Clopper & Pearson (1934). For each bin in $M_{\mathrm{MC}}/d_{\mathrm{MC}}^2$, there is a sample consisting of $n$ molecular clouds of which $m$ clouds are spatially coincident with $\gamma$-ray emission. The fraction of coincident clouds from the sample is denoted by $p = m/n$. The probability $P$ of $r$ clouds to be spatially coincident out of a sample of $n$ clouds can be estimated using the binomial probability density (see, e.g., Barlow, 1989) as

$$P(r;p,n) = p^r(1-p)^{n-r}\frac{n!}{r!(n-r)!}. \tag{5.1}$$

For the construction of the confidence intervall the lower limit $p_-$ and upper limit $p_+$ on $p$ are searched for. The limits on $p$ are given such way (Barlow, 1989) that

$$\sum_{r=m+1}^{n} P(r;p_+,n) = 1-\frac{1-\mathrm{CL}}{2} \quad \text{and} \quad \sum_{r=0}^{m-1} P(r;p_-,n) = 1-\frac{1-\mathrm{CL}}{2}, \tag{5.2}$$

with the given confidence level CL and $m$ clouds spatially coincident from a sample of $n$ clouds.
The results in Fig. 5.2 indicate that the fraction of clouds spatially coincident with $\gamma$-ray emission above the threshold of $7.5\,\sigma$ is rising with increasing values of $M_{\mathrm{MC}}/d^2_{\mathrm{MC}}$. The cloud mass is correlated with the size of the elliptic representation of the molecular cloud as shown in the following section. The criterion of spatial coincidence, as defined here, prefers clouds with larger areas. Therefore, a general increase of the fraction of spatially coincident clouds is expected and not all clouds fulfilling the coincidence criterion are related to the observed $\gamma$-ray emission. Hence, the level of random coincidences has to be estimated.

## 5.3 Estimation of the level of random coincidences

Figure 5.2 shows the fraction of molecular clouds of the Galactic Ring Survey that is coincident with $\gamma$-ray emission in dependence of $M_{\mathrm{MC}}/d^2_{\mathrm{MC}}$. Most of these clouds are expected not to be correlated with the observed emission but to be coincident with it by chance. The fraction of random coincidences is estimated in this section using simulated populations of molecular clouds.

Table 5.2 lists the correlations between the properties of the molecular clouds identified in the Galactic Ring Survey. The longitude and latitude position of the cloud as well as the angle of the ellipse are independent of each other. Therefore, these properties are simulated independently. The cloud mass over the squared distance, $M_{\mathrm{MC}}/d^2_{\mathrm{MC}}$, is weakly correlated with the cloud position, especially the Galactic longitude as the more massive molecular clouds are slightly more often located at lower Galactic longitude values. Since, the $\gamma$-ray emission in the H.E.S.S. Galactic Plane Survey is stronger at lower values of Galactic longitude this trend is considered in the simulation of the molecular cloud populations.

**Table 5.2:** Correlation matrix for the different properties of the cloud sample of the Galactic Ring Survey. The correlation coefficients are given in %. The semi-major axis is denoted by A, the semi-minor axis by B, respectively.

| | Longitude | Latitude | A | B | Angle | $M_{\mathrm{MC}}/d^2_{\mathrm{MC}}$ |
|---|---|---|---|---|---|---|
| Longitude | 100 | −7 | −1 | −7 | 5 | −14 |
| Latitude | −7 | 100 | −1 | −8 | −6 | −9 |
| A | −1 | −1 | 100 | 56 | −1 | 23 |
| B | −7 | −8 | 56 | 100 | 5 | 51 |
| Angle | 5 | −6 | −1 | 5 | 100 | 1 |
| $M_{\mathrm{MC}}/d^2_{\mathrm{MC}}$ | −14 | −9 | 23 | 51 | 1 | 100 |

The distributions of the cloud position, i.e. longitude and latitude, the angle of the cloud ellipse and $M_{\mathrm{MC}}/d^2_{\mathrm{MC}}$ are parameterised using the kernel density estimation (KDE), also called Parzen-Rosenblatt window method (Rosenblatt, 1956; Parzen, 1962). The kernel density estimator describes the shape of a sample distribution according to Parzen (1962) as

$$f_{\mathrm{n}}(x) = \frac{1}{nh}\sum_{j=1}^{n} K\left(\frac{x - x_{\mathrm{i}}}{h}\right), \tag{5.3}$$

with a sample $(x_1, x_2, ...x_n)$, the bandwidth $h$ and the kernel function $K$. Kernel functions are symmetric functions and the integral over the kernel function is normalised to 1. For the kernel density estimations used in this work the normal distribution is used as kernel function. The bandwidth was adjusted for each parameter distribution.
The kernel density estimation method was chosen, since the distributions of Galactic longitude, Galactic latitude, angle of the cloud ellipse and $M_{MC}/d_{MC}^2$ are not necessarily following any predefined probability distributions or functions. The density of molecular clouds at certain longitude position, for example, depends on the projection of the Galactic spiral arm structures onto the Galactic plane. The individual distributions and the derived kernel density estimations are shown in Fig. 5.3 for the longitude, latitude and angle distributions of the cloud ellipses. The distributions of $M_{MC}/d_{MC}^2$ in dependence of the Galactic longitude are shown in Fig. 5.4 and 5.5. The properties of the simulated molecular cloud populations are sampled from the derived kernel density estimations of those parameters.

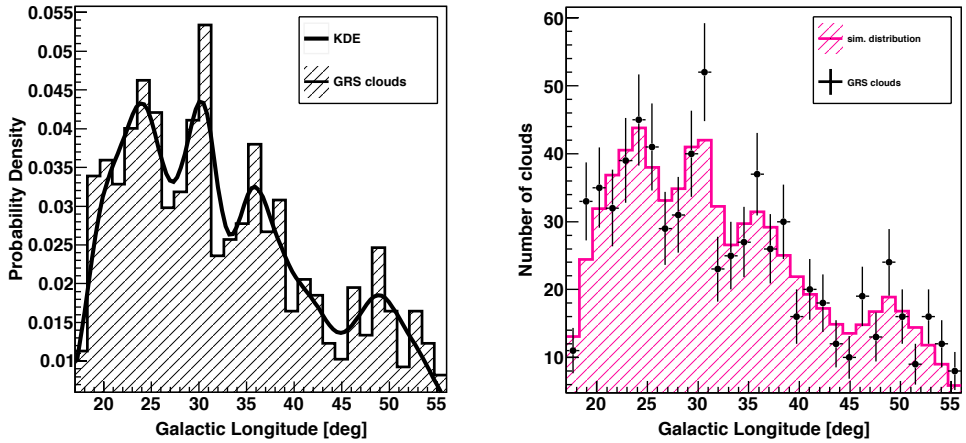


(a) Galactic longitude position of the molecular clouds.

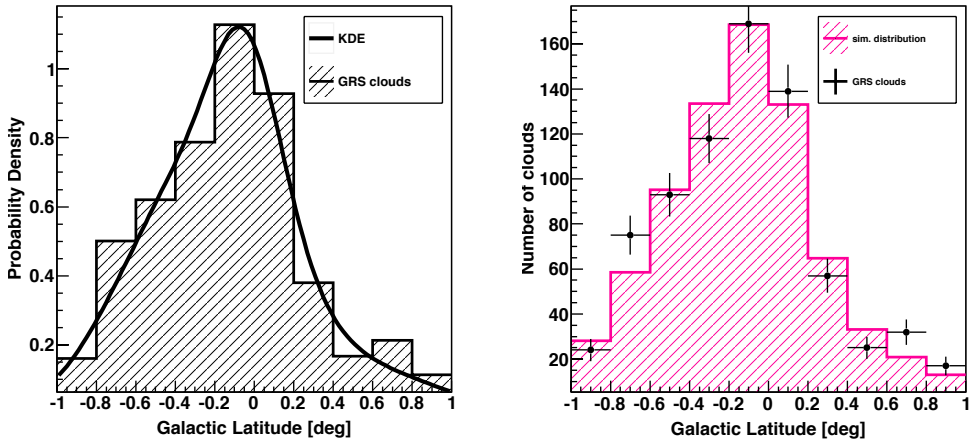


(b) Galactic latitude position of the molecular clouds.

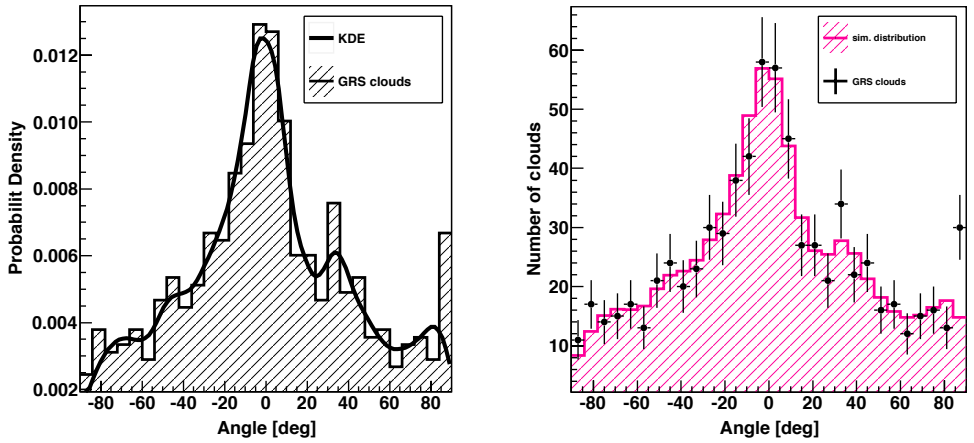


(c) Angle of the ellipse of the molecular clouds.

**Figure 5.3:** The distribution of Galactic longitude, Galactic latitude and angle for the molecular clouds of the Galactic Ring Survey and distributions obtained from the kernel density estimation. *Left*: Kernel density estimation (KDE) shown with the solid black line obtained from the normalised distributions of properties of the molecular clouds (black cross-striped) of the Galactic Ring Survey (GRS). *Right*: Distribution of the cloud parameters of the Galactic Ring Survey sample (black data points) and a simulated distribution of the parameter obtained from the KDE (magenta cross-striped) normalised to 750 clouds.

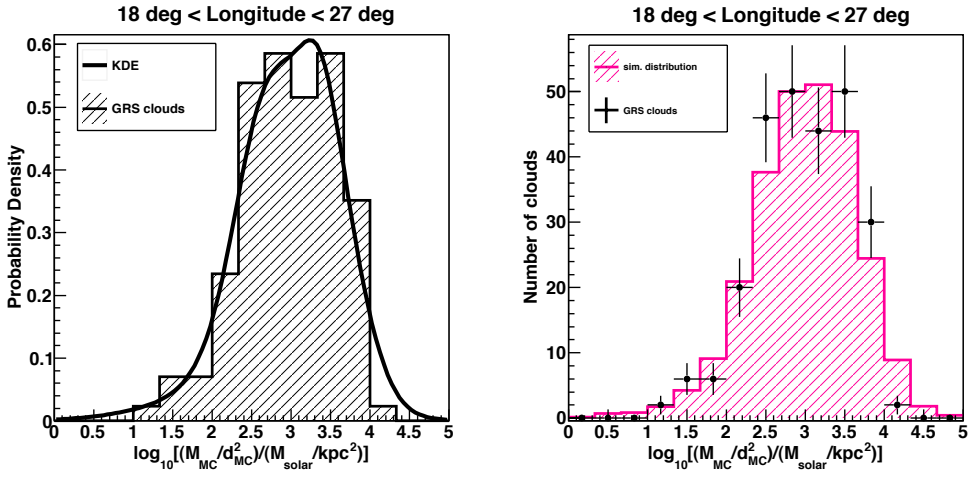


(a) $M_{\mathrm{MC}}/d^2_{\mathrm{MC}}$ for the Galactic longitude between 18° and 27°.

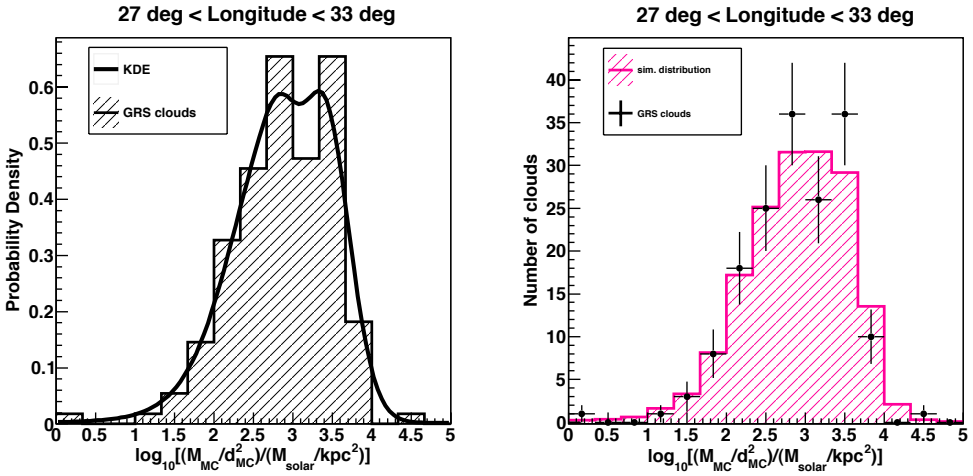


(b) $M_{\mathrm{MC}}/d^2_{\mathrm{MC}}$ for the Galactic longitude between 27° and 33°.

**Figure 5.4:** The distribution of $M_{\mathrm{MC}}/d^2_{\mathrm{MC}}$ in dependency of the Galactic longitude for the molecular clouds of the Galactic Ring Survey and distributions obtained from the kernel density estimation for the region between 18° and 33° Galactic longitude. *Left*: Kernel density estimation (KDE) shown with the solid black line obtained from the normalised distributions of properties of the molecular clouds (black cross-striped) of the Galactic Ring Survey (GRS). *Right*: Distribution of the cloud parameters of the Galactic Ring Survey sample (black data points) and a simulated distribution of the parameter obtained from the KDE (magenta cross-striped) normalised to 750 clouds.

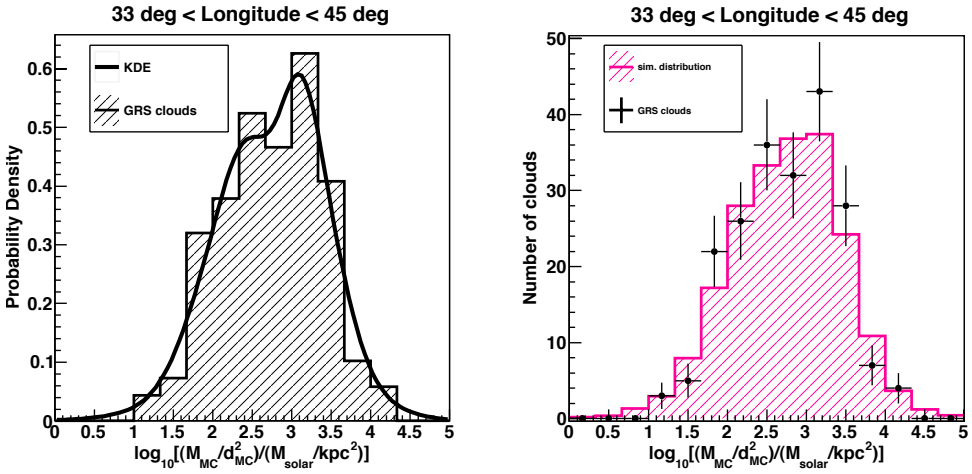


(a) $M_{\mathrm{MC}}/d^2_{\mathrm{MC}}$ for the Galactic longitude between 33° and 45°.

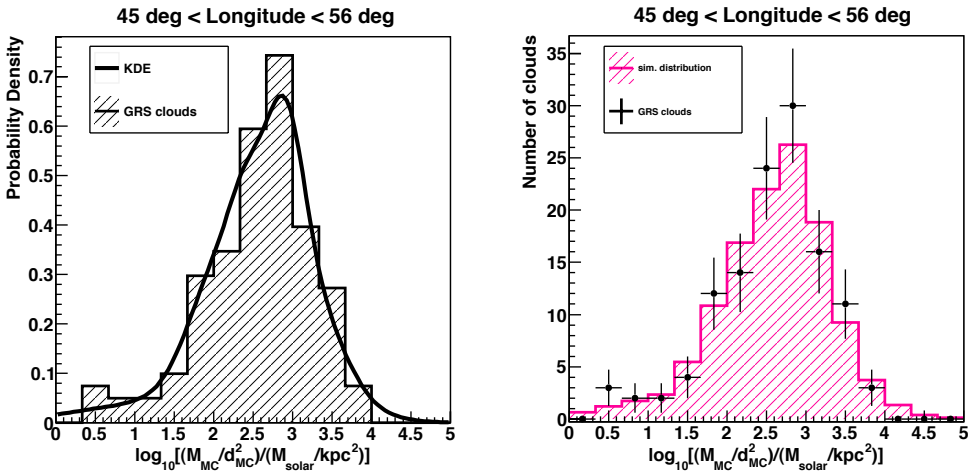


(b) $M_{\mathrm{MC}}/d^2_{\mathrm{MC}}$ for the Galactic longitude between 45° and 56°.

**Figure 5.5:** The distribution of $M_{\mathrm{MC}}/d^2_{\mathrm{MC}}$ in dependency of the Galactic longitude for the molecular clouds of the Galactic Ring Survey and distributions obtained from the kernel density estimation for the region between 33° and 56° Galactic longitude. *Left*: Kernel density estimation (KDE) shown with the solid black line obtained from the normalised distributions of properties of the molecular clouds (black cross-striped) of the Galactic Ring Survey (GRS). *Right*: Distribution of the cloud parameters of the Galactic Ring Survey sample (black data points) and a simulated distribution of the parameter obtained from the KDE (magenta cross-striped) normalised to 750 clouds.

As the correlation matrix in Tab. 5.2 shows, the strongest correlations are between the semi-major and semi-minor axis of the cloud ellipse and $M_{\mathrm{MC}}/d^2_{\mathrm{MC}}$. These correlations are illustrated in Fig. 5.6, which shows the dependence of the semi-major and minor axes of the cloud ellipses on $M_{\mathrm{MC}}/d^2_{\mathrm{MC}}$. This dependency is expected from the mass-radius dependency of the clouds as observed in Roman-Duval et al. (2010).
The blue squares in Fig. 5.6 represent the mean of the individual distributions and the errors are the standard deviation derived from the distributions in each $M_{\mathrm{MC}}/d^2_{\mathrm{MC}}$ bin divided by the square-root of the number of clouds within each bin. The grey-shaded band represents the mean semi-major, respectively semi-minor axis of the whole cloud sample of the Galactic Ring Survey. The mean semi-major, respectively semi-minor axis, increases with larger $M_{\mathrm{MC}}/d^2_{\mathrm{MC}}$. These correlations exist because the cloud mass depends on the radio intensity within the defined cloud region and, except for empty sky regions, the intensity increases with area. The semi-major and minor axes for the simulated molecular clouds are sampled as random variables using two-dimensional histograms for the corresponding $M_{\mathrm{MC}}/d^2_{\mathrm{MC}}$ bins a shown in Fig. 5.7.

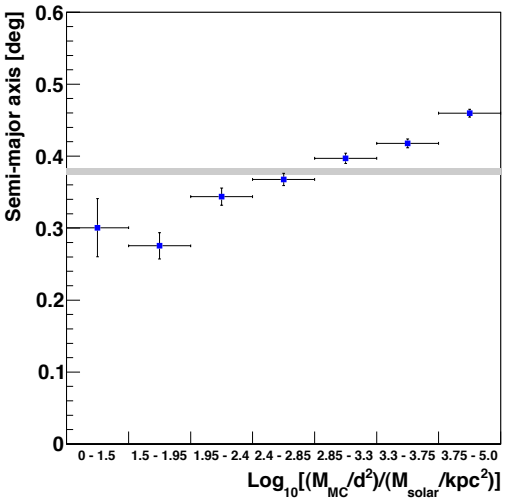


(a) Dependency of the semi-major axis of the cloud ellipses on $M_{\mathrm{MC}}/d^2_{\mathrm{MC}}$.

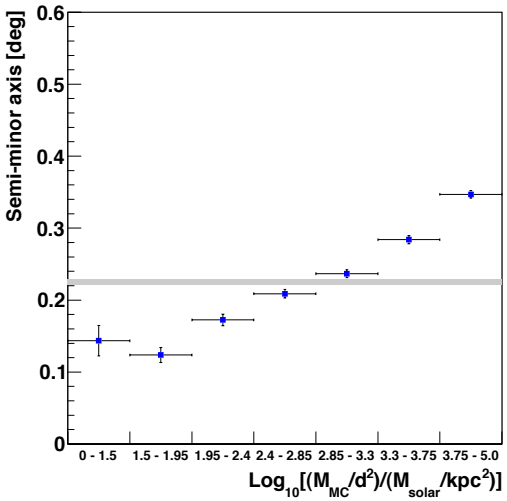


(b) Dependency of the semi-minor axis of the cloud ellipses on $M_{\mathrm{MC}}/d^2_{\mathrm{MC}}$.

**Figure 5.6:** Dependencies of the semi-major and minor axis of the cloud ellipses on $M_{\mathrm{MC}}/d^2_{\mathrm{MC}}$.

The correlation coefficients for the simulated clouds are listed in Table 5.3. The ones for the Galactic Ring Survey sample from Tab. 5.2 are given in brackets for comparison. As discussed above, the position of the molecular cloud and the angle of the cloud ellipse are simulated independently, therefore, their correlation coefficients are 0. The correlations between $M_{\mathrm{MC}}/d^2_{\mathrm{MC}}$ and the cloud position in Galactic longitude as well as between $M_{\mathrm{MC}}/d^2_{\mathrm{MC}}$, the semi-major axis $A$ and semi-minor axis $B$ of the cloud ellipse are considered in the simulation and the correlation coefficients are in good agreement with the ones derived from the clouds of the Galactic Ring Survey.

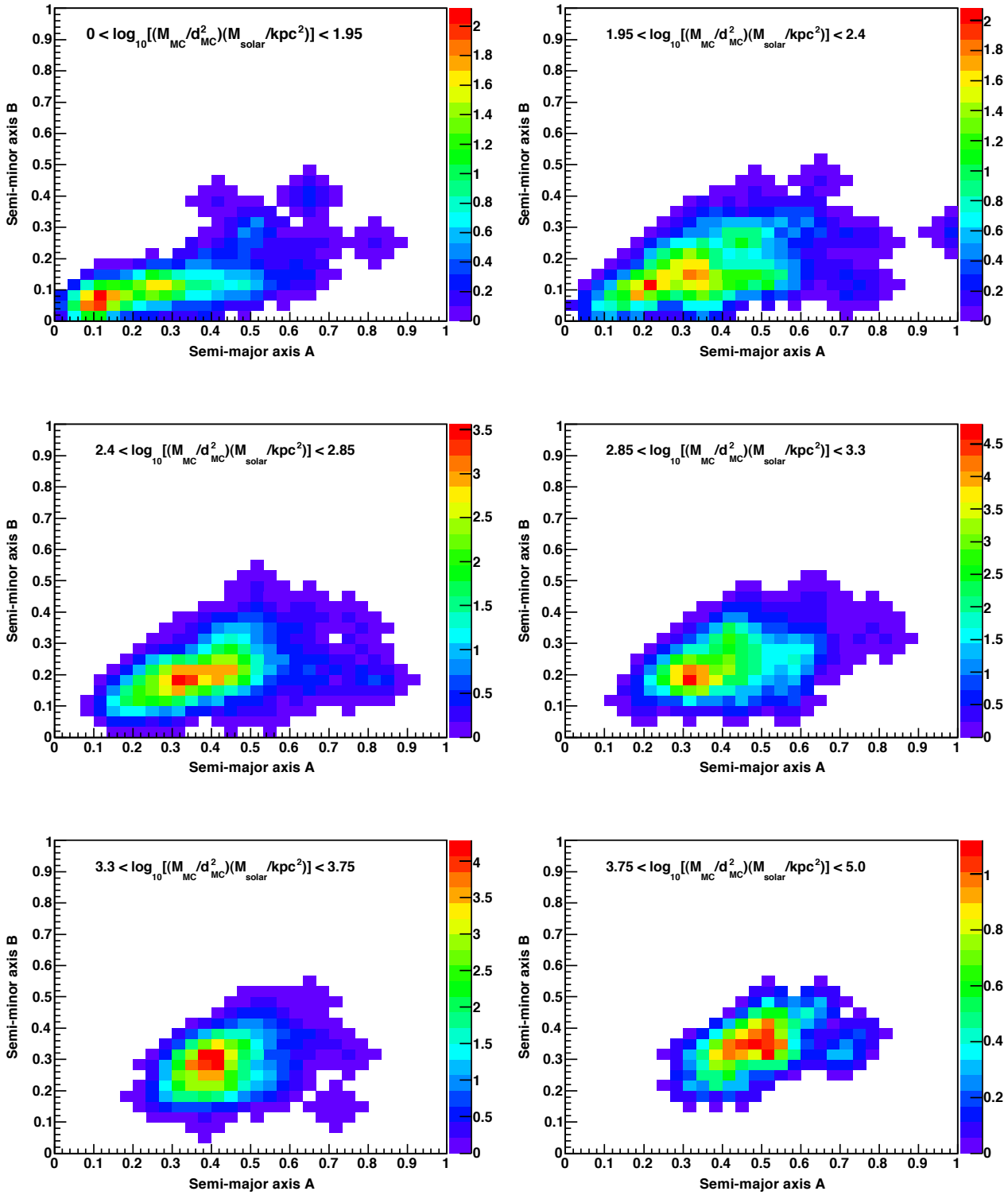


**Figure 5.7:** Semi-major and semi-minor axis of the ellipses for various $M_{\mathrm{MC}}/d_{\mathrm{MC}}^2$ bins.

**Table 5.3:** Correlation coefficients in % for the simulated molecular cloud sample and in brackets for the clouds of the Galactic Ring Survey. The semi-major axis is denoted by A, the semi-minor axis by B, respectively.

| | Longitude | Latitude | A | B | Angle | $M_{\mathrm{MC}}/d_{\mathrm{MC}}^2$ |
|---|---|---|---|---|---|---|
| Longitude | 100 (100) | 0 (−7) | −5 (−1) | −11 (−7) | 0 (5) | −20 (−14) |
| Latitude | 0 (−7) | 100 (100) | 0 (−1) | 0 (−8) | 0 (−6) | 0 (−9) |
| A | −5 (−1) | 0 (−1) | 100 (100) | 50 (56) | 0 (−1) | 26 (23) |
| B | −11 (−7) | 0 (−8) | 50 (56) | 100 (100) | 0 (5) | 53 (51) |
| Angle | 0 (5) | 0 (−6) | 0 (−1) | 0 (5) | 100 (100) | 0 (1) |
| $M_{\mathrm{MC}}/d_{\mathrm{MC}}^2$ | −20 (−14) | 0 (−9) | 26 (23) | 53 (51) | 0 (1) | 100 (100) |

The molecular cloud populations are simulated to estimate the level of random coincidences for the results in Fig. 5.2. A sample of $10^6$ molecular clouds was generated and the same coincidence criterion as defined in Section 5.2 was applied to those clouds. The fraction of spatially coincident clouds dependent on $M_{\mathrm{MC}}/d_{\mathrm{MC}}^2$ derived for the simulated molecular cloud sample and the sample of the clouds of the Galactic Ring Survey is shown in Fig. 5.8. The results for the clouds of the Galactic Ring Survey are the same as in Fig. 5.2. The results for the simulated cloud sample are illustrated in magenta in Fig. 5.8. The simulated cloud sample shows also a dependency of the fraction of spatially coincident clouds on $M_{\mathrm{MC}}/d_{\mathrm{MC}}^2$ as expected by the coincidence criterion, but the increase is not as strong as for the molecular clouds of the Galactic Ring Survey. The rather flat level for values $\log_{10}[(M_{\mathrm{MC}}/d_{\mathrm{MC}}^2)/(\mathrm{M}_\odot/\mathrm{kpc}^2)] < 2$ arises from the fact, that the semi-major and minor axis are generated from the same two-dimensional histogram as shown in Fig. 5.7 as the statistic in this bin is not sufficient enough to further divide the sample. The molecular clouds with $\log_{10}[(M_{\mathrm{MC}}/d_{\mathrm{MC}}^2)/(\mathrm{M}_\odot/\mathrm{kpc}^2)] < 2$ are below the completeness limit of the Galactic Ring Survey as discussed in Section 5.1. However, this should not influence the results here, as the simulated distribution of $M_{\mathrm{MC}}/d_{\mathrm{MC}}^2$ is generated from the observed one and, therefore, the fraction of clouds spatially coincident from the Galactic Ring Survey sample and the simulated clouds for the estimation of random coincidences are biased in the same way. In general, there is a good agreement between the results derived for the Galactic Ring Survey clouds and for the simulated molecular clouds, except for the bin $3.5 < \log_{10}[(M_{\mathrm{MC}}/d_{\mathrm{MC}}^2)/(\mathrm{M}_\odot/\mathrm{kpc}^2)] < 4$. The results derived with significance sky maps generated with correlation radii of 0.3° and 0.4° (Carrigan et al., 2013) in Fig. 5.9 and 5.10 show the same trend. Significance maps generated with different correlations radii are tested, because molecular clouds are extended objects with different sizes. The fraction of spatially coincident clouds, both for the Galactic Ring Survey sample and the simulated sample, is in general slightly higher for a correlation radius of 0.3° and 0.4° than for a correlation radius of 0.2° as the area on the significance map above the threshold of $7.5\,\sigma$ is larger. These results are discussed and interpreted in the following section.

## 5.4 Interpretation

The spatial coincidence of molecular clouds of the Galactic Ring Survey with $\gamma$-ray emission in the H.E.S.S. Galactic Plane Survey was tested in Section 5.2. This analysis resulted in 294 molecular clouds fulfilling the coincidence criterion for a $\gamma$-ray significance map generated

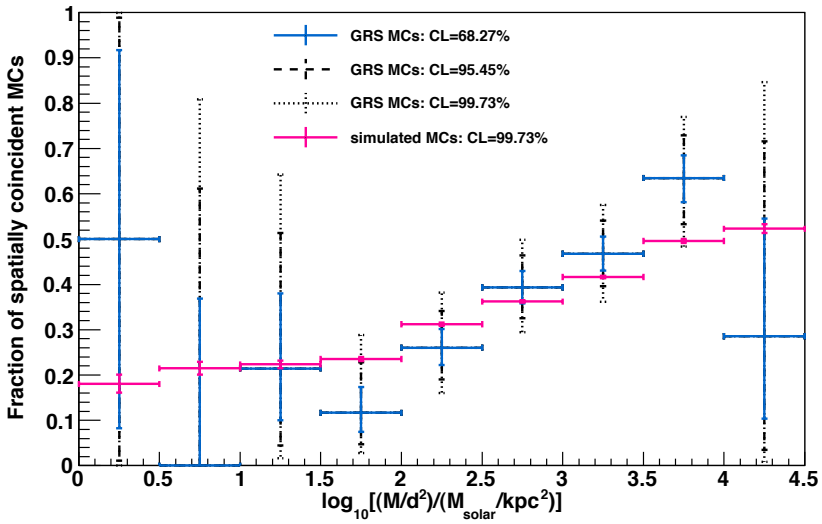


**Figure 5.8:** Fraction of molecular clouds (MCs) from the Galactic Ring Survey (GRS) spatially coincident with $\gamma$-ray emission in the H.E.S.S. Galactic Plane Survey denoted by the blue and black points. The level of random coincidences derived from $10^6$ simulated molecular clouds is illustrated in magenta. A threshold of $7.5\,\sigma$ was applied to a significance map with a correlation radius of 0.2°.

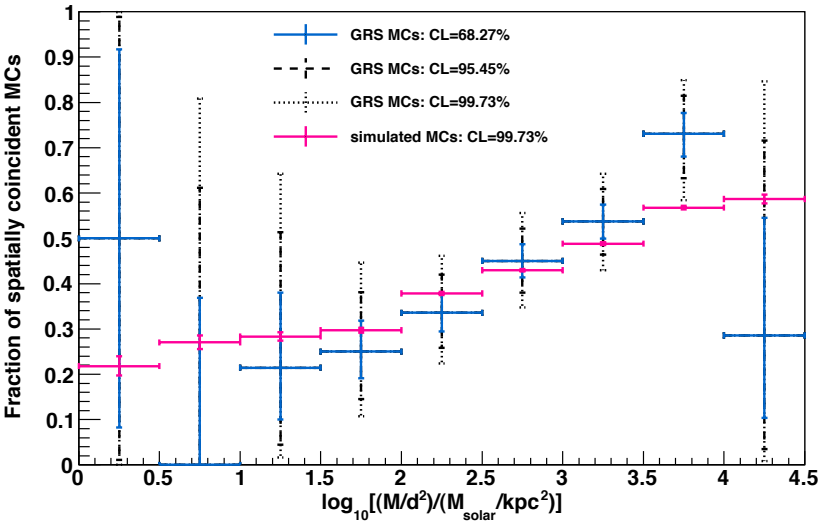


**Figure 5.9:** Fraction of molecular clouds (MCs) from the Galactic Ring Survey (GRS) spatially coincident with $\gamma$-ray emission in the H.E.S.S. Galactic Plane Survey denoted by the blue and black points. The level of random coincidences derived from $10^6$ simulated molecular clouds is illustrated in magenta. A threshold of $7.5\,\sigma$ was applied to a significance map with a correlation radius of 0.3°.

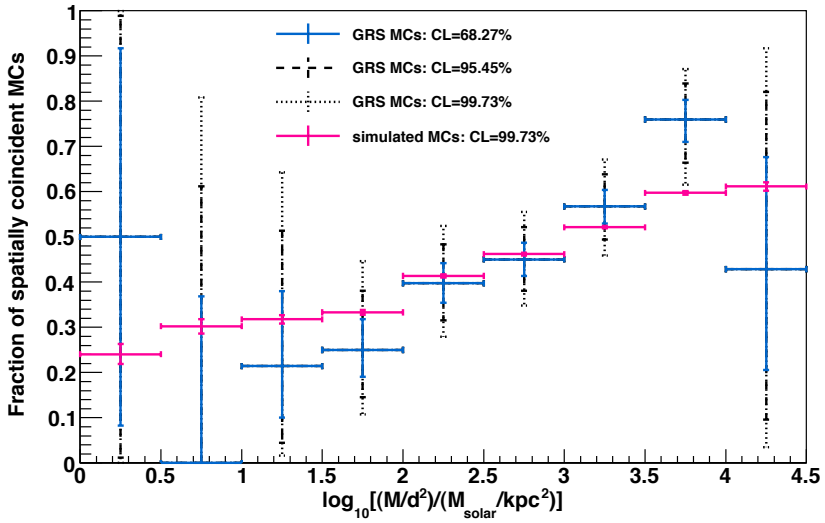


**Figure 5.10:** Fraction of molecular clouds (MCs) from the Galactic Ring Survey (GRS) spatially coincident with $\gamma$-ray emission in the H.E.S.S. Galactic Plane Survey denoted by the blue and black points. The level of random coincidences derived from $10^6$ simulated molecular clouds is illustrated in magenta. A threshold of $7.5\,\sigma$ was applied to a significance map with a correlation radius of 0.4°.

with a correlation radius of 0.2°. The fraction of molecular clouds not correlated with the $\gamma$-ray emission but spatially coincident with it by chance was estimated in Section 5.3 for $10^6$ simulated molecular clouds. These results are illustrated in Fig. 5.8, 5.9 and 5.10 for different values of $M_{\mathrm{MC}}/d^2_{\mathrm{MC}}$ since the expected $\gamma$-ray flux from molecular clouds is proportional to $M_{\mathrm{MC}}/d^2_{\mathrm{MC}}$.
In general, there is a good agreement for the results derived with the clouds of the Galactic Ring Survey and the estimated level of random coincidences in Fig. 5.8, 5.9 and 5.10, except for the bin with $3.5 < \log_{10}[(M_{\mathrm{MC}}/d^2_{\mathrm{MC}})/(\mathrm{M}_\odot/\mathrm{kpc}^2)] < 4$. The higher fraction of spatially coincident clouds for $3.5 < \log_{10}[(M_{\mathrm{MC}}/d^2_{\mathrm{MC}})/(\mathrm{M}_\odot/\mathrm{kpc}^2)] < 4$ arises for each tested correlation radius. In the following paragraphs, it is discussed whether this results can be interpreted as hint for a connection between molecular clouds with $3.5 < \log_{10}[(M_{\mathrm{MC}}/d^2_{\mathrm{MC}})/(\mathrm{M}_\odot/\mathrm{kpc}^2)] < 4$ of the Galactic Ring Survey and the $\gamma$-ray emission in the H.E.S.S. Galactic Plane Survey or if it arises through the analysis method used here.

The coincidence criterion depends on the size of the cloud which is correlated with the mass of the cloud. Therefore, an increasing fraction of spatially coincident clouds with larger $M_{\mathrm{MC}}/d^2_{\mathrm{MC}}$ is expected for the random coincidences. The dependency of the fraction of spatially coincident clouds of the Galactic Ring Survey on $M_{\mathrm{MC}}/d^2_{\mathrm{MC}}$ seems stronger than for the simulated molecular clouds. One could speculate that this different behaviour is caused by differences in the dependencies of the semi-major and minor axes of the clouds on $M_{\mathrm{MC}}/d^2_{\mathrm{MC}}$ for the clouds of the Galactic Ring Survey and the simulated cloud sample. The product of the semi-major axis $A$ and semi-minor axis $B$ is shown in dependence of $M_{\mathrm{MC}}/d^2_{\mathrm{MC}}$ for the clouds of the Galactic Ring Survey with black data points and for the simulated ones in magenta. The data points represent the mean of the individual distributions of $A \cdot B$ for a certrain range in $M_{\mathrm{MC}}/d^2_{\mathrm{MC}}$ and the errors are the standard deviations derived from the individual distributions divided by the square-root of the number of clouds in this $M_{\mathrm{MC}}/d^2_{\mathrm{MC}}$ bin. As shown in Fig. 5.11, the dependence of $A \cdot B$ on $M_{\mathrm{MC}}/d^2_{\mathrm{MC}}$ is the same for the molecular clouds of the Galactic Ring Survey and the simulated molecular clouds. Therefore, the effect

observed in Fig. 5.8 stems not from differences in the derived distributions for the semi-minor and major axis for the clouds of the Galactic Ring Survey and the $10^6$ simulated ones.

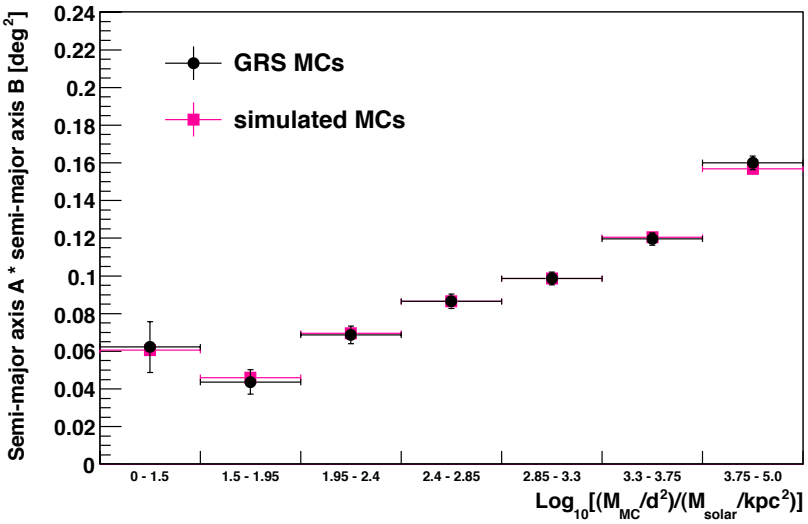


**Figure 5.11:** Dependency of the product of the semi-major axis A and semi-minor axis B on $M_{\mathrm{MC}}/d^2_{\mathrm{MC}}$. The black data points represent the molecular clouds (MCs) of the Galactic Ring Survey (GRS) and the magenta points the $10^6$ simulated molecular clouds.

The only dependencies on $M_{\mathrm{MC}}/d^2_{\mathrm{MC}}$ considered for the simulation of the molecular cloud populations are the correlation of the semi-major and semi-minor axis of the cloud ellipses with $M_{\mathrm{MC}}/d^2_{\mathrm{MC}}$ and the dependence of $M_{\mathrm{MC}}/d^2_{\mathrm{MC}}$ on the Galactic Longitude. Correlations smaller than 10 % are neglected. This could affect indeed the dependency of the fraction of spatially coincident molecular clouds on $M_{\mathrm{MC}}/d^2_{\mathrm{MC}}$. However, the cloud sample of the Galactic Ring Survey comprises only 750 clouds and it is, therefore, not possible to divide this sample into too many subsamples to consider each correlation of the cloud parameters in the simulation.

An analysis with an increased threshold is carried out to test the reliability of the level of random coincidences derived from simulated molecular cloud populations. Figure 5.12 shows the results derived with a higher threshold of $20\,\sigma$ to test the spatial coincidence with strong $\gamma$-ray sources on a significance map with a correlation radius of 0.2°. There are only two H.E.S.S. sources in the region covered by the Galactic Ring Survey with that high significances on the skymap generated for a correlation radius of 0.2° (Carrigan et al., 2013): the TeV sources HESS J1825−137, identified as pulsar wind nebula (Aharonian et al., 2005b), and HESS J1837−069, classified according to the catalogue of TeV sources, TeVCat, as unidentified but with a pulsar wind nebula as potential counter part. Both sources are not correlated with molecular clouds and the results in Fig. 5.12 confirm that the fraction of molecular clouds from the Galactic Ring Survey spatially coincident with this strong $\gamma$-ray emission are only random coincidences.
This strengthens the conclusion, that indeed the larger fraction of clouds spatially coincident with $\gamma$-ray emission in Fig. 5.8, 5.9 and 5.10 does not arise due to severe problems with the simulated molecular cloud sample. Therefore, the larger fraction of clouds spatially coincident with $\gamma$-ray emission ($> 7.5\,\sigma$) in the bin $3.5 < \log_{10}[(M_{\mathrm{MC}}/d^2_{\mathrm{MC}})/(\mathrm{M}_\odot/\mathrm{kpc}^2)] < 4$ illustrated in Fig. 5.8, 5.9 and 5.10 can be interpreted as a hint for a relation between the

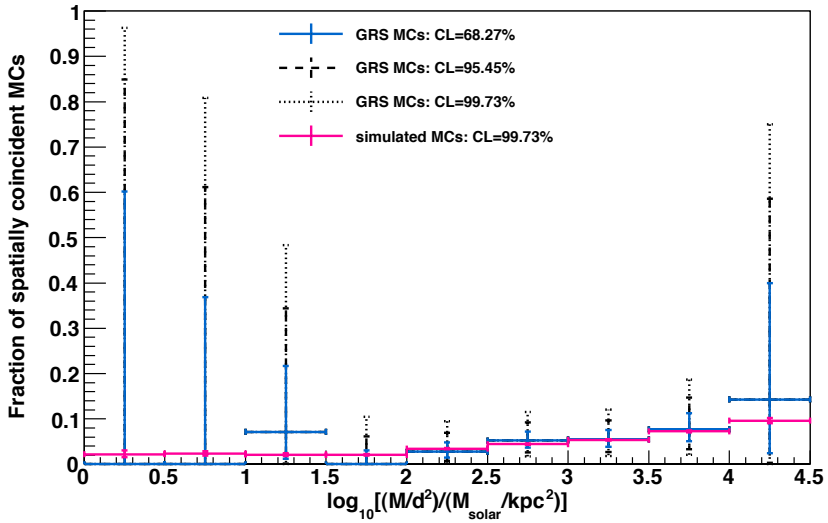


**Figure 5.12:** Fraction of molecular clouds (MCs) from the Galactic Ring Survey (GRS) spatially coincident with strong $\gamma$-ray emission in the H.E.S.S. Galactic Plane Survey denoted by the blue and black points. The level of random coincidences derived from $10^6$ simulated molecular clouds is illustrated in magenta. A threshold of $20\,\sigma$ was applied to a $\gamma$-ray significance map with a correlation radius of 0.2°.

molecular clouds of the Galactic Ring Survey and the $\gamma$-ray emission in the H.E.S.S. Galactic Plane Survey.

**Table 5.4:** Number of clouds of the Galactic Ring Survey with $3.5 < \log_{10}[(M_{\mathrm{MC}}/d^2_{\mathrm{MC}})/(\mathrm{M}_\odot/\mathrm{kpc}^2)] < 4$ spatially coincident with $\gamma$-ray emission in the H.E.S.S. Galactic Plane Survey on $\gamma$-ray significance sky maps generated by Carrigan et al. (2013) with correlation radii of 0.2°, 0.3° and 0.4°. A treshold of $7.5\,\sigma$ was applied. The probabilities $P$, thath the number $N_{\mathrm{MC}}$ arises due to random coincidences of a level $f_{\mathrm{RC}}$ are calculated according to Eq. 5.1.

| Corr. radius [°] | $N_{\mathrm{MC}}$ | $N_{\mathrm{tot}}$ | $f$ | $f_{\mathrm{RC}}$ | $P(\geq N_{\mathrm{MC}}; f_{\mathrm{CC}}, N_{\mathrm{tot}})$ |
|---|---|---|---|---|---|
| 0.2 | 66 | 104 | 0.63 | 0.50 | $3.9 \cdot 10^{-3}$ |
| 0.3 | 76 | 104 | 0.73 | 0.57 | $5.1 \cdot 10^{-4}$ |
| 0.4 | 79 | 104 | 0.76 | 0.60 | $4.5 \cdot 10^{-4}$ |

Table 5.4 summarises the number $N_{\mathrm{MC}}$ of spatially coincident clouds and the number $N_{\mathrm{tot}}$ of all clouds with $3.5 < \log_{10}[(M_{\mathrm{MC}}/d^2_{\mathrm{MC}})/(\mathrm{M}_\odot/\mathrm{kpc}^2)] < 4$ for the test on $\gamma$-ray significance maps generated with correlation radii of 0.2°, 0.3° and 0.4° (Carrigan et al., 2013) with an applied threshold of $7.5\,\sigma$. The ratio of $N_{\mathrm{MC}}$ and $N_{\mathrm{tot}}$ is denoted by $f$ and the level of random coincidences, derived from the simulated molecular cloud sample, by $f_{\mathrm{RC}}$. The probability of $N_{\mathrm{MC}}$ or more clouds from a sample of $N_{\mathrm{tot}}$ to be spatially coincident with the $\gamma$-ray emission due to random coincidences can be calculated following Eq. 5.1 as $P(\geq N_{\mathrm{MC}}; f_{\mathrm{RC}}, N_{\mathrm{tot}})$ and is also listed in Tab. 5.4. It is interesting to note that the probability to observe that fraction of spatially coincident clouds due to random coincidences has the lowest value of $4.5 \cdot 10^{-4}$ for the test with a significance map generated with a correlation radius of 0.4° since the distribution of $\sqrt{A \cdot B}$ has a mean value of 0.38° with a standard deviation of 0.07 for clouds with $3.5 < \log_{10}[(M_{\mathrm{MC}}/d^2_{\mathrm{MC}})/(\mathrm{M}_\odot/\mathrm{kpc}^2)] < 4$. However, the larger fractions of spatially coincident clouds derived here are not significant and can only be interpreted as a hint for a relation between molecular clouds of the Galactic Ring Survey with

$3.5 < \log_{10}[(M_{\mathrm{MC}}/d_{\mathrm{MC}}^2)/(\mathrm{M}_\odot/\mathrm{kpc}^2)] < 4$ and extended $\gamma$-ray emission in the H.E.S.S. Galactic Plane Survey.

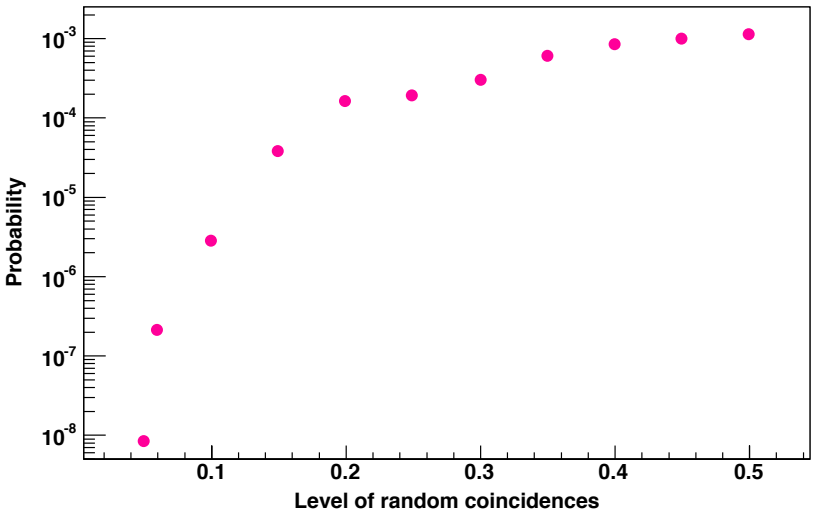


**Figure 5.13:** The probablility that an enhancement of 15 % of 104 clouds with $3.5 < \log_{10}[(M_{\mathrm{MC}}/d_{\mathrm{MC}}^2)/(\mathrm{M}_\odot/\mathrm{kpc}^2)] < 4$ arises due to random coincidences in depencence on the level of random coincidences.

The values in Tab. 5.4 indicate that maximal a fraction of 15 % from the 104 clouds with $3.5 < \log_{10}[(M_{\mathrm{MC}}/d_{\mathrm{MC}}^2)/(\mathrm{M}_\odot/\mathrm{kpc}^2)] < 4$ could be physically related to the $\gamma$-ray emission. As discussed above, the probability derived here that the observed fraction of spatially coincident clouds arises due to random coincidences is too large to claim a significant result. This is mainly caused by the high level of random coincidences. The fraction of random coincidences from Tab. 5.4 ranges from 0.5 to 0.6. To obtain a significant result it would be necessary to decrease the fraction of random coincidences. The probability that an enhancement of 15 % of a sample of 104 clouds regarding to a certain level of random coincidences arises due to random coincidences is shown by the magenta points in Fig. 5.13. The numbers of spatially coincident clouds $N_{\mathrm{MC}}$ for each level of random coincidences were rounded up, respectively off to whole numbers for the calculation of the probabilities.
To achieve a significant result it would be necessary to reduce the level of random coincidences to less than 10 % as shown in Fig. 5.13. However, this low level of random coincidences is not possible to achieve with the loose spatial coincidence criterion as done here using the significance sky maps and the peak significance within the elliptic cloud area. With the forthcoming source catalogue (H.E.S.S. Collaboration et al., 2014c) of the H.E.S.S. Galactic Plane Survey it is possible to define a different criterion for spatial coincidence which considers additional information, such as a certain containment radius of the H.E.S.S. sources. However, it will remain challenging to achieve a level of random coincidences of 10 % or less with large extended objects such as molecular clouds.

Interpreting the results derived above as hint, one could speculate about the origin of the increased fraction of spatially coincident clouds. Scenarios for $\gamma$-ray emission from molecular clouds are described in Chapter 3. The simplest scenario arises from passive molecular clouds, i.e., clouds only embedded in the cosmic-ray sea. Estimating the $\gamma$-ray emission for the cloud sample of the Galactic Ring Survey according to Eq. 3.3 and comparing the integral flux value

with the flux sensitivity of the H.E.S.S. Galactic Plane Survey, which is about $3 \cdot 10^{-13}\,\mathrm{cm}^{-2}\,\mathrm{s}^{-1}$ for a correlation radius of 0.2° (see Section 6.1) leads to no individually detectable clouds. Since many molecular clouds are located at different distances but at the same line-of-sight, as shown in Fig. 5.1, the flux of all molecular clouds at the same line-of-sight is considered in Fig. 5.14. The flux of each cloud is normalised to the area of the cloud, summed up for all clouds at the same line-of-sight and represented by the colour scale in Fig. 5.14. Even the sum of the individual $\gamma$-ray fluxes of molecular clouds only embedded in the cosmic ray sea would not lead to a significant $\gamma$-ray emission detectable with H.E.S.S.

Higher $\gamma$-ray fluxes than the ones from passive molecular clouds, are expected from molecular clouds near potential cosmic-ray sources such as supernova remnants. According to TeVCat, two identified supernova remnant/molecular cloud associations, HESS J1923+141 and HESS J1911+090, are located in the region covered by the Galactic Ring Survey as well as three aditional sources, HESS J1858+020, HESS J1852-000 and HESS J1834-087, classified as unidentified sources with a supernova remnant/molecular cloud association as potential counter part. The statistical method used in this chapter, however, does not allow to determine which of the molecular clouds with $3.5 < \log_{10}[(M_{\mathrm{MC}}/d_{\mathrm{MC}}^2)/(\mathrm{M}_\odot/\mathrm{kpc}^2)] < 4$ are related to $\gamma$-ray emission and which are only spatially coincident by chance. Considering the level of random coincidences, maximal 15% of the molecular clouds of the Galactic Ring Survey with $3.5 < \log_{10}[(M_{\mathrm{MC}}/d_{\mathrm{MC}}^2)/(\mathrm{M}_\odot/\mathrm{kpc}^2)] < 4$ are related to $\gamma$-ray emission in the H.E.S.S. Galactic Plane Survey. It is, yet, not possible to establish a relation between the number of clouds related to $\gamma$-ray emission and the number of H.E.S.S. sources identified as supernova remnant/molecular cloud association. This is the case, because more than one cloud could be physically related to a TeV $\gamma$-ray source and the exact assignment of the molecular emission features, identified in the Galactic Ring Survey as clouds, to the $\gamma$-ray sources is not determined.

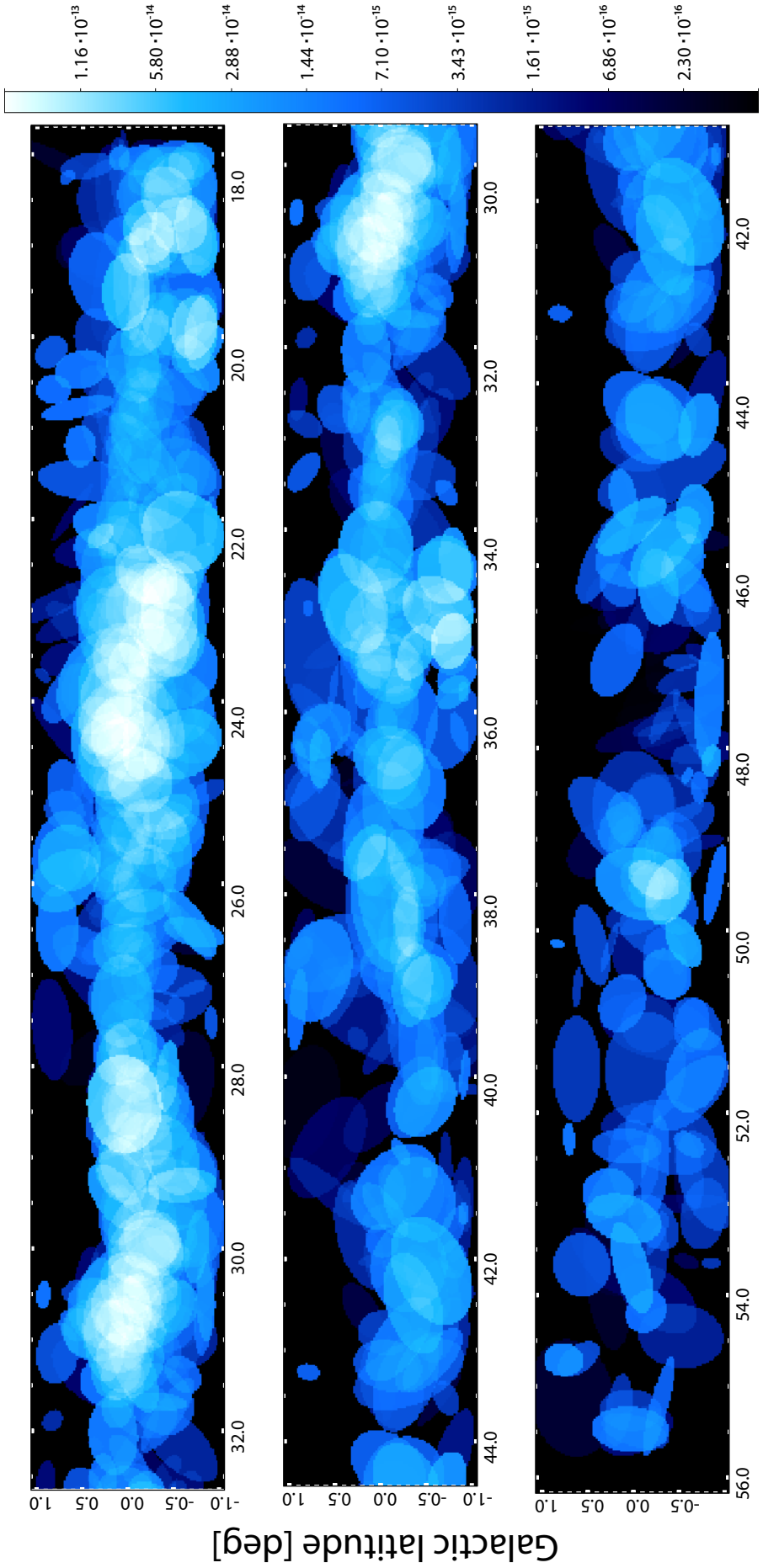


**Figure 5.14:** Sky map with the integral fluxes above 1 TeV in units of [$cm^{-2}$ $s^{-2}$ $deg^{-2}$] for the clouds of the Galactic Ring Survey assuming those are only embedded in the cosmic-ray sea. The ellipses are representing the molecular clouds. The flux values are normalised each for the area of the corresponding cloud ellipse.

## 5.5 Conclusion

The analysis presented in this chapter searched for a connection between the molecular clouds of Galactic Ring Survey and $\gamma$-ray emission in the H.E.S.S. Galactic Plane Survey. A molecular cloud is defined as spatially coincident if the $\gamma$-ray peak significance within the elliptical representation of the cloud is larger than the defined threshold of $7.5\,\sigma$. The application of the coincidence criterion on the cloud sample of the Galactic Ring Survey and on the significance map of the H.E.S.S. Galactic Plane Survey (Carrigan et al., 2013) generated with a correlation radius of 0.2° resulted in 294 of the 750 molecular clouds to be spatially coincident.
A large part of these clouds are not related to any $\gamma$-ray emission but are spatially coincident with it by chance. The level of random coincidences was estimated in Section 5.3 with simulated populations of molecular clouds and illustrated in dependence of $M_{\mathrm{MC}}/d_{\mathrm{MC}}^2$, as $\gamma$-ray emission from molecular clouds is proportional to the mass of the cloud $M_{\mathrm{MC}}$ divided by the distance $d_{\mathrm{MC}}$ of the cloud squared. For most bins in $M_{\mathrm{MC}}/d_{\mathrm{MC}}^2$ there is a good agreement between the fraction of clouds from the Galactic Ring Survey beeing spatially coincident and the level of random coincidences estimated using $10^6$ simulated molecular clouds, except for clouds with $3.5 < \log_{10}[(M_{\mathrm{MC}}/d_{\mathrm{MC}}^2)/(\mathrm{M}_\odot/\mathrm{kpc}^2)] < 4$. There are more clouds with these properties fulfilling the coincidence criterion than expected by random coincidences. This trend arises also for tests with $\gamma$-ray significance sky maps generated with correlation radii of 0.3° and 0.4° (Carrigan et al., 2013). The probability of the larger fraction of spatially coincident clouds for the three different significance maps to originate due to random coincidences is about $3.9 \cdot 10^{-3}$, $5.1 \cdot 10^{-4}$ and $4.5 \cdot 10^{-4}$ for the correlation radii of the significance map of 0.2°, 0.3° and 0.4°, respectively. However, the level of random coincidences might be slightly underestimated as only the correlation of properties of the molecular clouds of the Galactic Ring Survey which have a larger correlation coefficient than 10 % are considered for the simulation of the molecular cloud populations. Tests of spatial coincidence with strong $\gamma$-ray sources associated with pulsar wind nebula show a good agreement between the results derived for the molecular clouds of the Galactic Ring Survey and the estimated level of random coincidences. The analysis presented here gives a hint that 15 % of the 104 molecular clouds with $3.5 < \log_{10}[(M_{\mathrm{MC}}/d_{\mathrm{MC}}^2)/(\mathrm{M}_\odot/\mathrm{kpc}^2)] < 4$ might be related to $\gamma$-ray emission. However, to achieve a significant result it would be necessary to reduce the level of random coincidences to be less than 10 %.
Hence, the larger fraction of spatially coincident clouds for molecular clouds with $3.5 < \log_{10}[(M_{\mathrm{MC}}/d_{\mathrm{MC}}^2)/(\mathrm{M}_\odot/\mathrm{kpc}^2)] < 4$ can merely interpreted as a hint for a connection between these clouds and the $\gamma$-ray emission of the H.E.S.S. Galactic Plane Survey. The statistical method applied in this chapter, however, can not determine exactly which clouds are related to $\gamma$-ray emission and which are only coincident with it by chance. The calculation of the integral $\gamma$-ray fluxes from molecular clouds embedded in the cosmic ray sea, even considering all clouds in the same line-of-sight, showed that $\gamma$-ray emission from passive molecular clouds are not detectable with the sensitivity of the H.E.S.S. Galactic Plane Survey. Therefore, the relation between molecular clouds of the Galactic Ring Survey with $3.5 < \log_{10}[(M_{\mathrm{MC}}/d_{\mathrm{MC}}^2)/(\mathrm{M}_\odot/\mathrm{kpc}^2)] < 4$ and $\gamma$-ray emission in the H.E.S.S. Galactic Plane Survey hints towards molecular clouds near potential cosmic-ray sources, such as supernova remnants.

CHAPTER 6

# Study of gamma-ray emitting molecular clouds in the vicinity of supernova remnants

The study of spatial coincidence of molecular clouds with observed $\gamma$-ray emission from the H.E.S.S. Galactic Plane Scan, presented in Chapter 5, revealed a slightly larger fraction of molecular clouds spatially coincident with the TeV emission than expected from random coincidences for molecular clouds with $3.5 < \log_{10}[(M_{\mathrm{MC}}/d^2_{\mathrm{MC}})/(\mathrm{M}_\odot/\mathrm{kpc}^2)] < 4$. This cannot be explained by the $\gamma$-ray emission of passive molecular clouds, but might be interpreted as a hint of $\gamma$-ray emitting molecular clouds in the vicinity of accelerators. As discussed in Chapter 2, supernova remnants are prime candidates as sources of cosmic rays and thus, this chapter focuses on molecular clouds near supernova remnants.

First, in Section 6.1, the parameter space for molecular clouds near supernova remnants detectable at the sensitivity level of the H.E.S.S. Galactic Plane Survey is explored, specifically with regard to the normalisation of the diffusion coefficient $D_{10}$ at 10 GeV and the distance between the supernova remnant and molecular cloud. In Section 6.2 a search for regions populated with potentially detectable molecular clouds is presented, using molecular clouds from the Galactic Ring Survey and selected supernova remnants from the catalogue of Ferrand & Safi-Harb (2012). Section 6.3 presents constraints on the diffusion coefficient derived with simulated populations of supernova remnants provided by Hahn (2014) and the number of TeV sources identified as supernova remnant/molecular cloud associations. Apart from that, the prospects with the forthcoming experiment CTA observatory are discussed.

Parts of the discussion on the parameter space of molecular clouds near supernova remnants, as well as the introduction of the search strategy and parts of the discussion on the W44 region, were published first in Häffner et al. (2013).

## 6.1 Parameter space for molecular clouds detectable with H.E.S.S.

There are different theoretical models to estimate the expected $\gamma$-ray emission from molecular clouds that are illuminated by escaped particles from a nearby supernova remnant. These models range from simple approaches to complex models using numerical simulations. The search in this work for detectable $\gamma$-ray emitting molecular clouds in the region of the H.E.S.S. Galactic Plane Survey uses the model by Gabici et al. (2009), introduced in Section 3.4. More elaborated models that rely on detailed information on the individual supernova remnant environments, e.g., densities and magnetic field orientations, are not suited for a general search strategy as discussed in this work.
An examplarily scenario of a molecular cloud near a supernova remnant is discussed in the following to show which parameter space, especially the range of the diffusion coefficient and distance $D_{\text{SNR-MC}}$ between molecular cloud and supernova remnant, can be explored within the data of the H.E.S.S. Galactic Plane Survey. The cloud has a mass of $4 \cdot 10^4\,\mathrm{M}_\odot$ and is located at a distance of 2 kpc to Earth. These values resemble the cloud properties as in the $\gamma$-ray emission scenario in the W28 region (Aharonian et al., 2008b). A Sedov time of 200 yr and an efficiency of 30 % for the conversion of the supernova explosion energy of $10^{51}$ erg into acceleration of particles are assumed here. Figure 6.1(a) shows the integral $\gamma$-ray fluxes above 1 TeV, $I(>1\,\text{TeV})$, of this molecular cloud with a distance of 50 pc to a remnant as a function of the normalisation of the diffusion coefficient $D_{10}$ at 10 GeV for three different ages of the supernova remant. The energy dependence of the diffusion coefficient is considered to be of the form $D(E) = D_{10} \cdot \left(\frac{E}{10\,\text{GeV}}\right)^s$, with $s = 0.5$. The integral fluxes above 1 TeV lie between $10^{-14}\,\mathrm{cm}^{-2}\,\mathrm{s}^{-1}$ and $10^{-11}\,\mathrm{cm}^{-2}\,\mathrm{s}^{-1}$ depending on the age of the supernova remnant and the diffusion coefficient.
Current imaging Cherenkov telescope systems reach integral flux sensitivities above 1 TeV in the order of $1-2\,\%$ Crab units (C.U.)[1]. The integral flux sensitivity of the H.E.S.S. Galactic Plane Survey (Carrigan et al., 2013) for the region covered by the Galactic Ring Survey is shown in Fig. 6.2 for a correlation radius of 0.2°.
Comparison of the sensitivity of the H.E.S.S. Galactic Plane Survey with the derived TeV $\gamma$-ray fluxes for the examplary scenario in Fig. 6.1(a) shows that a wide range of diffusion coefficients and ages of the supernova remnant gives detectable $\gamma$-ray fluxes. The parameter space for detectable $\gamma$-rays supernova remnant/ molecular cloud associations depends on the diffusion coefficient, the age of the remnant and additionally on the seperation $D_{\text{SNR–MC}}$ between the remnant and the cloud as shown in Fig. 6.1(b). The hatched areas indicate the parameter space in $D_{\text{SNR–MC}}$ and $D_{10}$ which leads, for three different ages of the supernova remnant and the remaining parameters chosen as in the example above, to an integral $\gamma$-ray flux larger than $3 \cdot 10^{-13}\,\mathrm{cm}^{-2}\,\mathrm{s}^{-1}$. This value was picked since it is reached in the H.E.S.S. Galactic Plane Survey sensity for almost the whole region also covered by the Galactic Ring Survey between 18° and 56° Galactic longitude. Molecular clouds near young remnants are thus detectable in TeV $\gamma$-rays for a large range of diffusion coefficients and a distance smaller than 85 pc to the supernova remnant whereas for old remnants ambient clouds are detectable only for low diffusion coefficients of about $D_{10} \approx 10^{26}\,\mathrm{cm}^2\,\mathrm{s}^{-1}$. This can be understood intuitively as for high diffusion coefficients and large ages the particles are distributed within a larger volume and the particle density is lower.

[1] here: $1\,\text{C.U.} = I_{\text{Crab}}(>1\,\text{TeV}) = 2.26 \cdot 10^{-11}\,\mathrm{cm}^{-2}\,\mathrm{s}^{-1}$

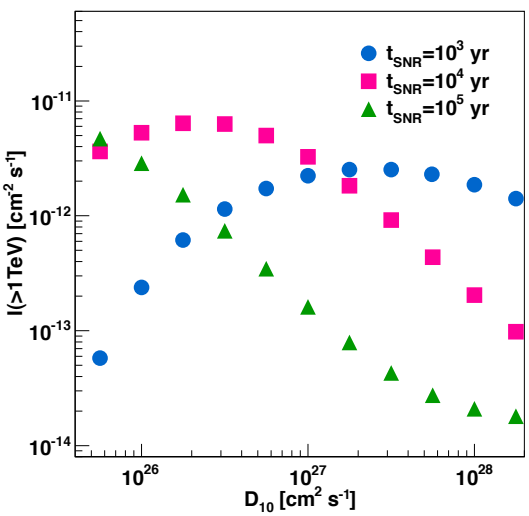


(a) Integral $\gamma$-ray fluxes above 1 TeV as a function of $D_{10}$ for three assumed ages of the supernova remnant and a distance of 50 pc between the remnant and the molecular cloud.

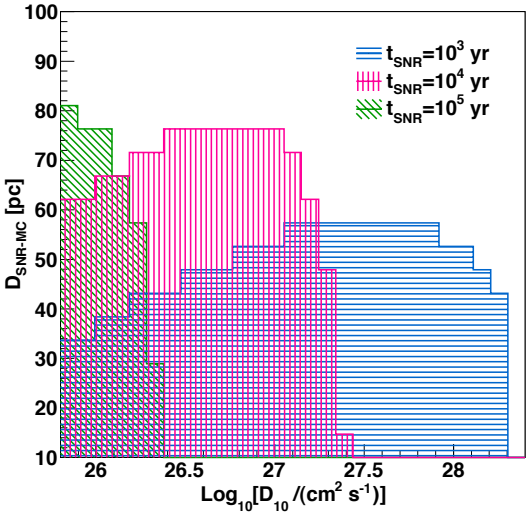


(b) The detectable ($I(>1\,\text{TeV}) > 3 \cdot 10^{-13}\,\text{cm}^{-2}\,\text{s}^{-1}$) parameter space for the diffusion coefficient and distance between the supernova remnant and the molecular cloud is shown exemplarily.

**Figure 6.1:** Integrated flux and detectable parameter space for a molecular cloud near a supernova remnant. The supernova remnant is situated near a molecular cloud with a mass of $4 \cdot 10^4\,M_\odot$ and a distance to Earth of 2 kpc.

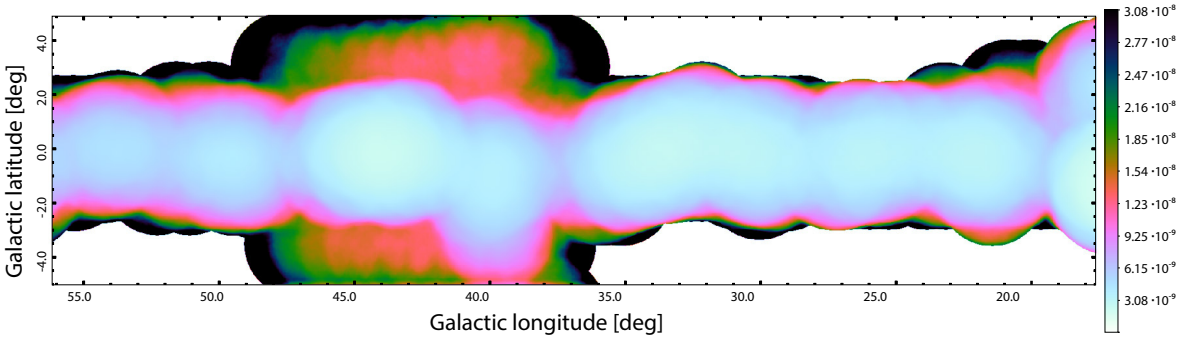


**Figure 6.2:** Integral sensitivity of the H.E.S.S. Galactic Plane Survey (Carrigan et al., 2013) above 1 TeV for a correlation radius of 0.2° given in $\text{m}^{-2}\,\text{s}^{-1}$. Only the region of the H.E.S.S. Galactic Plane Survey, that is also covered by the Galactic Ring Survey, is shown here.

## 6.2 Search for potentially detectable molecular clouds

This section presents a search for regions with potentially detectable $\gamma$-ray emitting molecular clouds within the area of the Galactic plane covered by the Galactic Ring Survey. Within this region, between 18° and 56° Galactic longitude, there are two identified supernova remnant/molecular cloud associations and three further sources classified as unidentified sources in the TeV energy band. Apart from these regions, there might be more supernova remnant/molecular cloud associations for which no TeV counterpart has been identified yet. The search strategy for regions populated with potentially detectable molecular clouds is introduced in Section 6.2.1 and the interpretation of the results derived in this search is given in Section 6.2.2. Two specific regions are individually discussed: the region around the supernova remnant W44 is examined in Section 6.2.3, and a closer look at the region of the supernova remnant 3C391 in the TeV band is presented in Chapter 7.

### 6.2.1 Search strategy

The search uses molecular clouds, supernova remants, the model of Gabici et al. (2009) for the calculation of the expected $\gamma$-ray fluxes, and the sensitivity of the H.E.S.S. Galactic Plane Survey. The input parameters of the theoretical model of Gabici et al. (2009) are the following:

- age $t_{\mathrm{SNR}}$ of the remnant;
- distance $D_{\mathrm{SNR-MC}}$ between the remnant and the molecular cloud;
- cloud mass $M_{\mathrm{MC}}$;
- distance of the cloud to Earth $D_{\mathrm{MC}}$;
- portion of energy of the supernova explosion, $\eta \cdot E_{SN}$, that was converted into the acceleration of cosmic rays ;
- normalisation of the diffusion coefficient $D_{10}$ at 10 GeV;
- energy dependence $s$ of the diffusion coefficient.

Although, not all of these parameters are well constrained, a general search for regions harbouring potentially detectable molecular clouds is possible with the strategy as described below.
The molecular cloud and supernova remnant sample, used in this search, is selected from public catalogues. The clouds from the Galactic Ring Survey are taken as molecular cloud sample. The cloud properties were discussed in detail in Section 5.1. The supernova remnants located in the region of the Galactic Ring Survey, for which age and distance estimates are available, are selected from the supernova remnant catalogue[2] of Ferrand & Safi-Harb (2012). The ages of the remnants range from 720 yr to $2 \cdot 10^5$ yr, their distances from 2.3 kpc to 19 kpc. The properties of the 22 supernova remants considered in this search are listed in Table 6.1. All supernova remnants are combined with all molecular clouds. For each supernova remant/molecular cloud pair the integral flux above 1 TeV is calculated and later compared to the sensitivity of the H.E.S.S. Galactic Plane Survey to estimate which clouds can be expected

[2] http://www.physics.umanitoba.ca/snr/SNRcat/

**Table 6.1:** Supernova remnants from the catalogue by Ferrand & Safi-Harb (2012) considered for the search.

| Remnant | Other names | Distance [kpc] | age [yr] |
|---|---|---|---|
| G015.9+00.2 | | 8.5 | 1 000 – 3 000 |
| G018.8+00.3 | Kes 67 | 4.0 – 19 | 100 000 |
| G021.5-00.9 | | 4.3 – 5.1 | 720 – 1 070 |
| G021.8-00.6 | Kes 69 | 5.2 – 5.5 | 4 400 – 5 000 |
| G023.3-00.3 | W41 | 3.9 – 4.5 | 60 000 – 200 000 |
| G027.4+00.0 | Kes 73 | 7.5 – 9.1 | 750 – 2 100 |
| G028.6-00.1 | AX J1843.8-0352 | 6 – 8.5 | $\leq$ 2 700 |
| G029.7-00.3 | Kes 75 | 6.3 – 10.6 | 900 – 7 000 |
| G031.9+00.0 | 3C391, Kes 77 | 7.2 – 8.6 | 3 700 – 4 400 |
| G032.8+00.0 | Kes 78 | 4.8 | 6 000 |
| G033.6+00.1 | Kes 79 | 7.1 | 3 000 – 15 000 |
| G034.7-00.4 | W44, 3C392 | 2.5 – 2.6 | 6 000 – 29 000 |
| G035.6-00.4 | | 3.2 – 4 | 2 300 |
| G038.7-01.4 | | 4 | 14 000 – 15 000 |
| G039.2-00.3 | 3C396 | 6.2 | 3 000 – 7 000 |
| G039.7-02.0 | W50 | 5.5 – 6.5 | 30 000 |
| G041.1-00.3 | 3C397 | 10.3 | 5 300 |
| G043.3-00.2 | W49B, 3C398 | 8 – 11 | 4 000 – 6 000 |
| G049.2-00.7 | W51C | 4.3 – 6 | 26 000 – 30 000 |
| G053.6-02.2 | 3C400.2 | 2.3 – 6.7 | 15 000 – 110 000 |
| G054.1+00.3 | | 5.6 – 7.2 | 2 500 – 3 300 |
| G054.4-00.3 | | 3.3 – 9 | 61 000 |

**Table 6.2:** Parameters and step sizes of the parameter scan for the calculation of $\gamma$-ray fluxes for each supernova remnant/molecular cloud pair.

| Parameter | Value | Steps |
|---|---|---|
| $D_{10}\,[\mathrm{cm^2\,s^{-1}}]$ | $[10^{26}\ldots\ 10^{28}]$ | $[10^{26}, 10^{27}, 10^{28}]$ |
| $s$ | 0.5 | fixed |
| $\eta \cdot E_{\mathrm{SN}}\,[\mathrm{erg}]$ | $0.3 \cdot 10^{51}$ | fixed |
| $t_{\mathrm{SNR}}$ | $t_{\mathrm{min}} - t_{\mathrm{max}}$ | 5 different ages |
| $d_{\mathrm{SNR}}$ | $d_{\mathrm{min}} - d_{\mathrm{max}}$ | 5 pc steps |
| $M_{\mathrm{MC}}$ | $M_{\mathrm{MC}} \pm \Delta M_{\mathrm{MC}}$ | 3 different masses |
| $d_{\mathrm{MC}}$ | $d_{\mathrm{MC}} \pm \Delta d_{\mathrm{MC}}$ | 5 pc steps |

to emit detectable $\gamma$-ray emission. To take into account the uncertainties of the different parameters in the TeV flux calculation a parameter scan was performed. The scan ranges and the step sizes are given in Table 6.2.
As mentioned above the local diffusion coefficient and its energy dependence in general are not known, just the average Galactic normalisation is determined and is in the order of $10^{28}\,\mathrm{cm^2\,s^{-1}}$ (Strong et al., 2007). Following the usual approach, e.g., (Pedaletti et al., 2013), the range between $10^{26}\,\mathrm{cm^2\,s^{-1}}$ and $10^{28}\,\mathrm{cm^2\,s^{-1}}$ for $D_{10}$ and a power law with index $s = 0.5$ for the energy dependence are assumed to be suitable values. The minimum and maximum values for the ages and distances of the supernova remnants are taken from Ferrand & Safi-Harb (2012). If no error or uncertainty are listed in the catalogue, the given value is used without adding any arbitary error. The range of the age of the supernova remnant is scanned with five steps. Considering the large uncertainty of $D_{10}$ this seems a good compromise.
The errors on the MC distances are estimated in Roman-Duval et al. (2009) to be of the order of $20\,\% - 30\,\%$, therefore, $\Delta d_{\mathrm{MC}} = 0.2 \cdot d_{\mathrm{MC}}$ is used as distance uncertainty. The distance between the supernova remnant and the molecular cloud is defined as the distance between the centre position of the remnant and the peak of highest emission of the cloud. The results do not change significantly if instead the position with the highest molecular emission is employed. The mean radius of the clouds is 24.1 pc (Rathborne et al., 2009), which is small compared to the errors on the distances of the remnants and clouds. The range of the distance of the supernova remnant is scanned in 5 pc steps as well as the distance of the molecular cloud. As shown in Fig. 6.1(b) the maximal allowed distance between the remnant and the cloud, for which our exemplarily supernova remnant/molcular cloud association emits detectable $\gamma$-ray emission is less than 100 pc, thus step sizes of 5 pc appear suitable. The errors on the cloud masses $\Delta M_{\mathrm{MC}}$ are given individually for each cloud in Roman-Duval et al. (2010) and vary from about 10 % to more than 40 %. The mass of the molecular cloud is a normalisation factor for the calculated $\gamma$-ray flux and three different values, $M_{\mathrm{MC}}$ and $M_{\mathrm{MC}} \pm \Delta M_{\mathrm{MC}}$, are used in the parameter scan.

Figure 6.3 shows the result of the parameter scan in the form of a sky map. The coloured ellipses mark the radio position and extent of those molecular clouds with at least one parameter set that gives a detectable $\gamma$-ray flux. The magenta circles show the radio position and extent of the supernova remnants considered in this search, as listed in Table 6.1. The colour scale gives the ratio $f$ of parameter sets $n_{>\mathrm{sens,i}}$ with an integrated flux above 1 TeV larger than the sensitivity of the H.E.S.S. Galactic Plane Survey for the total number $n_{\mathrm{total}}$ of tested parameter sets. The flux sensitivity map with a correlation radius of 0.2°, as illustrated in Fig. 6.2, is used and the sensitivity $S_{\mathrm{AB}}$ is corrected for the area of the cloud as

$$S_{\mathrm{AB}} = S_{0.2^\circ} \cdot \frac{\sqrt{A \cdot B}}{0.2^\circ}, \tag{6.1}$$

with $A$ and $B$, the semi-major and minor axis of the cloud ellipse.
If more than one cloud might contribute to the emission at a certain sky location, the value $f$ is calculated as

$$f = 1 - \prod_i \left(1 - \frac{n_{>\mathrm{sens,i}}}{n_{\mathrm{total,i}}}\right) \tag{6.2}$$

for each contributing cloud $i$. The motivation of this presentation is given in the next Section 6.2.2.

In Fig. 6.3, 147 molecular clouds from the sample of about 750 clouds are illustrated. These clouds have at least one set of parameters that give a detectable $\gamma$-ray flux. 17 of these clouds could be illuminated by more than one supernova remnant and nine of those clouds are located in the region around the supernova remnants W44 and G035.6-00.4.
H.E.S.S. sources with the positions and extents taken from TeVCat are marked by ochre dashed circles, respectively ellipses, in Fig. 6.3. However, the source extents in TeVCat are not consistent due to different information given in the corresponding publications. The information is a mixture of intrinsic source size, observed $\gamma$-ray emission and extraction region used for the spectral analysis. Howevere, it is valid to take the H.E.S.S. source extents for illustration purpose.
Two H.E.S.S. sources, namely HESS J1923+141 and HESS J1911+090, are classified in TeVCat as supernova remnant/molecular cloud associations. Furthermore, there are three aditional sources, HESS J1858+020 , HESS J1852-000 and HESS J1834-087, classified as unidentified sources with a supernova remnant/molecular cloud associations as potential counter part. All of these five regions are revealed in the search for regions harbouring potentially detectable clouds presented here as illustrated in Fig. 6.3. This shows the search strategy, as describes above, is working and regions populated with potentially detectable molecular clouds are selected.

### 6.2.2 Interpretation

The parameter scan carried out gives for each supernova remnant/molecular cloud pair only the number of parameter sets that yield a certain $\gamma$-ray flux level and the number of total parameter sets tested for this pair. Thus, it is also possible to fill the sky map with 1 and 0, indicating whether at least one parameter set reaches the previously defined flux level or not. The skymap presented here in Fig. 6.3, however, contains additional information. The parameter $f$ as defined in Eq. 6.2 additionally indicates the uncertanties on the parameters apart from the presence of nearby clouds. In the following paragraph the representation of $f$ is motivated.
Formally, $f$ fulfills the probability axioms as defined, e.g., in Barlow (1989). In our scenario, two complementary events may occur: the events D, a “potentially detectable cloud”, and N, a “non-detectable cloud”. Any specific cloud belongs either to the category D, if at least one tested parameter set yields an integral flux larger than the flux sensitivity, or to N, if there is no parameter set, for which such a flux can be realised. The formal probability for a cloud to fall into category D can be defined as

$$P(D) = \frac{n_{I>\text{sens}}}{n_{\text{total}}} \tag{6.3}$$

and, consequently, the probability that the cloud belongs to N is

$$P(N) = \frac{n_{I<\text{sens}}}{n_{\text{total}}} = \frac{1 - n_{I>\text{sens}}}{n_{\text{total}}} = 1 - P(D), \tag{6.4}$$

with $0 \leq P(D) \leq 1$ and $0 \leq P(N) \leq 1$.
Further, the sum of the probabilities of the cloud to belong to D or N is 1, $\sum_{i=[D,N]} P(i) = 1$.
The probability that the MC belongs to D or N is also additive: $P(D \cup N) = P(D) + P(N)$.

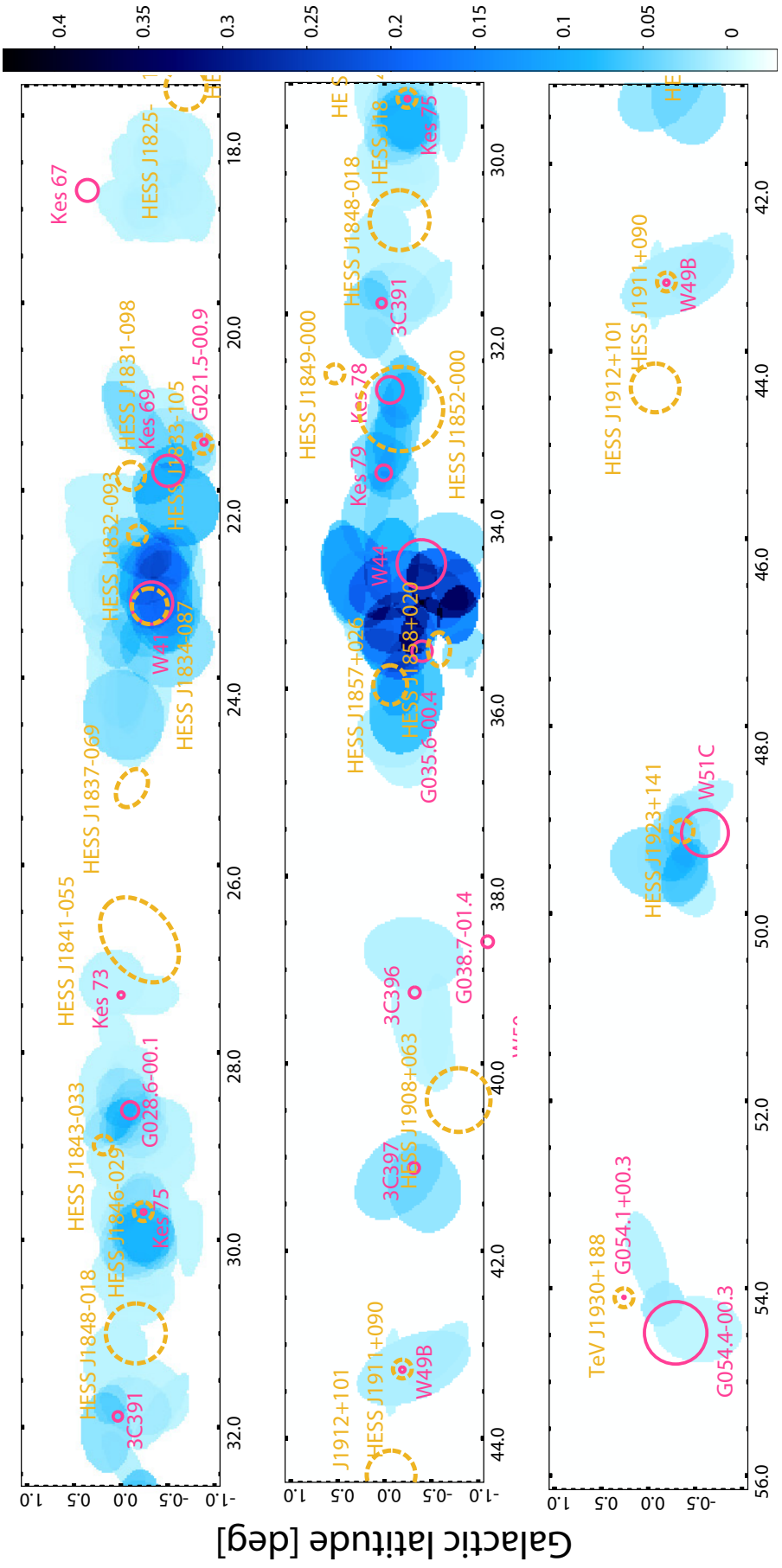


**Figure 6.3:** Sky map of the parameter $f$ as defined in Eq. 6.2 derived from the parameter scan from the molecular clouds of the Galactic Ring Survey and selected supernova remnants listed in Tab. 6.1. The coloured overlapping ellipses represent the positions and extents of the clouds. The magenta circles mark the radio positions and extents of the consirered remnants. The ochre circles, respectively ellipses, indicate the positions and extents of H.E.S.S. sources as listed in TeVCat.

In our scenario, the three-dimensional positions of clouds within the Galaxy are projected onto a two dimensional sky map. This results in many regions where more clouds located at the same line-of-sight overlapp. The parameter scan for each supernova remnant/molecular cloud is independent, hence, the above defined probabilites are independent for each supernova remnant/molecular cloud pair. Regarding the search for regions populated with potentially detectable clouds, only the probability to detect $\gamma$-ray emission from any cloud is interesting, not the one from a special one. Therefore, the probability for a sky region where $i$ MCs are located, that at least one MC belongs to the class D can be written as

$$1 - \prod_i P_{\mathrm{i}}(N) = 1 - \prod_i \left(1 - \frac{n_{>\mathrm{sens,i}}}{n_{\mathrm{total,i}}}\right). \tag{6.5}$$

This is the same formalism as for the parameter $f$ defined in Eq. 6.2 and motivates the illustration of the results from the parameter scan as done in this work in Fig. 6.3.

The paragraph above shows that the parameter $f$ is a real number satisfying the probability axioms. Regarding the physical interpretation of the parameter scan and the parameter $f$, there are, strictly speaking, no probabilites involved. The properties of the molecular cloud and supernova remnants are determined and the errors on the parameters only give the uncertanties to which level it is possible to estimate those.
The probability of a supernova remnant to be physically located at a distance of 3.8 kpc to Earth does not change whether the distance can be estimated from measurements as $4.0 \pm 0.2$ kpc or $4.0 \pm 2.0$ kpc. The distance between a supernova remnant and a molecular cloud, where the cloud could still emit detectable $\gamma$-ray emission, is smaller than 100 pc, depending on a lot of parameters and on the flux sensitivity of the experiment. Therefore, for the example given here, a distance of the supernova remnant of $4.0 \pm 0.2$ kpc and a nearby cloud at a distance of 3.85 kpc would result in an higher value of $f$ than for a remnant with a noted distance of $4.0 \pm 2.0$ kpc, because the larger distance uncertainty of the remnant leads to more parameter sets to test with the parameter scan. In this case a lower value of $f$ indicates larger uncertanties on the parameters of the tested supernova remnant/molecular cloud pair.
The value of $f$, however, increases, if there is a second cloud nearby at a distance of 3.5 kpc. The parameter scan for the distance of $4.0 \pm 2.0$ kpc covers the second cloud and additional parameter sets achieving the defined flux level arise and, hence, the value $f$ with a second cloud nearby for a distance of $4.0 \pm 2.0$ kpc is higher than with only one cloud nearby.
This example illustrates that the representation of the parameter $f$ on the sky map in Fig. 6.3 provides more information compared to a sky map filled with 0 and 1, since a higher value of $f$ either indicates a good knowledge about the region and/or indicates that there are at least a few potentially detectable clouds located nearby. With the given information on the parameters of supernova remnants and molecular clouds it is not possible to construct a probability to detect a cloud near a remnant at a certain sky location, but nevertheless the results derived here can be used to select different sky regions to take a closer look at.

### 6.2.3 Discussion of the W44 region

Within the coverage of the Galactic Ring Survey, the most prominent supernova remnant with ambient molecular clouds is the supernova remnant W44. W44 is surrounded by a complex of giant molecular clouds (e.g., Seta et al. (2004)). $^{13}$CO line emission from this molecular cloud complex is illustrated in Fig. 3.1. In the GeV $\gamma$-ray regime the shell of the supernova remnant was detected by *EGRET*[3] (as 2EG J1857+0018, Sturner & Dermer (1995)), *AGILE* (Giuliani et al., 2011) and also by *Fermi*-LAT (Abdo et al., 2010). In addition, two regions close to the shell were also detected by *Fermi*-LAT as reported by Uchiyama et al. (2012). These two regions are called *SRC*1 and *SRC*2 in the following. They coincide with ambient molecular clouds, and the $\gamma$-ray emission is interpreted to be produced by hadrons escaped from the supernova remnant and interacting with the ambient clouds. This argument is strengthened by the pion-decay signature observed in the energy spectrum of the GeV $\gamma$-ray emission, which was recently reported by Ackermann et al. (2013) and Cardillo et al. (2014).

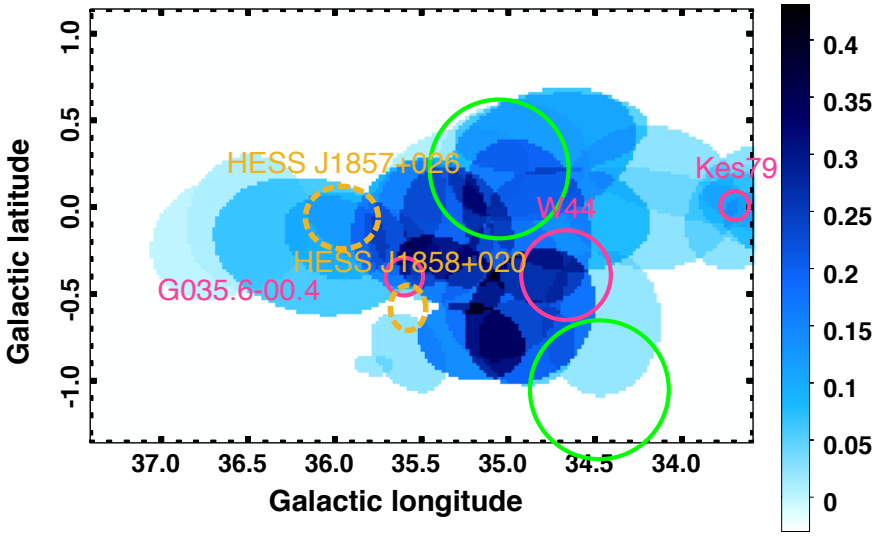


**Figure 6.4:** The region around the supernova remnants W44 and G035.6-00.4. The radio position and extents of the remnants are overlaid in magenta, the regions *SRC* 1 and *SRC* 2, identified by Uchiyama et al. (2012), are marked by green circles. The colour scale of the ellipses, representing the molecular clouds, show the value of the parameter $f$ as defined in Eq. 6.2. The position of H.E.S.S. sources are shown by the ochre dashed ellipses.

Figure 6.4 shows a sky map of the results from the parameter scan for the W44 region and the neighbouring SNR G035.6-00.4. The ellipses represent the molecular clouds and the colour scale gives the prameter $f$ as defined in Eq. 6.2 for clouds located along the same line-of-sight. The radio shells of the supernova remnants are overlaid in magenta and the GeV $\gamma$-ray emitting regions outside the shell *SRC* 1 and *SRC* 2, as reported in Uchiyama et al. (2012), are overlaid in green. H.E.S.S. sources located nearby are overlaid in ochre.
The W44 region exhibits the largest values for the parameter $f$ in the search region as presented in Section 6.2.1. There are three specific circumstances explaining this unique role of the W44 region: First, the distance ranges of both SNRs used in the parameter scan are small as listed in Table 6.1. Second, W44 is located in a molecular cloud complex, in which the Galactic Ring Survey identifies several individual clouds. Therefore, there are 33 clouds, potentially illuminated by particles escaping from one of the both supernova remnants in that region. Third, nine molecular clouds which can be illuminated by particles

[3] **E**nergetic **G**amma **R**ay **E**xperiment **T**elescope

escaping from both remnants are located in the region between W44 and G035.6-00.4. As explained in Section 6.2.2, a higher value for $f$ does not necessarily imply, that there is the highest chance to detect $\gamma$-ray emission from molecular clouds in the TeV domain. Infact, no significant TeV $\gamma$-ray emission has been reported so far from the W44 region. By contrast, the W51C and W49B region, both with smaller $f$ values due to larger ranges of their distances, are established supernova remnant/molecular cloud associations in the TeV band.

The very complex molecular environment around W44 makes it difficult to use this region to constrain the diffusion coefficient as at least 33 molecular clouds could be illuminated by particles escaping the remnant W44 or the adjacent one G035.6-00.4. Calculations of the combined fluxes considering the distance uncertainties of all potentially participating clouds cannot constrain the parameter space of the diffusion coefficient, as the span of the integrated fluxes is too large due to the combination of the different cloud distances.

Even though no significant TeV $\gamma$-ray emission is reported so far for the W44 region, a detection with the next generation experiment CTA is expected based on the GeV observations of the $\gamma$-ray emitting molecular clouds outside the shell and the extrapolation of the $\gamma$-ray emission modeled by Uchiyama et al. (2012) to higher energies. The complex surrounding complicates the modeling of $\gamma$-ray emission of the individual clouds because of the large distance uncertainties and the large number of clouds that could contribute in principle to the $\gamma$-ray emission. Therefore, for studies regarding the propagation of high-energetic particles, regions with simpler environments are better suited, such as the regions around the supernova remnants Kes 73, 3C391, 3C396, 3C397, W49B, W51C and G054.4-00.3 as shown in Fig. 6.3.

## 6.3 Constraints on the diffusion coefficient

The aim of the analysis presented in this section is to derive a constraint on the diffusion coefficient using the number of TeV sources identified as supernova remnant/molecular cloud associations and the sample of clouds from the Galactic Ring Survey. The diffusion coefficient, as used in this work, is defined as $D(E) = D_{10}\,(E/10\,\mathrm{GeV})^s\,\mathrm{cm}^2\,\mathrm{s}^{-1}$ with $s \in [0.3; 0.7]$, see, e.g., Gabici et al. (2009). $s$ is the energy dependence and $D_{10}$ is the normalisation at 10 GeV of the diffusion coefficient. While the Galactic average is $D_{10} \approx 10^{28}$ (Strong et al., 2007), the local value in dense regions near supernova remnants might be lower by up to two orders of magnitude due to a stronger and more turbulent magnetic field. This suppression of the diffusion coefficient has been mainly derived for the W28 region (Gabici et al., 2010; Li & Chen, 2010; Ohira et al., 2011; Yan et al., 2012).

The ansatz presented here to constrain the diffusion coefficient for regions near supernova remnants, is based on the comparison of the number of detectable molecular clouds, derived from a simulation of supernova remnant populations and the molecular clouds from the Galactic Ring Survey, with the number of detected and identified supernova remnant/molecular cloud associations in the TeV band. This approach using populations instead of individual regions can constrain the average diffusion properties for dense regions near supernova remnants. This work studies which constraints on the difussion coefficient can be achieved with the H.E.S.S. Galactic Plane Survey and the clouds from the Galactic Ring Survey as presented in Section 6.3.1 and discusses propects of the next generation experiment, the CTA observatory, in Section 6.3.2.

### 6.3.1 Results obtained with H.E.S.S.

The search for potentially $\gamma$-ray emitting molecular clouds detectable in the H.E.S.S. Galactic Plane Survey in the previous section considers only supernova remnants for which age and distance estimates are available. More than 70 supernova remnants, detected in the radio band, are located in the region covered by the Galactic Ring Survey, but for only 22 remnants the age and distances have been derived. Therefore, the considered supernova remnant sample might be biased by selection effects. One selection effect refers generally to the identification of supernova remnants in the radio band (Green, 2009): in particular, faint supernova remants and remnants with a small angular size are difficult to identify. The second selection effect stems from the criterion of estimated age and distance. Thus, the results derived in Section 6.2 are only valid under the assumption that there are no additional accelerators in the vicinity of the clouds from the Galactic Ring Survey. And, of course, there is a selection bias on the molecular cloud sample as well, as discussed in 5.1, but the selection biases on the supernova remnant sample dominate here.

The ansatz of this study is based on simulated populations of supernova remants, avoiding the problem of selecting only remnants with known age and distance. The simulated populations used in this section are provided by Hahn (2014). The analysis presented here uses the following parameters of the simulated supernova remants: the position of the remnant in the galaxy and the age of the remnant. In the following only the derivation of those parameters is described. The location of core-collapse supernova remnants are generated considering a four-arm spiral structure as parametrised in Vallée (2005) and the barred-spiral structure of Freudenreich (1998). For the location of remnants of type Ia supernovae[4] a uniform distribution within the galaxy was assumed. A ratio of four core-collapse supernovae to one supernova Ia was used. The radial distribution of the simulated remnants within the galaxy follows model (c) from Green (2012), obtained from the sample of observed bright supernova remnants. The time between two supervnovae was sampled from a Poisson distribution with a mean value of 33 years. A rate of three supernovae per hundred years per galaxy was assumed since a supernova rate for the Milky Way Galaxy of $2.84 \pm 0.60$ supernovae per century was derived by Li et al. (2011).

For each supernova remnant/molecular cloud pair per simulated population of supernova remnants the integral $\gamma$-ray flux is calculated using the model by Gabici et al. (2009) for three different diffusion coefficients $D_{10}$: $10^{26}\,\mathrm{cm^2\,s^{-1}}$, $10^{27}\,\mathrm{cm^2\,s^{-1}}$ and $10^{28}\,\mathrm{cm^2\,s^{-1}}$. A Sedov time of 200 yr and an efficiency of 30 % for the conversion of the supernova explosion energy of $10^{51}$ erg into acceleration of particles are assumed here. The derived $\gamma$-ray flux is compared with the sensitivity of the H.E.S.S. Galactic Plane Survey corrected for the spatial extent of the cloud as defined in Eq. 6.1. The number of detectable molecular clouds, i.e., supernova remnant/molecular cloud pairs with an integral $\gamma$-ray flux larger than the corrected sensitivity, per simulated supernova remnant population is shown exemplarily in Fig. 6.5 for three different diffusion coefficients and an energy dependence $s = 0.5$. The results presented here were derived using 1000 simulated populations of supernova remnants. The mean and median value as well as the standard deviation of the distributions of the number of detectable clouds per supernova remnant population for three different values of $D_{10}$ and $s$ are listed in Table 6.3.

[4] A supernova of type Ia is a supernova explosion off a white dwarf accreting matter of a companion star until the conditions for a thermonuclear explosion are fullfilled.

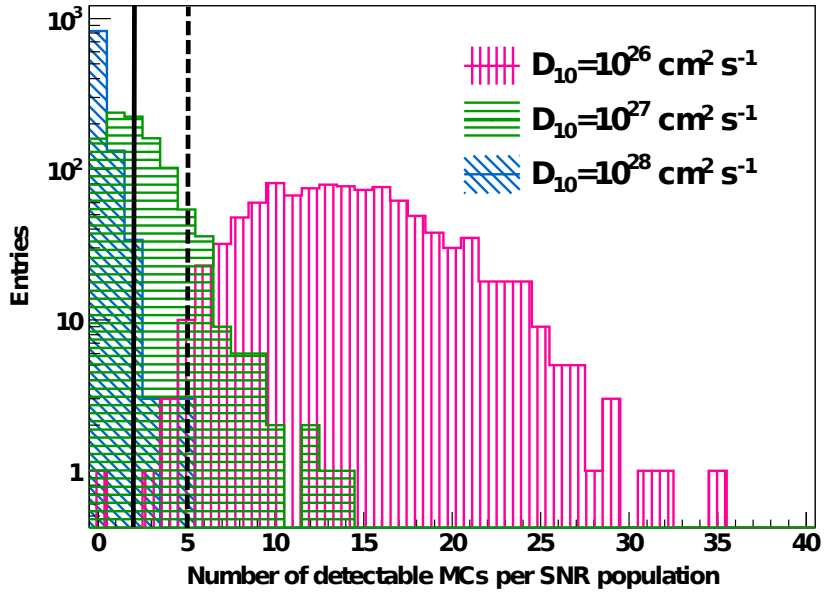


**Figure 6.5:** Number of molecular clouds (MCs) with TeV emission detectable by H.E.S.S. per simulated supernova remnant (SNR) population for three different diffusion coefficients and an energy dependence $s = 0.5$. The black solid line represents the number of established supernova remnant/molecular cloud associations in the TeV band, the dashed black line considers additionally three unidentified TeV sources with a supernova remnant/molecular cloud association as potential counterpart.

**Table 6.3:** Mean, standard deviation and median for the number of clouds detectable with H.E.S.S. per supernova remnant population for different diffusion coefficients $D_{10}$ and energy dependence $s$. The table entries are listed as: mean / standard deviation / median of the individual distributions.

| | $s$= 0.3 | $s$= 0.5 | $s$=0.7 |
|---|---|---|---|
| $D_{10}$ [cm$^2$ s$^{-1}$]=$10^{26}$ | 11.1 / 4.1 / 11 | 14.3 / 5.0 / 14 | 4.5 / 2.7 / 4 |
| $D_{10}$ [cm$^2$ s$^{-1}$]=$10^{27}$ | 12.0 / 4.6 / 11.5 | 2.3 / 2.0 / 2 | 0.5 / 0.8 / 0 |
| $D_{10}$ [cm$^2$ s$^{-1}$]=$10^{28}$ | 1.3 / 1.4 / 1 | 0.2 /0.6 / 0 | 0.0 / 0.1 / 0 |

For any energy coefficients $s$, a high diffusion coefficient $D_{10}$ of $10^{28}\,\mathrm{cm^2\,s^{-1}}$ will efficiently suppress the number of detectable clouds. Reducing the normalisation $D_{10}$ to $10^{27}\,\mathrm{cm^2\,s^{-1}}$ results in up to twelve detectable clouds per population of supernova remnants with pronounced variations with the energy dependence $s$. Four to fourteen detectable clouds would be expected with a lower value for $D_{10}$ of about $10^{26}\,\mathrm{cm^2\,s^{-1}}$. These numbers can be compared with the number of actually detected supernova remnant/molecular cloud associations in the TeV band within the range of the Galactic Ring Survey.

According to TeVCat, two H.E.S.S. sources within the coverage of the Galactic Ring Survey are classified as interacting systems of a supernova remnant/molecular clouds: HESS J1911+090 with the supernova remnant W51C and HESS J1923+141 with W49B. Three more sources, listed as unidentified, have supernova remnant/molecular cloud associations as potential counter parts. These are HESS J1858+020, HESS J1852−000 and HESS J1834−087. The two identified supernova remnant/molecular cloud interactions are the lower limit of the number of detectable cloud. Further supernova remnant/molecular cloud interactions might be detectable, but were possibly not detected because of a stronger TeV $\gamma$-ray source nearby or are listed as unidentified source due to too many potential counter parts. It is, therefore, not possible to derive an upper limit of detectable clouds from the number of identified ones. The number of two identified supernova remnant/molecular cloud associations is denoted in Fig. 6.5 as solid line, the number of five, consisting of the two identified and the additional the three candidates is represented by the dashed line.

With the number of two established supernova remnant/molecular cloud associations as lower limit and three additional candidates it is possible, under all the assumptions that were made in the model of Gabici et al. (2009) and the values adopted in this work, to exclude a diffusion coefficient of $10^{28}\,\mathrm{cm^2\,s^{-1}}$ as average diffusion coefficient for regions near supernva remnants. The number of identified supernova remnant/molecular cloud associations is consistent with a diffusion coefficient of $10^{27}\,\mathrm{cm^2\,s^{-1}}$ and also with $10^{26}\,\mathrm{cm^2\,s^{-1}}$ for various assumed energy dependences of the diffusion coefficient even with the three unidentified sources with potential supernova remnant/molecular cloud counterparts. However, it is not possible to constrain the energy dependence except for an exclusion of $s = 0.7$ for a normalisation $D_{10}$ of the diffusion coefficient of $10^{27}\,\mathrm{cm^2\,s^{-1}}$. For $D_{10} = 10^{26}\,\mathrm{cm^2\,s^{-1}}$ and a lower limit of two detectable clouds no constraint on the energy dependence seems possible.

### 6.3.2 Prospects with CTA

The CTA observatory is the next-generation imaging Cherenkov telescope array designed for studies of $\gamma$-ray astrophysics in the energy range between 30 GeV and 100 TeV. The sensitivity of CTA will be one order of magnitude better compared to today's imaging Cherenkov telescope systems such as H.E.S.S., MAGIC and VERITAS (Actis et al., 2011).

With a better sensitivity and a larger energy range, CTA is expected to substantially increase the number of detected supernova remnant/molecular cloud associations compared to the number of already established ones. For the calculation of the expected number of detectable clouds per simulated population of supernova remnants the same strategy as in Section 6.3.1 is applied. Despite the lower energy threshold achieved with CTA, an energy threshold of 1 TeV is chosen to limit the number of clouds which would be detectable by just being embedded in the cosmic-ray sea. An integral flux sensitivity of $2.8 \cdot 10^{-14}\,\mathrm{cm^{-2}\,s^{-1}}$ above 1 TeV (Actis et al., 2011) is adopted. This integral flux sensitivity is derived for a point source observed for 50 hrs at a zenith angle of 20° and a $\gamma$-ray energy spectrum following a power law with index −2.57. An angular resolution of 0.04° at 1 TeV (Bernlöhr et al., 2013) is

assumed to correct the integral flux sensitivity for an extended source using Eq. 6.1 with 0.04° instead of 0.2°. The mean and median value as well as the standard deviation of the distributions of the number of molecular clouds expected to be detectable with CTA per simulated population of supernova remnants for three different values of $D_{10}$ and $s$ are listed in Table 6.4.
Due to the better sensitivity of CTA, for almost all combinations of $D_{10}$ and $s$ the number of clouds detectable with CTA is more than twice as high as for H.E.S.S. However, it will remain difficult to distinguish, for example, between a diffusion coefficient of $1.0 \cdot 10^{27}$ with an energy dependence of 0.3 and a diffusion coefficient of $1.0 \cdot 10^{26}$ with an energy dependence of 0.5 based on the number of supernova remnant/molecular cloud associations detected with CTA.

**Table 6.4:** Mean, standard deviation and median for the number of clouds detectable with CTA per population of supernova remnant for different diffusion coefficients $D_{10}$ and energy dependence $s$. An integral flux sensitivity of $2.8 \cdot 10^{-14}\,\mathrm{cm}^{-2}\,\mathrm{s}^{-1}$ above 1 TeV and an angular resolution of 0.04° are assumed. The table entries are listed as: mean / standard deviation / median of the individual distributions.

| | $s$= 0.3 | $s$= 0.5 | $s$=0.7 |
|---|---|---|---|
| $D_{10}$ [$\mathrm{cm}^2\,\mathrm{s}^{-1}$]=$10^{26}$ | 18.5 / 5.8 / 18 | 34.3 / 8.8 / 34 | 17.6 / 6.0 / 17 |
| $D_{10}$ [$\mathrm{cm}^2\,\mathrm{s}^{-1}$]=$10^{27}$ | 36.1 / 9.2 / 35 | 9.6 / 4.6 / 9 | 1.8 / 0.8 / 1 |
| $D_{10}$ [$\mathrm{cm}^2\,\mathrm{s}^{-1}$]=$10^{28}$ | 5.3 / 3.3 / 5 | 1.0 / 1.3 / 1 | 0.1 / 0.5 / 0 |

## 6.4 Conclusion

This chapter focused on $\gamma$-ray emitting molecular clouds near supernova remnants. As presented in Section 6.1, the sensitivity of the H.E.S.S. Galactic Plane Survey allows to detect molecular clouds up to 100 pc away from the supernova remnant depending on age and diffusion coefficient. Therefore, the H.E.S.S. Galactic Plane Survey is well suited to study $\gamma$-ray emitting molecular clouds in the TeV band.
The search for regions populated with potentially detectable $\gamma$-ray emitting molecular clouds near supernova remnants presented in this chapter used about 750 molecular clouds from the Galactic Ring Survey and 22 supernova remnants with estimated age and distance selected from the catalogue of Ferrand & Safi-Harb (2012). The search results reveal regions with potentially detectable molecular clouds. While W44 certainly represents the most prominent region, due to the very complex molecular environment it is not very well suited for a study aiming to constrain the diffusion coefficient. For this purpose, supernova remnants with a simpler environment - as Kes 73, 3C391, 3C396, 3C397, W49B, W51C and G054.4-00.3 - are better suited. The region around the supernova remnant 3C391 is analysed in the TeV band using observations of the H.E.S.S. experiment, see Chapter 7.
The study described in Secion 6.3 can constrain the average normalisation of the diffusion coefficient for dense regions near supernova remnants to be smaller than $10^{28}\,\mathrm{cm}^2\,\mathrm{s}^{-1}$. This result was obtained using simulated supernova remnant populations and the molecular clouds from the Galactic Ring Survey as well as the theoretical model of Gabici et al. (2009) to calculate the expected number of detectable molecular clouds. This number was compared to the number of identified supernova remnant/molecular cloud associations in the TeV band including sources classified as unidentified but with a supernova remnant/molecular cloud

association as potential counterpart. The future experiment CTA will detect more supernova remnant/molecular cloud associations, but it will still remain challenging to constrain the energy dependence of the diffusion coefficient from $\gamma$-ray observations of molecular clouds.

CHAPTER 7

# The region around the supernova remnant 3C391 revealed in TeV gamma-rays

The search for detectable molecular clouds presented in Section 6.2 revealed regions populated with potentially detectable $\gamma$-ray emitting clouds where no $\gamma$-ray emission was reported so far. One of those regions interesting to look at is the area around the supernova remnant 3C391. Figure 7.1 shows that region on the sky map derived from the parameter scan results.

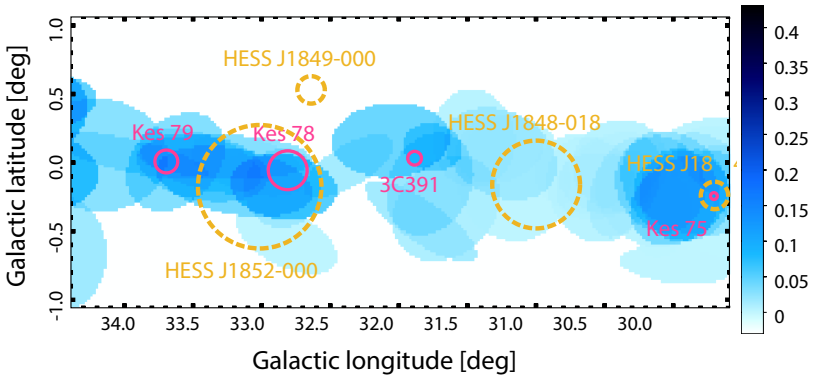


**Figure 7.1:** Results from the parameter scan for the region surrounding 3C391. The coloured ellipses represent the position and extension of the molecular clouds. The colour scale gives the ratio of parameter sets which resulted in integral fluxes larger than the sensitivity of the H.E.S.S. Galactic Plane Survey in this region as explained in Section 6.2. The magenta circles show the radio position and extent of the supernova remnants considered in the search and the ochre dashed circles denote the position of H.E.S.S. sources from TeVCat.

3C391 is a mixed-morphology supernova remnant (Rho & Petre, 1998), characterised by a centre-filled X-ray and shell-like radio morphology. The radio and X-ray morphology of 3C391 is shown in Fig. 7.2. The radio emission in Fig. 7.2(a) shows a very inhomogenous structure with bright emission at the northern rim of the remnant and fainter radio emission

in the south. That kind of morphology is often referred to as “break-out” morphology and can be explained by the evolution of a supernova remnant in an ambient medium with large density gradient. X-ray emission observed from the supernova remnant is shown in the composite image in Fig. 7.2(b) in blue, the radio emission on this figure is coloured in red. The X-ray emission is, contrary to the bright radio emission at the northern rim of the remnant, more compact on the southern part and does not show any shell-like structure.
The distance of 3C391 is estimated as $7.2 - 8.6\,\mathrm{kpc}$ (Ferrand & Safi-Harb, 2012) based on measurements of absorption features in the line emission of neutral hydrogen (HI) (Radhakrishnan et al., 1972) putting it behind the tangent point of 7.2 kpc. The age is estimated to be $\approx 4 \cdot 10^3$ yr using the post-shock temperature measured from X-ray emission (Chen et al., 2004). The same authors estimated the energy of the supernova explosion to be about $(0.3 - 1.4)/\cdot 10^{51} (r_{\mathrm{SNR}}/3')^3 (d_{\mathrm{SNR}}/8\,\mathrm{kpc})^3 (n_0/0.3\,\mathrm{cm}^{-3})$ erg with the radius of the remnant $r_{\mathrm{SNR}}$ and a pre-shock gas density $n_0$.

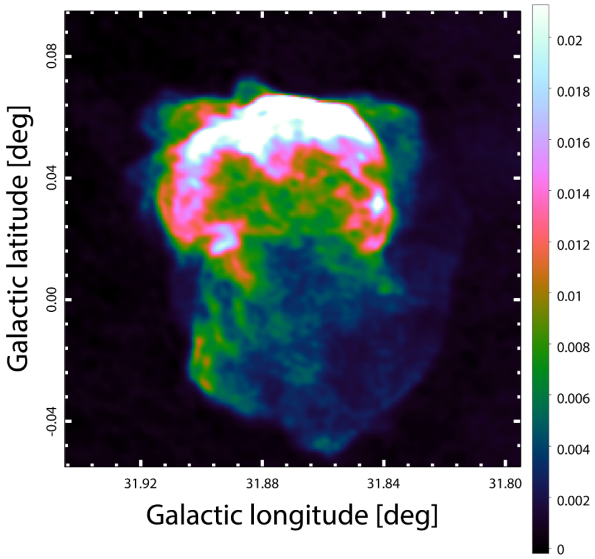


(a) Radio morphology of the supernova remnant 3C391. The image was generated using data from the MAGPIS[2]Galactic plane survey (White et al., 2005) in the 20 cm band.

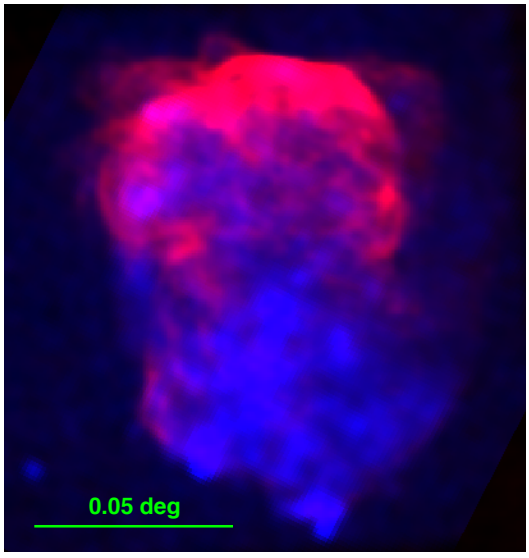


(b) Composite image with radio and X-ray emission observed from the supernova remnant 3C391. The radio emission is coloured in red and the X-ray emission in blue. The image of the X-ray was produced using *Chandra* data, obs ID:2786

**Figure 7.2:** Morphology of the supernova remnant 3C391 in the radio and X-ray band.

The supernova remnant is located at the edge of a molecular cloud, and CO observations of this region reveal that the remnant is interacting with the cloud (Wilner et al., 1998; Reach & Rho, 1999). This is further supported by the detection of OH maser emission at the shell of the remnant. Frail et al. (1996) observed OH maser emission at $\approx 105\,\mathrm{km\ s^{-1}}$ and $\approx 110\,\mathrm{km\ s^{-1}}$. An additional OH maser emission component was observed by Hewitt et al. (2008) at $\approx 97\,\mathrm{km\ s^{-1}}$. They also confirmed the emission observed by Frail et al. (1996).
X-ray observation of 3C391 with *Einstein*[3] (Wang & Seward, 1984; Seward, 1990), *ROSAT*[4] (Rho & Petre, 1996, 1998), *ASCA*[5] (Chen & Slane, 2001) and *Chandra*[6] (Chen et al., 2004)

[2]**M**ulti-**A**rray **G**alactic **P**lane **I**maging **S**urvey
[3]The name of the observatory was changed after launch to honour Albert Einstein
[4]**Rö**ntgen **sat**ellite, named in honour of Wilhelm Röntgen
[5]**A**dvanced **S**atellite for **C**osmology and **A**strophysics
[6]named after the Indian-American astrophysicist Subrahmanyan Chandrasekhar

reveal only thermal emission from the centre of the remnant.
GeV $\gamma$-ray emission detected with *Fermi*-LAT in the 3C391 region was reported by Castro & Slane (2010) and Nolan et al. (2012). Both analyses show significant $\gamma$-ray emission associated with the supernova remnant 3C391 and a power-law energy spectrum with a spectral index $\approx -2.3$. The observed GeV emission as well as the results from the search in Section 6.2 motivate a closer look at the region around 3C391 within the H.E.S.S. data.
The analysis of 80 hours of observations taken by the H.E.S.S experiment reveals significant $\gamma$-ray emission in the region around the supernova remnant 3C391 where no VHE $\gamma$-ray emission was reported so far. The analysis and the obtained results are presented in Section 7.1. Section 7.2 focuses on the morphological and spectral properties of the observed emission around 3C391. In Section 7.3 is discussed whether the observed emission can be explained by $\gamma$-ray emitting molecular clouds in the surrounding of 3C391.

## 7.1 Analysis of H.E.S.S. data for the 3C391 region

The analysis of the region around the supernova remnant 3C391 in the TeV band uses 79.5 hr of observations taken with the H.E.S.S. telescope system (phase I). Observations with the target position of the run less than 2° away from the position of the supernova remnant are used. The mean zenith angle is about 27°. Almost none of the used observation runs were directly pointed toward the 3C391 region. Instead, the data set is comprised of runs at the nearby sources HESS J1849-000 and on the W43 region or are scan observations of the H.E.S.S. Galactic Plane Survey. Therefore, the events have a mean offset from the camera centre of 1.44°. The observation runs have a mean optical efficiency of 54%. The analysis was carried out with the Model++ software version paris-0-8-24 and to derive the results presented in this Chapter. The point spread function for the data set has a 68% containment radius of 0.055°. This value already considers the systematic extent of 0.003° reported in Deil et al. (2014). The significance and excess sky maps of the TeV emission are generated using the ring background method introduced in Section 4.2.2. The default exclusion regions from the database were used. Other exclusion regions were also generated using the method of Carrigan et al. (2012) and tested. A short discussion on the different exclusion regions can be found in the Appendix A.
Figure 7.3 shows the $\gamma$-ray significance sky map for the region of the supernova remnant 3C391 using the standard selection configuration (see Table 4.1) and a correlation radius of 0.22°. The correlation radius was chosen to search for extended sources (Aharonian et al., 2005a). The white dashed circle in Fig. 7.3 indicates the radio position and extension of 3C391. Three nearby TeV $\gamma$-ray sources, HESS J1849–000 (Terrier et al., 2008), HESS J1852+000 (Kosack & the H.E.S.S. Collaboration, 2011) and the W43 region, HESS J1848–018 (Chaves et al., 2008), are also marked on the sky map. The analysis reveals significant $\gamma$-ray emission around the radio position of 3C391 with a peak significance of $9.1\,\sigma$ at (l,b)= $(31°56'22.5'', 0°07'11.7'')$. The significance values presented here are pre-trial values. A conservative approach to estimate the number of trials is to take the number of pixels of the sky map. The sky map covers the region of $3° \times 3°$ and is binned in 0.01°. This results in 900 pixels and therefore 900 trials. A pre-trial significance of $8\,\sigma$ results for 900 trials in a post significance of more than $7\,\sigma$. The post-trial significance is estimated as discussed in Section 4.2.2. The number of 900 trials might be overestimated depending on the search window for emission spots, but the observed emission remains significant also considering the potential trial factors.

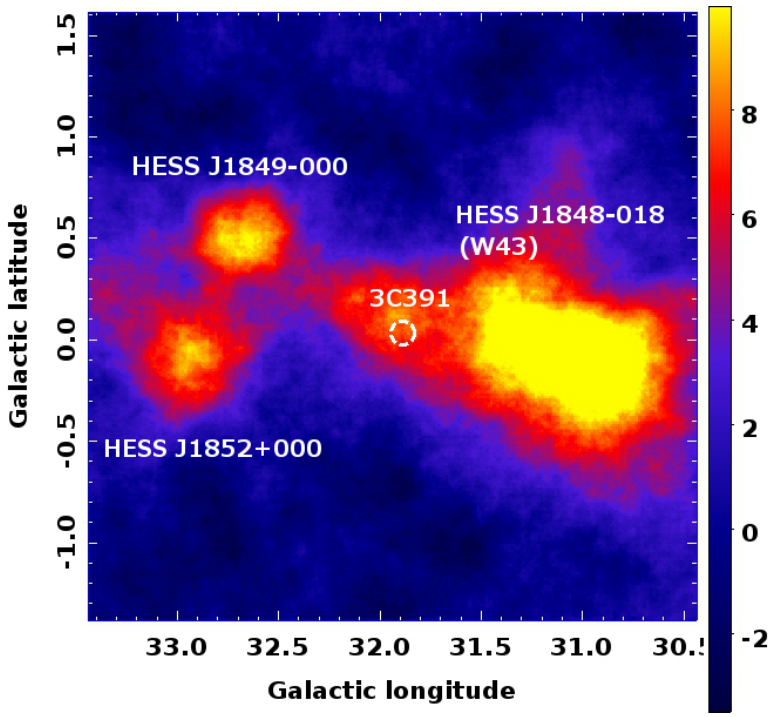


**Figure 7.3:** $\gamma$-ray significance sky map generated with a correlation radius of 0.22°. The white dashed circle indicates the radio position and extent of the supernova remnant 3C391. The nearby H.E.S.S. sources HESS J1849–000, HESS J1852+000 and HESS J1848–018 (W43 region) are also marked on the map.

## 7.2 Morphological and spectral properties of the gamma-ray emission

As the significance map in Fig. 7.3 shows the area of the supernova remnant 3C391 is located right in the Galactic plane in a rather complex environment with several nearby H.E.S.S. sources. The morphological properties of the observed $\gamma$-ray emission for a region centered on $(31.2°, 0.0°)$ and with a radius 1.5° are investigated using the morphology module from the software paris-0-8-24-scons. This region was selected to exclude the nearby sources HESS J1849–000 and HESS J1852+000 and to focus on the emission around 3C391 and the nearby source HESS J1848–018. The $\gamma$-ray emission from this region can be described with a Gaussian component near 3C391 and a larger asymmetric Gaussian component for HESS J1848–018. This two-source scenario is prefered with $7.7\,\sigma$ to one-source scenarios as listed in Tab. 7.1. The morphological parameters derived with a loglikelihood fit are listed in Tab.7.2.

**Table 7.1:** Comparison of three different morphological models for HESS J1848–018 and the 3C391 region. The likelihood values of the various fits are given as $\ln(L)$.

| Model | Number of parameters | $\ln(L)$ |
|---|---|---|
| One-source model: 1 Gaussian | 4 | -40275.9 |
| One-source model: 1 asym. Gaussian | 6 | -40173.7 |
| Two-source model: 1 Gaussian & 1 asym. Gaussian | 10 | -17689.5 |

**Table 7.2:** Model parameters for the region of HESS J1848–018 and the 3C391 region derived from the morphology fit using the two-sources model.

| | 3C391 | HESS J1848–018 |
|---|---|---|
| Model | Gaussian | assymetric Gaussian |
| Amplitude [$s^{-1}\,deg^{-2}$] | 0.00128 ± 0.00044 | 0.0209 ± 0.0013 |
| Longitude | 31°58′13.2″± 0°1′46.4″ | 31°6′7.8″ ± 0°1′50.8″ |
| Latitude | 0°8′15″ ± 0°1′44.9″ | −0°3′50.1″± 0°1′4.4″ |
| Extension 1 | 0°6′7.2″ ± 0°1′29.5″ | 0°30′33.6″ ± 0°2′19.9″ |
| Extension 2 | 0 ± 0 | 0°18′22.3″ ± 0°0′58.8″ |
| Angle | 0 ± 0 | 344°9′1.7″ ± 4°17′23.2″ |

Figure 7.4(a) shows the preferred morphological model in arbitrary units and Fig. 7.4(b) the $\gamma$-ray excess map obtained with standard cuts and smoothed with a Gaussian width of 0.08°. This width is the corresponding two-dimensional 68 % containment radius of the point spread function with a one-dimensional radius of about 0.055°. The Gaussian and the asymmetric Gaussian component are overlaid as circle, respectively ellipse. An extraction region was chosen to further investigate the spectral properties of the $\gamma$-ray emission. The green dashed circle shows the extraction region centred on the fit position of the Gaussian component. Its width of 0.16° radius is motivated by the two-dimensional 68% containment radius of one-dimensional one slightly larger than 0.1°.
Using this morphological model it is possible to estimate the excess within the extraction region originating from the Gaussian component sitting on the tail of the nearby source HESS J1848–018. The number of counts only from the Gaussian function is compared to the number of counts using the combined functions. The model parameters are varied 10 000 times within the errors derived from the morphology fit and for each simulation a fraction of excess originating from the Gaussian component near 3C391 is calculated. Figure 7.5(b) shows the distribution for the derived excess only from this Gaussian source component. This estimation gives a fraction of 69.8% ± 0.1% and results in a contamination of about 30 % originating from the neighbouring source within the extraction region. The error of 0.1% is the statistical error derived from the standard deviation of the distribution.

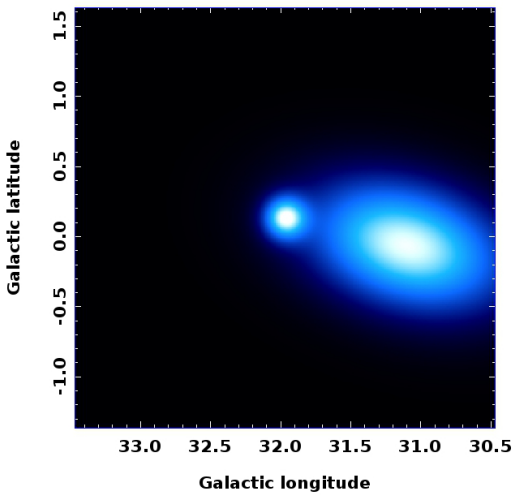


(a) Morphological model with one symmetric and one asymmetric Gaussian component obtained from the morphology fit.

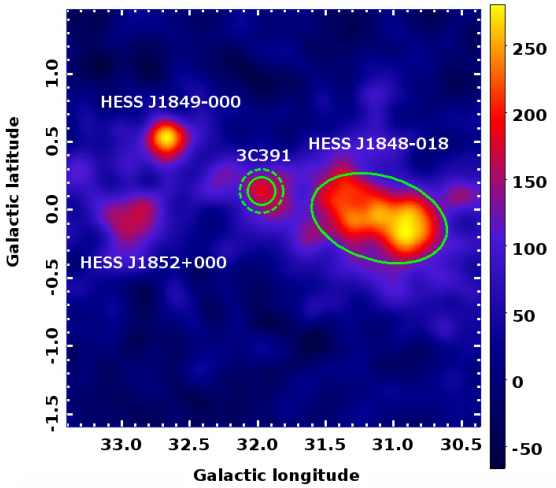


(b) TeV $\gamma$-ray excess map Gausian-smoothed with a kernel of 0.08°. The solid lines represent the morphological model and the dashed line shows the position and extent of the extraction region used for spectral analysis.

**Figure 7.4:** Morphological model and TeV $\gamma$-ray excess map for the region around 3C391 and HESS J1848–018.

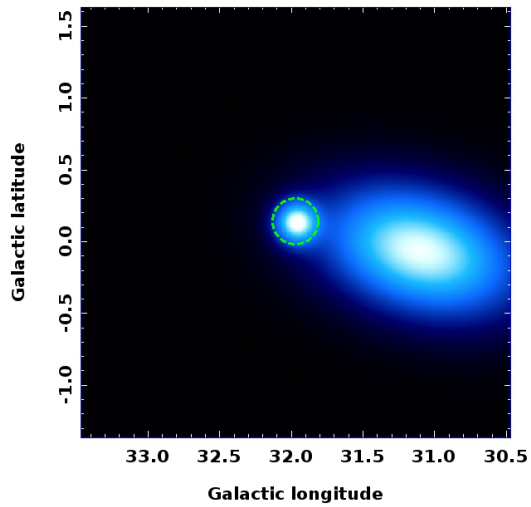


(a) Morphological model with one symmetric and one asymmertic Gaussian component derived from the morphology fit. The extraction region is overlaid as a green dashed circle.

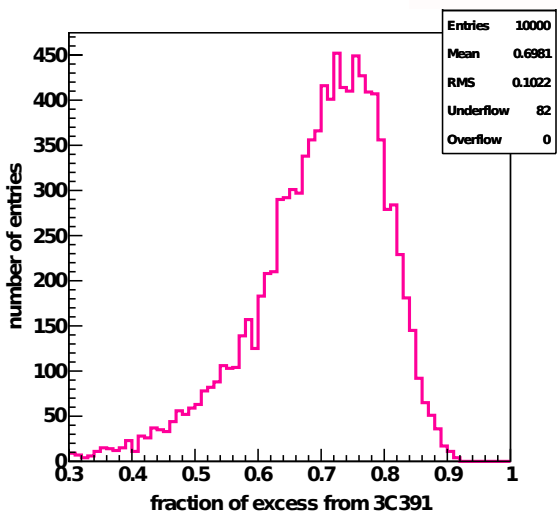


(b) The distribution of fraction of excess from the symmetric Gaussian component only for 10000 variations of the morphology parameters within the given errors.

**Figure 7.5:** Fraction of excess counts from the single Gaussian component only derived using the morphological model.

It is possible to estimate the number of excess counts that might originate from the neighbouring source using an alternative approach with test regions. This method places regions with the same size as the extraction region at the same distance from the adjacent source HESS J1848–018 and counts the number of excess photons within those. Potential test regions for this purpose are shown in Fig. 7.6. The statistics for the individual test regions are listed in Tab. 7.3. The same exclusion regions as for the extraction region were used to derive the number of remaining excess counts within the various test regions. The average number of excess counts for twelve test regions is $\bar{N}_\gamma = 148.5$. Test region #7 was ignored because this region has an excess of 360.2 counts with a significance of almost $9\,\sigma$. This might be a hint for another $\gamma$-ray source and considering this excess for the average excess would lead to a overestimation.
By contrast, the excess in region #8 with 222.4 counts with a significance of $5.4\,\sigma$ is considered, because there is a large-scale diffuse $\gamma$-ray component along the Galactic plane (H.E.S.S. Collaboration: A. Abramowski et al., 2014) and the excess seen here might originate from this or from another $\gamma$-ray source. In case, it originates from a large-scale emission peaked at Galactic latitude 0.0° (Terrier, 2014), this component would also influence the extraction region and hence the excess in region #8 is kept. Therefore all remaining twelve test regions are considered.

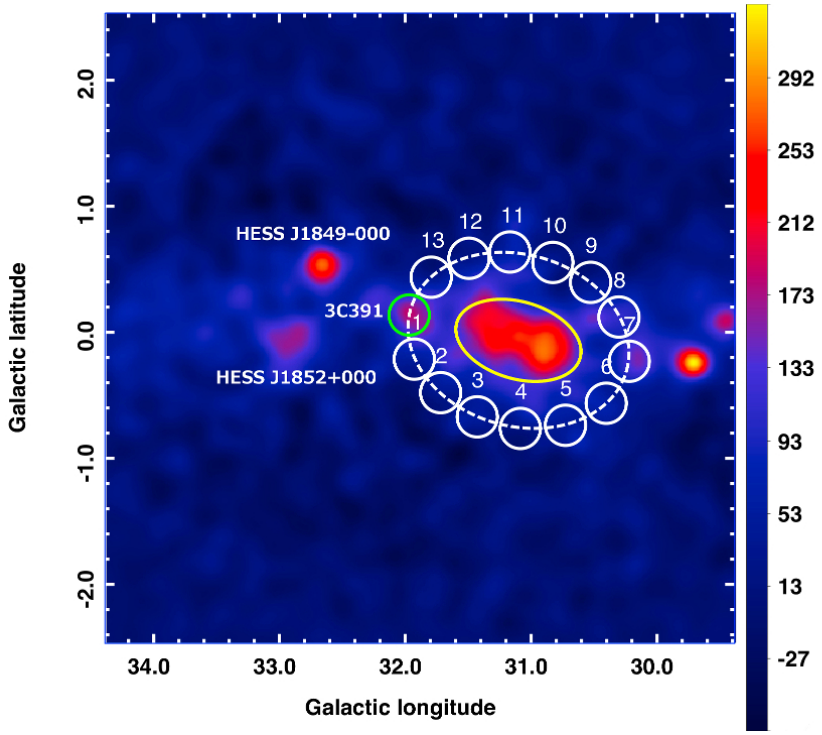


**Figure 7.6:** The positions of the test regions are indicated by the white circles on the TeV $\gamma$-ray excess map. These regions have the same size as the extraction region (green circle) and the same distance to the source HESS J1848–018. The morphological model for HESS J1848–018 is indicated by the yellow ellipse.

The number of average excess counts $\bar{N}_\gamma$ within the test regions, $\bar{N}_\gamma = 148.5$, was determined from the sum of the excess counts multiplied with the ratio of the acceptance-corrected live time of the respective test regions and the acceptance-corrected live time of the analysis region of 46.8 hr. This was done to consider the potentially lower excess counts in the test regions due to larger offset or less observation time.

**Table 7.3:** Event statistics for various test regions used to estimate the contamination from the nearby source HESS J1848–018. All regions have a radius of 0.16°. Coordinates are given in the Galactic system. The live times listed here are corrected for dead time and the value in brackets is also corrected for differences in the radial acceptance. $N_{\gamma,\mathrm{corr}}$ denotes the excess counts $\mathrm{N}_\gamma$ scaled by the ratio of the acceptance-corrected live time to that of the extraction region with 46.8 hr.

| Position | Coordinates | $\mathrm{N}_{\mathrm{ON}}$ | $\mathrm{N}_{\mathrm{OFF}}$ | $\alpha^{-1}$ | Live time [hr] | $\mathrm{N}_\gamma$ | S [$\sigma$] | $\mathrm{N}_{\gamma,\mathrm{corr}}$ |
|---|---|---|---|---|---|---|---|---|
| 1 | (31°55′43″), (−0°12′45″) | 2051 | 27717 | 14.49 | 78.1 (44.3) | 138.8 | 3.0 | 146.6 |
| 2 | (31°43′13.1″), (−0°28′44.8″) | 2016 | 27815 | 14.51 | 81.6 (44.9) | 99.7 | 2.2 | 103.9 |
| 3 | (31°25′43″), (−0°40′14.9″) | 1825 | 24811 | 14.35 | 79.5 (38.8) | 96.4 | 2.5 | 116.3 |
| 4 | (31°5′12.8″), (−0°45′45″) | 1716 | 22776 | 14.01 | 81.7 (37.8) | 90.6 | 2.1 | 112.2 |
| 5 | (30°43′43″), (−0°44′15″) | 1616 | 19294 | 13.3 | 80.3 (34.0) | 165.2 | 4.1 | 227.4 |
| 6 | (30°24′19.8″), (−0°33′47.5″) | 1369 | 17357 | 14.29 | 76.8 (28.3) | 154.8 | 4.2 | 256.0 |
| 7 | (30°13′19.2″), (−0°13′48″) | 1755 | 17941 | 12.86 | 81.7 (32.5) | 360.2 | 8.9 | 518.7 |
| 8 | (30°18′13.3″), (0°7′14.9″) | 1724 | 20104 | 13.39 | 82.6 (34.2) | 222.4 | 5.4 | 304.3 |
| 9 | (30°31′43″), (0°23′44.9″) | 1505 | 22152 | 15.24 | 79.8 (33.9) | 51.0 | 1.3 | 70.4 |
| 10 | (30°51′31″), (0°33′15.1″) | 1667 | 23838 | 14.87 | 79.4 (35.3) | 63.7 | 1.5 | 84.5 |
| 11 | (31°10′12.7″), (0°38′15″) | 1841 | 24125 | 14.34 | 79.9 (39.1) | 159.0 | 3.7 | 190.3 |
| 12 | (31°29′43.1″), (0°35′15″) | 1889 | 25101 | 13.91 | 79.9 (42.5) | 84.2 | 1.9 | 92.7 |
| 13 | (31°47′43.1″), (0°26′15″) | 1914 | 27478 | 14.91 | 77.2 (42.4) | 70.6 | 169 | 77.9 |

Considering $\bar{N_\gamma} = 148.5$ obtained from the test regions, 186.0 excess counts out of the 334.5 observed ones in the extraction region should originate from the 3C391 region using the estimation with the test regions. This corresponds to a fraction of 55.6%, which is lower than the one derived from the morphological model with almost 70%. One reason is that the underlying large-scale emission is not considered in the simple morphological model with two sources. In the approach using the test regions it is not possible to separate the emission due to the adjacent source from the large-scale emission. Therefore, the number of excess originating from HESS J1848–018 is overestimated due to the latitude-dependent large-scale component. The excess within the test regions from the large-scale component is underestimated, because the test regions have different latitudes and therefore the regions at larger latitude contain less excess from the large-scale component. Table 7.4 summarises the measured excess counts and the corrected excess counts obtained using the morphological model and the test- region method.

**Table 7.4:** Event statistics for the circular extraction region centred at $(31°58'13.2'', 0°8'15'')$ with a radius of 0.16°. $N_{\mathrm{ON}}$ denotes the number of $\gamma$-ray like events within the extraction region, $N_{\mathrm{OFF}}$ the number of $\gamma$-ray like events within the OFF regions. The ratio between the ON and OFF area is given by $\alpha$. The number of excess counts after background substraction is given by $N_\gamma$ and $S$ is the significance of those excess counts.

| | $N_{\mathrm{ON}}$ | $N_{\mathrm{OFF}}$ | $\alpha$ | $N_\gamma$ | S $[\sigma]$ |
|---|---|---|---|---|---|
| observed | 2314 | 27293 | 0.0725 | 334.5 | 7.1 |
| corrected (morphology model) | | | | 233.5 | |
| corrected (using test regions) | | | | 186.0 | |

The extraction region at (l,b)=$(31°58'13.2'', 0°8'15'')$ with a radius of 0.16° was selected to estimate the spectral properties of the observed emission around the supernova remnant 3C391. Using a power-law model and fitting between 250 GeV and 10 TeV leads to the following spectral properties for the $\gamma$-ray emission within the extraction region:

- Flux normalisation at 1.2 TeV : $(2.35 \pm 0.35) \cdot 10^{-13}\,\mathrm{TeV}^{-1}\mathrm{cm}^{-2}\mathrm{s}^{-1}$;
- Spectral index $\Gamma$: $2.20 \pm 0.18$;
- Differential flux at 1 TeV: $(3.16 \pm 0.53) \cdot 10^{-13}\,\mathrm{TeV}^{-1}\mathrm{cm}^{-2}\mathrm{s}^{-1}$;
- Integral flux above 1 TeV: $(2.89 \pm 0.55) \cdot 10^{-13}\,\mathrm{cm}^{-2}\mathrm{s}^{-1}$.

It is important to keep in mind when interpreting these spectral properties that the excess within the extraction region is influenced by the nearby source HESS J1848–018 as well as by the underlying large-scale emission. This potentially affects not only the flux normalisation but also the spectral index.

## 7.3 Testing the supernova remnant/molecular cloud scenario

Significant $\gamma$-ray emission is observed in the vicinity of the supernova remnant 3C391. The remnant is known to interact with a nearby molecular cloud. The remnant itself as well as the ambient cloud could be sources of the observed emission. Pulsar wind nebulae, however, are the most frequent counterparts to $\gamma$-ray emission located in the Galactic plane. Therefore, it is necessary to include them in the discussion as potential counterparts for the observed emission. Two nearby pulsars, PSR J1848-0055 and PSR J1849-0040, are listed in the ATNF catalogue[7]. PSR J1848-0055 has a spin-down luminosity[8] of $\dot{E} = 2.57 \cdot 10^{33}\,\mathrm{erg\,s^{-1}}$ and is located at a distance of 15.1 kpc (Manchester et al., 2005). PSR J1849-0040 has an $\dot{E} = 1.41 \cdot 10^{33}\,\mathrm{erg\,s^{-1}}$ and a distance of 20.9 kpc (Manchester et al., 2005). The low spin-down luminosities, large distances and the resulting low ratio $\dot{E}/d^2$ of $1.1 \cdot 10^{31}\,\mathrm{erg\,s^{-1}\,kpc^{-2}}$ for PSR J1848-0055, respectively $3.3 \cdot 10^{30}\,\mathrm{erg\,s^{-1}\,kpc^{-2}}$ for PSR J1849-0040, make these two pulsars unlikely counterparts for the observed emission (Carrigan et al., 2008). Apart from pulsar wind nebulae also X-ray binaries and star forming regions are counterpart candidates, but none of these are catalogued near the 3C391 region. Hence, in the following the discussion focuses on the supernova remnant/molecular cloud scenario to explain the emission.

The supernova remnant 3C391 is located at the edge of a molecular cloud complex at velocities $90 - 110\,\mathrm{km\,s^{-1}}$, revealed by CO observations (Wilner et al., 1998). Furthermore, detection of compact OH emission indicates the interaction of the shock of a supernova remnant with the cloud (Frail et al., 1996; Hewitt et al., 2008). Such compact OH emission is found at velocities of $\approx 97\,\mathrm{km\,s^{-1}}$, $\approx 105\,\mathrm{km\,s^{-1}}$ and $\approx 110\,\mathrm{km\,s^{-1}}$. The observed TeV emission near 3C391 is located at the nearby molecular cloud complex. The analysis of radio data presented here uses $^{13}$CO data from the Galactic Ring Survey (Jackson et al., 2006). Figure 7.7(a) shows the velocity spectrum of $^{13}$CO emission within the TeV analysis position. Figure 7.7(b) shows a sky map of the $^{13}$CO emission integrated between $87\,\mathrm{km\,s^{-1}}$ and $117\,\mathrm{km\,s^{-1}}$. The green dashed circle indicates the extraction region for the TeV spectral analysis, the white solid circle represents the radio position and extension of 3C391 and the two yellow crosses mark the positions of the OH maser emission. The $\gamma$-ray excess near the remnant 3C391 is spatially coincident with dense molecular material as shown in Fig. 7.8. The $\gamma$-ray excess map is overlaid with the 4, 8 and $12\,\mathrm{K\,km\,s^{-1}}$ $^{13}$CO contours for the emission integrated between $87\,\mathrm{km\,s^{-1}}$ and $117\,\mathrm{km\,s^{-1}}$.

The simple test for spatial coincidence of the observed emission with the molecular cloud complex is not sufficient to establish the supernova remnant/molecular cloud association as counter part. It is necessary to test if the spectral properties of such a scenario match the observed spectral properties. As discussed in Section 7.2 the emission around 3C391 is influenced by the neighbouring source HESS J1848–018 and a large-scale diffuse emission component, but it is at least possible to test if the scenario with a supernova remnant and a molecular cloud could deliver the measured integral flux.

For this estimation it is necessary to derive the distance between the remnant 3C391 and the molecular cloud as well as the cloud mass. Table 7.5 lists the velocities $V_{\mathrm{LSR}}$, distances $d_{\mathrm{MC}}$ and masses $M_{\mathrm{MC}}$ for nearby molecular clouds from the Galactic Ring Survey (Roman-Duval

[7] http://www.atnf.csiro.au/research/pulsar/psrcat/

[8] The rotation of the pulsar is decreasing with time and a fraction of this energy is converted to luminous energy.

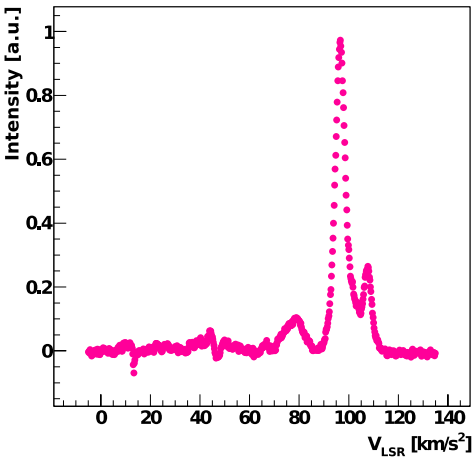


(a) Velocity spectrum of $^{13}$CO emission within the TeV extraction region for spectral analysis.

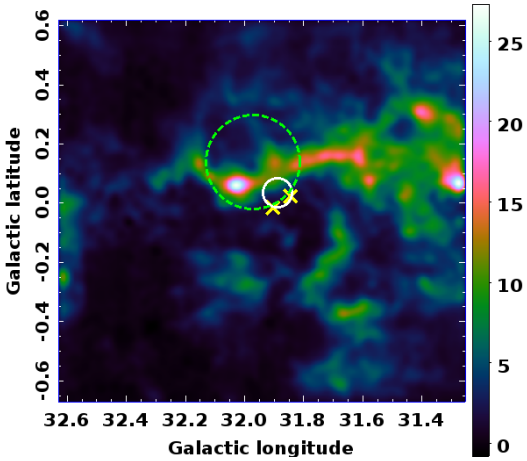


(b) $^{13}$CO emission in units of [K km s$^{-1}$] integrated over velocities between 87 km s$^{-1}$ and 117 km s$^{-1}$. The extraction region for the TeV analysis is marked by the green dashed circle.

**Figure 7.7:** $^{13}$CO emission in the region of the supernova remnant 3C391. The radio position and extent of the supernova remnant 3C391 is marked by the white circle and the OH emission spots by the yellow crosses.

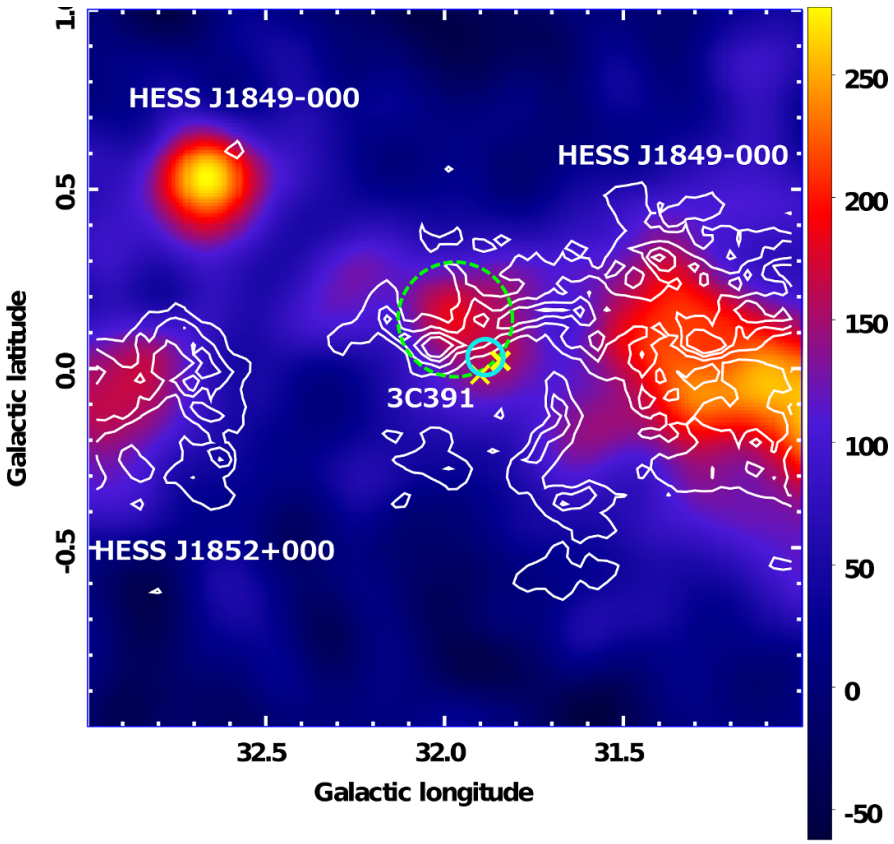


**Figure 7.8:** $\gamma$-ray excess map overlaid with the $^{13}$CO contours (4, 8 and 12 K km s$^{-1}$) of the emission integrated between 87 km s$^{-1}$ and 117 km s$^{-1}$. The position of the supernova remnant 3C391 is marked by the cyan circle and the OH emission spots by the yellow crosses.

et al., 2009, 2010) that have their peak emission located between 31.5° and 32.5° Galactic longitude with velocities between 87 km s$^{-1}$ and 117 km s$^{-1}$.

**Table 7.5:** Molecular clouds from the Galactic Ring Survey (GRS) with their peak emission located between 31.5° and 32.5° Galactic longitude with velocities between 87 km s$^{-1}$ and 117 km s$^{-1}$.

| GRS cloud | $V_{\mathrm{LSR}}$ [km s$^{-1}$] | $d_{\mathrm{MC}}$ [kpc] | $M_{\mathrm{MC}}$ [$M_\odot$] |
|---|---|---|---|
| G031.74-00.36 | 88.8 | 8.65 | $(4.70 \pm 0.24) \cdot 10^3$ |
| G032.04-00.21 | 96.4 | 6.85 | $(3.23 \pm 0.27) \cdot 10^4$ |
| G032.09+00.09 | 96.8 | 7.07 | $(1.42 \pm 0.15) \cdot 10^5$ |
| G031.64-00.36 | 100.7 | 7.20 | $(8.89 \pm 0.88) \cdot 10^4$ |
| G031.69-00.16 | 104.1 | 7.22 | $(4.66 \pm 0.41) \cdot 10^4$ |
| G031.79+00.14 | 107.5 | 7.20 | $(4.43 \pm 0.39) \cdot 10^4$ |
| G031.59+00.24 | 116.4 | 7.25 | $(3.43 \pm 0.16) \cdot 10^3$ |

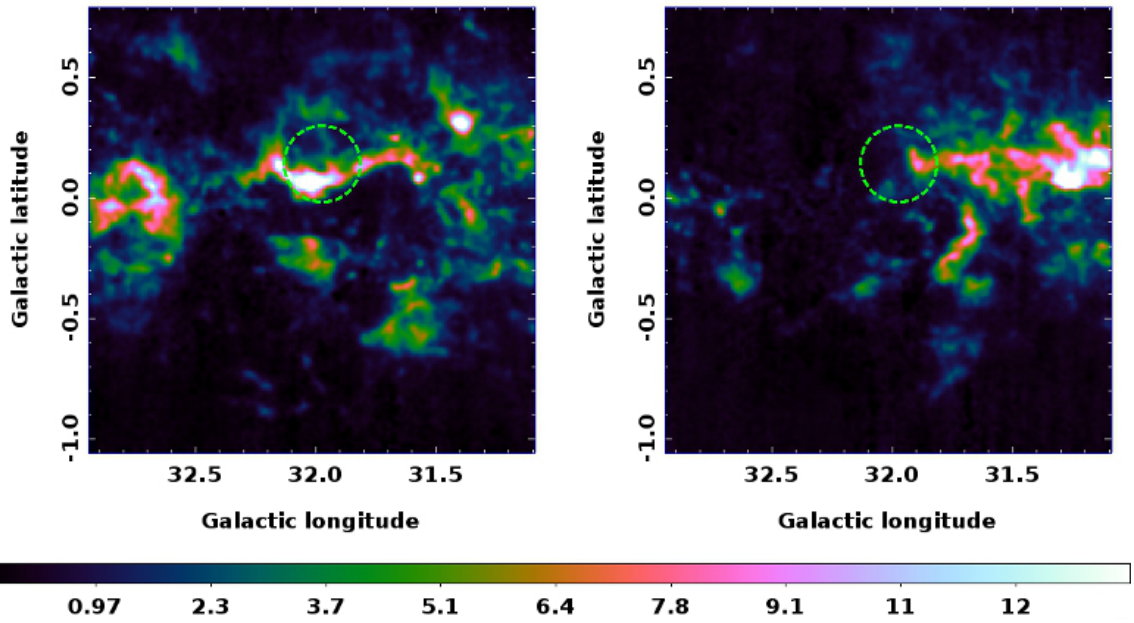


**Figure 7.9:** $^{13}$CO emission in units of [K km s$^{-1}$] integrated over velocities between 90 km s$^{-1}$ and 100 km s$^{-1}$ (left) and 100 km s$^{-1}$ and 115 km s$^{-1}$ (right). The green dashed circle represents the extraction region used for the spectral analysis of the H.E.S.S. data.

The largest fraction of CO emission within the extraction region used in the analysis of the H.E.S.S. data comes from the cloud G032.09+00.09. The clouds G031.74-00.36, G032.04-00.21, G031.64-00.36 and G031.59+00.24 do not overlap with the analysis position. The comparison of the integrated CO emission between 90 km s$^{-1}$ and 100 km s$^{-1}$ and the emission between 100 km s$^{-1}$ and 115 km s$^{-1}$, as shown on Fig. 7.9, with the molecular clouds listed in Tab. 7.5 reveals that cloud G032.09+00.09 at a velocity of 97 km s$^{-1}$ is preferred over G031.69-00.16 and G031.79+00.14, since these both clouds have velocities larger than 100 km s$^{-1}$.

It is possible to test with a parameter scan for the supernova remnant 3C391 and the molecular cloud G032.09+00.09 under the same conditions as in Section 6.2 what level of $\gamma$-ray flux results from this scenario. A supernova explosion energy of $10^{51}$ erg used in the parameter scan

is compatible with the value of $\sim (0.3-1.4)\cdot 10^{51}$ erg derived from X-ray observations (Chen et al., 2004). Figure 7.10(a) shows the distribution of the integrated fluxes for the tested parameter sets. This distribution is truncated at $\log_{10}(I(>1\,\mathrm{TeV})/\mathrm{cm}^{-2}\mathrm{s}^{-1}) > -14.5$ to focus on the relevant range. Figure 7.10(b) shows that the observed flux of $(2.89\pm0.55)\cdot 10^{-13}\,\mathrm{cm}^{-2}\mathrm{s}^{-1}$ can be realised for distances from the 3C391 to the molecular cloud between 20 pc and 100 pc, depending on the diffusion coefficient. Reducing $\eta$, the fraction of energy from the supernova explosion for the acceleration of cosmic rays, from 0.3 to a lower value of 0.1 still gives viable parameter sets for $d_{\text{SNR-MC}} = (40-70)\,\mathrm{pc}$ and diffusion coefficients of $10^{26}\,\mathrm{cm}^2\,\mathrm{s}^{-1}$ and $10^{27}\,\mathrm{cm}^2\,\mathrm{s}^{-1}$.

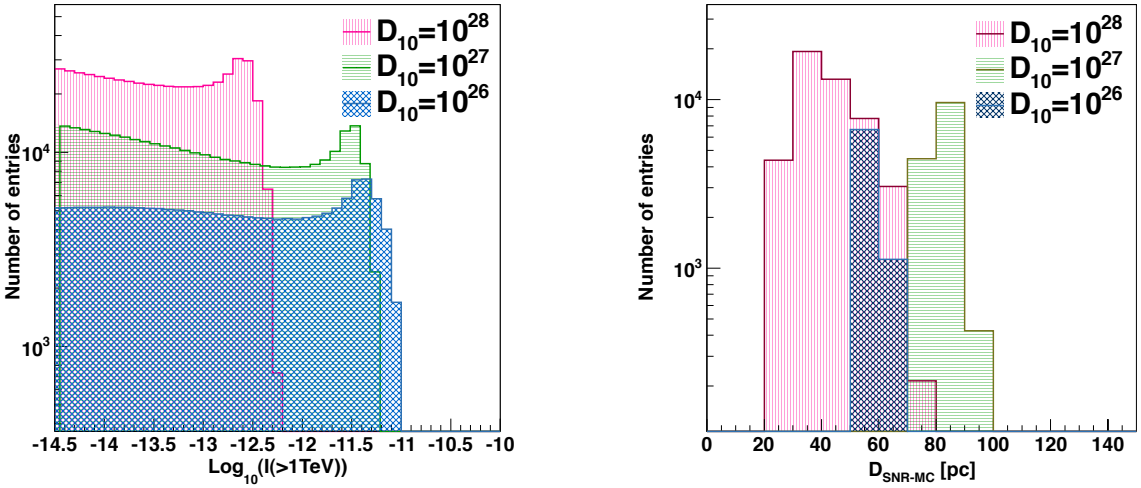


(a) Distribution of integral fluxes above 1 TeV obtained with a parameter scan. The range of the flux was truncated at $\log_{10}(I(>1\,\mathrm{TeV})/\mathrm{cm}^{-2}\mathrm{s}^{-1}) > -14.5$.

(b) The distance of tested parameter sets that give an integral flux above 1 TeV within the range $(2.9\pm0.55)\cdot 10^{-13}\,\mathrm{cm}^{-2}\mathrm{s}^{-1}$ for different diffusion coefficients.

**Figure 7.10:** Parameter scan with the same conditions as in Section 6.2 for the supernova remnant 3C391 and the molecular cloud G032.09+00.09.

## 7.4 Conclusion

This Chapter presented a analysis of data from the H.E.S.S. experiment of the region around the supernova remnant 3C391, one of those regions, that were revealed by the search for potentially detectable molecular clouds carried out in this work. Significant $\gamma$-ray emission was discovered spatially coincident with a molecular cloud near the remnant. It remains difficult to establish the ambient molecular cloud of the supernova remnant 3C391 as source of the observed $\gamma$-ray emission because of the neighbouring source HESS J1848–018 and the large-scale diffuse component. Futhermore, the spectral properties of the TeV $\gamma$-ray emission derived within the extraction region are affected by the underlying diffuse large-scale emission and potentially by HESS J1848–018. A detailed analysis of the large-scale diffusion component, however, is beyond the scope of this work. But, nevertheless, the supernova remnant/molecular cloud scenario is plausible given the spatial correlation of the $\gamma$-ray emission with the ambient cloud complex. This scenario can easily reproduce the

integrated flux measured at the analysis position which includes potential contamination. Observations with the future experiment CTA observatory with better sensitivity and angular resolution are mandatory to possibly seperate the generated flux of the molecular cloud from the underlying large-scale diffuse component.

CHAPTER 8

# Summary and outlook

Molecular clouds near supernova remnants as sources of very-high-energy $\gamma$-ray emission have been studied systematically in this thesis. For this purpose the information about molecular clouds of the Galactic Ring Survey and selected supernova remnants of the catalogue of Ferrand & Safi-Harb (2012) were combined with the information about very-high-energy $\gamma$-ray emission from the H.E.S.S. Galactic Plane Survey (Carrigan et al., 2013). The H.E.S.S. experiment provides the largest connected data set of the inner Galactic plane with the H.E.S.S. Galactic Plane Survey, which is very well suited for population studies. The catalogue of clouds identified in the Galactic Ring Survey is the most comprehensive one containing clouds with determined distances and masses (Rathborne et al., 2009; Roman-Duval et al., 2009, 2010).
Supernova remnants are assumed to be sources of cosmic-rays and detections of supernova remnants in the TeV energy band revealed high-energy particles at these locations. Generally, the observed $\gamma$-ray emission can be produced by both, leptons and hadrons. Molecular clouds near supernova remnants provide a suitable environment to study the acceleration of hadrons in supernova remnants, as $\gamma$-ray emission observed from molecular clouds mainly originates from proton-proton interaction and subsequent neutral pion decay. Apart from the general study of hadronic $\gamma$-ray emission, molecular clouds near supernova remnants allow to derive constraints of the propagation properties of high-energy particles through the interstellar medium.
The study of $\gamma$-ray emitting molecular clouds presented in this thesis explored various aspects: the spatial coincidence of molecular clouds with very-high-energy $\gamma$-ray emission, regions around supernova remnants populated with potentially detectable $\gamma$-ray emitting molecular clouds, constraints on the diffusion properties of high-energy particles and a closer look in the TeV energy range at the region around a specific supernova remnant, namely the supernova remnant 3C391.

In Chapter 5 the first analysis of spatial coincidence for a whole population of molecular clouds with regions of $\gamma$-ray emission from the H.E.S.S. Galactic Plane Survey was presented. The spatial coincidence of molecular clouds identified in the Galactic Ring Survey with TeV $\gamma$-ray emission observed in the H.E.S.S. Galactic Plane Survey was tested using $\gamma$-ray

significance sky maps by Carrigan et al. (2013) with different correlation radii of 0.2°, 0.3° and 0.4°. The $\gamma$-ray peak significance within the area of a cloud has to be larger than $7.5\,\sigma$ to fulfill the, here defined, coincidence criterion. It has been demonstrated that most molecular clouds of the Galactic Ring Survey are only spatially coincident with $\gamma$-ray emission by chance. However, for molecular clouds with $3.5 < \log_{10}[(M_{\mathrm{MC}}/d_{\mathrm{MC}}^2)/(\mathrm{M}_\odot/\mathrm{kpc}^2)] < 4$, where $M_{\mathrm{MC}}$ is the mass of the cloud and $d_{\mathrm{MC}}$ its distance, a larger fraction of spatially coincident molecular clouds than expected from random coincidences derived with simulated populations of molecular clouds has been found. The probability that the observed fraction of spatially coincident clouds in this range is caused by random coincidences is $3.9 \cdot 10^{-3}$, $5.1 \cdot 10^{-4}$ and $4.5 \cdot 10^{-4}$ for the tests with significance maps with correlation radii of 0.2°, 0.3° and 0.4°, respectively. Thus, the observed enhancement can merely be interpreted as a hint for a connection between molecular clouds of the Galactic Ring Survey in this $M_{\mathrm{MC}}/d_{\mathrm{MC}}^2$ range and extended $\gamma$-ray emission in the H.E.S.S. Galactic Plane Survey. The analysis presented here suggests that 15 % of the 104 molecular clouds with $3.5 < \log_{10}[(M_{\mathrm{MC}}/d_{\mathrm{MC}}^2)/(\mathrm{M}_\odot/\mathrm{kpc}^2)] < 4$ might be connected to $\gamma$-ray emission. However, to achieve a significant result it would be necessary to reduce the level of random coincidences to be less than 10 %. The hint for a relation between the molecular clouds and $\gamma$-ray emission can not be explained by the emission of molecular clouds only embedded in the cosmic-ray sea, even considering the total flux of all molecular clouds located at the same line-of-sight. Hence, the results derived in this thesis point towards $\gamma$-ray emission of molecular clouds near supernova remnants. It will be interesting to test the relation between molecular clouds and $\gamma$-ray emission with the forthcoming source catalogue (H.E.S.S. Collaboration et al., 2014c) of the H.E.S.S. Galactic Plane Survey using the additional information provided there to define a stricter coincidence criterion. But it will remain challenging to decrease the level of random coincidences below 10 % for extended objects such as molecular clouds.

Supernova remnants are prime candidates to be cosmic-ray sources, hence, Chapter 6 focused on the scenario of molecular clouds near supernova remnants. The parameter space of $\gamma$-ray emitting clouds near supernova remnants detectable with H.E.S.S. was derived using the theoretical model of Gabici et al. (2009) for the estimation of the expected $\gamma$-ray flux. The sensitivity of the H.E.S.S. Galactic Plane Survey allows to detect $\gamma$-ray emission from molecular clouds up to 100 pc away from the supernova remnant. In this thesis, the first search for regions populated with potentially detectable molecular clouds within the H.E.S.S. Galactic Plane Survey was carried out using the molecular clouds from the Galactic Ring Survey together with supernova remnants selected from the catalogue by Ferrand & Safi-Harb (2012), the theoretical model of for the expected $\gamma$-ray flux and information about the flux sensitivity of the H.E.S.S. Galactic Plane Survey. The uncertanties on many parameters have been considered using a parameter scan for the calculation of the $\gamma$-flux for each supernova remnant/molecular cloud pair. The presentation of the results was chosen to highlight regions with either more than one potentially detectable cloud or regions with supernova remnants with well estimated properties.

Apart from the search for regions with potentially detectable clouds, the clouds of the Galactic Ring Survey have been used for the first time to derive constraints on the diffusion properties of high-energy particles from a population of molecular clouds. Using these clouds, simulated populations of supernova remnants provided by Hahn (2014) and supernova remnant/molecular cloud associations identified in the TeV energy band, a constraint on the average normalisation of the diffusion coefficient at 10 GeV to be smaller than $10^{28}\,\mathrm{cm}^2\,\mathrm{s}^{-1}$ for dense regions near supernova remnants was obtained. The energy dependence of the

diffusion coefficient is, however, not constrainable with the presented strategy and it will remain challenging also for the future CTA observatory. This is the first study to obtain constraints on the diffusion properties combining a molecular cloud population, simulated supernova remnants, the sensitivity of the H.E.S.S. Galactic Plane Survey and identified TeV sources.

One region that was highlighted by the search for regions populated with potentially detectable $\gamma$-ray emitting molecular clouds, presented in Chapter 6, is the region around the supernova remnant 3C391. The analysis of about 80 hrs of observation with the H.E.S.S. experiment revealed significant TeV emission in that region. The morphological and spectral properties of this emission were obtained and discussed. The emission scenario of a molecular cloud near this supernova remnant was explored. This scenario can easily achieve the measured flux and the $\gamma$-ray emission is spatially coincident with a molecular cloud of the Galactic Ring Survey. It is, however, not possible to establish the observed emission as supernova remnant/molecular cloud association due to the spectral uncertanties because of the underlying large-scale diffuse $\gamma$-ray emission and the adjacent source HESS J1848–018. Observation with the CTA observatory with better angular resolution and better sensitivity can possibly separate the emission components and confirm a supernova remnant/molecular cloud association in the 3C391 region.

This thesis presented results obtained with the data set of the H.E.S.S. Galactic Plane Survey combined with a public catalogue of molecular clouds and selected supernova remnants. This work was restricted to the region covered by the Galactic Ring Survey, as it is the most comprehensive molecular cloud catalogue so far. Combining the molecular cloud sample with the forthcoming catalogue of the Mopra Southern Galactic Plane CO Survey (Burton et al., 2013) will increase the explorable region for $\gamma$-ray emitting molecular clouds within the H.E.S.S. Galactic Plane Survey. The search for potentially detectable molecular clouds was limited by both the region covered by the molecular cloud catalogue and the number of supernova remnants with determined ages and distances. This search can be extended with more supernova remnants fulfilling the criterion. Therefore, many of the results derived with the methods as presented in this thesis are expected to improve not only by observations with the forthcoming CTA observatory with a better flux sensitivity and angular resolution, but also with a larger sample of supernova remnants and molecular clouds with determined properties.

APPENDIX A

# Selection of the exclusion regions for the analysis of H.E.S.S. observations of the 3C391 region

For the analysis of observations of the H.E.S.S. experiment of the region of the supernova remnant 3C391 presented in Chapter 7, so-called exclusion regions are needed for the background subtraction as explained in detail in Section 4.2.2. The area within the exclusion regions contains $\gamma$-ray sources and is, therefore, not used for the estimation of the background level within the analysis region. The strategy of Carrigan et al. (2012) is applied to avoid a manual selection of the exclusion regions. A $\gamma$-ray significance map is generated with a correlation radius of 0.22° without any regions excluded from the background subtraction. A circular region with a radius of 0.3° around each pixel of the significance sky map wich has a value larger than $5\,\sigma$ is marked as excluded region. These exclusion regions are used in the next generation of a significance map. The regions around pixels with a larger value of $5\,\sigma$ are again marked as the exclusion regions and the next significance sky map using the new exclusion regions is produced. This procedure is repeated until the exclusion regions do no longer change.
Figure A.1 shows the significance sky map of the region around the supernova remnant 3C391 on the right side and the distribution of the pixel significances on the left side. The position of the supernova remnant is marked by the black circle on the $\gamma$-ray significance sky map and the area within the red contour are the exclusion regions derived with the method described above. The distribution of the significance values for the pixels of the significance map is shown on the right side in Fig. A.1. The significance distribution of pixels outside of the exclusion region is coloured in red. A Gaussian function, $N(\sigma) \propto \exp(-(x-\mu)^2/(2\beta^2))$, is fitted to this distribution and the function with the derived parameters from the fit is shown by the dotted red line. The histogram in black shows the signifiance distribution of the whole skymap including the $\gamma$-ray sources in this sky region. The fit of the Gaussian function to the significance distribution of the area outside of the exclusion region gives $\mu = 0.089 \pm 0.003$ and $\beta = 1.302 \pm 0.002$. Apart from the rather large width of the Gaussian function with 1.3, a bump in the significance distribution, coloured in red, between $\approx 3\sigma$ and $5\sigma$ stands

out. This is mainly caused by the region in the sky arround the position of ≈ 34° Galactic longitude and ≈ 0.3° Galactic latitude. The peak signifcance in this area is 4.93 and, hence, slightly below the threshold of 5 $\sigma$. As a consequence a threshold of 4.5 $\sigma$ was applied and new exclusion regions were generated applying the method described above.

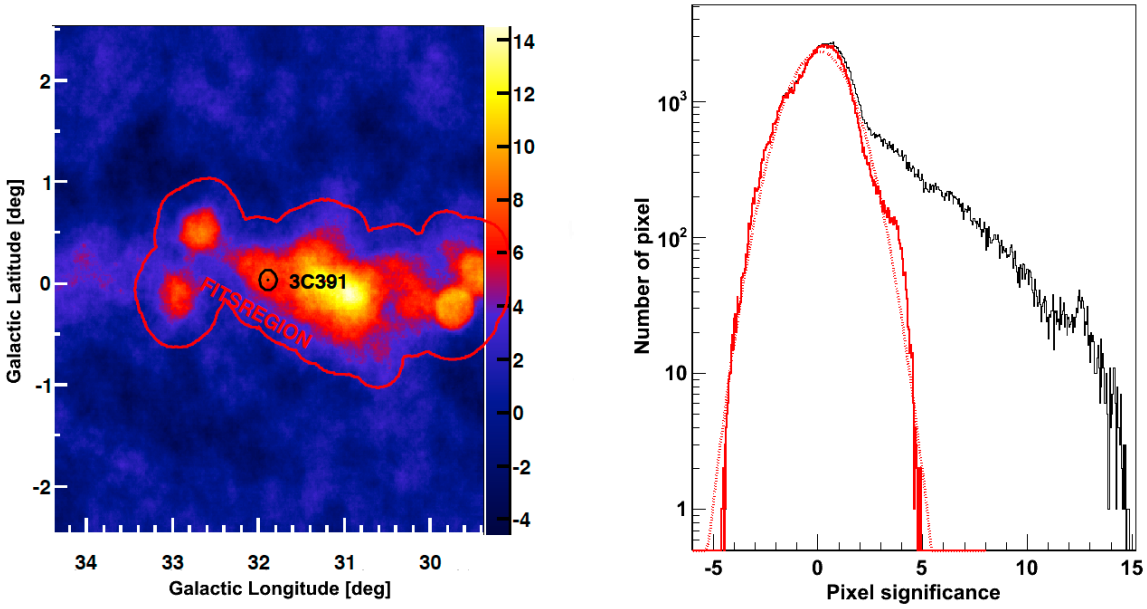


**Figure A.1:** $\gamma$-ray significance sky map of the 3C391 region and its significance distribution generated with the ringbackground method and a correlation radius of 0.22° using the exclusion regions generated with a threshold of 5$\sigma$.

**Table A.1:** Values derived from the fit of a Gaussian function to the distribution of the pixel significance values of a significance sky map outside of the exclusion region. The mean $\mu$ and the width $\beta$ of the Gaussian function derived from the fits are given for significance sky maps generated with a correlation radius of 0.1° and 0.22° using different exclusion regions.

| exclusion regions | $\mu$ | $\beta$ | Correlation radius [deg] |
|---|---|---|---|
| default | $-0.093 \pm 0.002$ | $1.029 \pm 0.002$ | 0.1 |
| default | $-0.230 \pm 0.003$ | $1.018 \pm 0.002$ | 0.22 |
| iterative: 5.0 $\sigma$ | $0.046 \pm 0.003$ | $1.112 \pm 0.002$ | 0.1 |
| iterative: 5.0 $\sigma$ | $0.089 \pm 0.003$ | $1.302 \pm 0.002$ | 0.22 |
| iterative: 4.5 $\sigma$ | $0.043 \pm 0.003$ | $1.075 \pm 0.002$ | 0.1 |
| iterative: 4.5 $\sigma$ | $0.110 \pm 0.003$ | $1.142 \pm 0.002$ | 0.22 |

For the comparison of the different exclusion regions a Gaussian function was fitted to the significance distribution of the sky map pixels outside of the exclusion regions. The values for the Gaussian function derived from the fit for the different exclusion regions derived with the iterative method and for the default exclusion regions from a H.E.S.S. internal database are listed in Tab. A.1. The distribution of significance values for a sky region without $\gamma$-ray sources and a perfect background subtraction applied is expected to have a mean $\mu$ of 0 $\sigma$ and a width $\beta$ of 1 $\sigma$. The values in Tab. A.1 show that the centre of the significance distribution outside of the exclusion regions is in general slightly shifted toward negativ

values for the default exclusion regions. The exclusion regions generated with a threshold of $5\,\sigma$ lead to significance distributions more centred toward $0\,\sigma$, but with a larger width $\beta$. Figure A.2 shows significance sky maps generated with a correlation radius of $0.22^\circ$ and different applied exclusion regions. The left sky map was generated using the default exclusion regions from a H.E.S.S. internal database, the right one was produced employing the exclusion regions selected with the iterative method and a threshold of $4.5\,\sigma$. The green contours indicate the corresponding exclusion regions for each sky map. The colour scale is the same for both maps. There are no large differences between the results derived with the different exclusion regions. Figure A.3 shows the $\gamma$-ray excess maps derived with the both selection of exclusion regions. The colour scale are again the same for both maps. There are, as well, no large differences for the excess observed in this region. The excess derived with the iteratively generated exclusion regions is in general slightly lower. The results presented in Chapter 7 are derived with the default exclusion regions, but the conclusions given there are also valid for an analysis using the exclusion regions derived with the iterative method with an threshold of $4.5\,\sigma$.

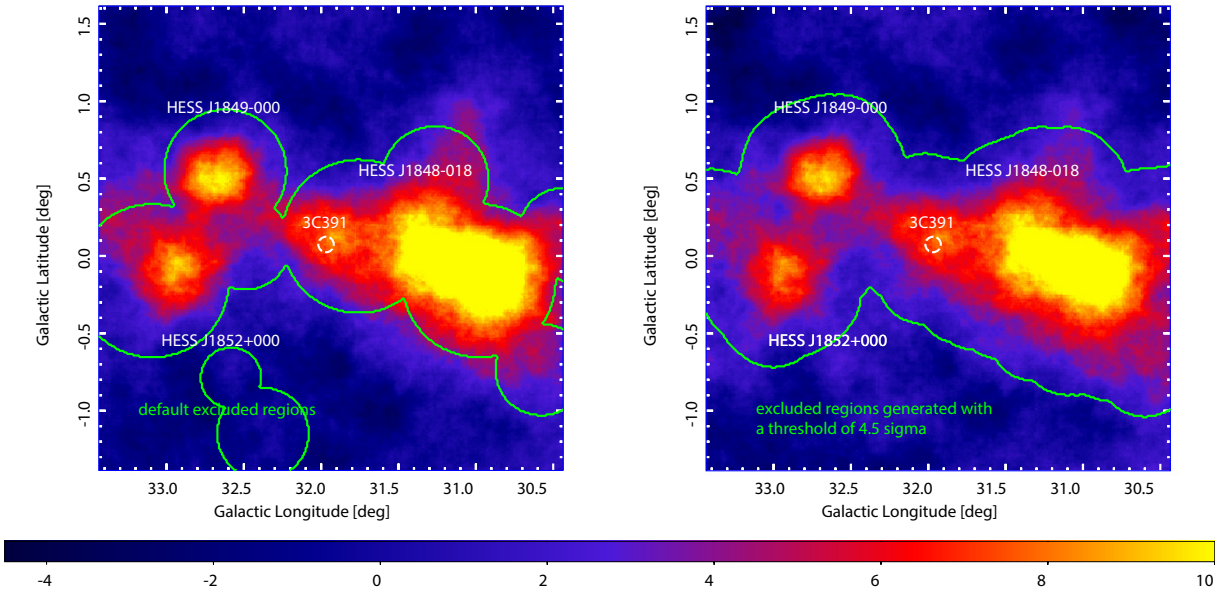


**Figure A.2:** $\gamma$-ray significance sky map of the 3C391 region produced with a correlation radius of 0.22° for different exclusion regions. Nearby H.E.S.S. sources and the radio position of the supernova remnant 3C391 are indicated in white. The contours of the exclusion regions are overlaid in green.
*Left*: Significance map generated using the default exclusion regions.
*Right*: Significance map with application of the the exclusion regions generated using the iterative method and an applied threshold of 4.5 $\sigma$.

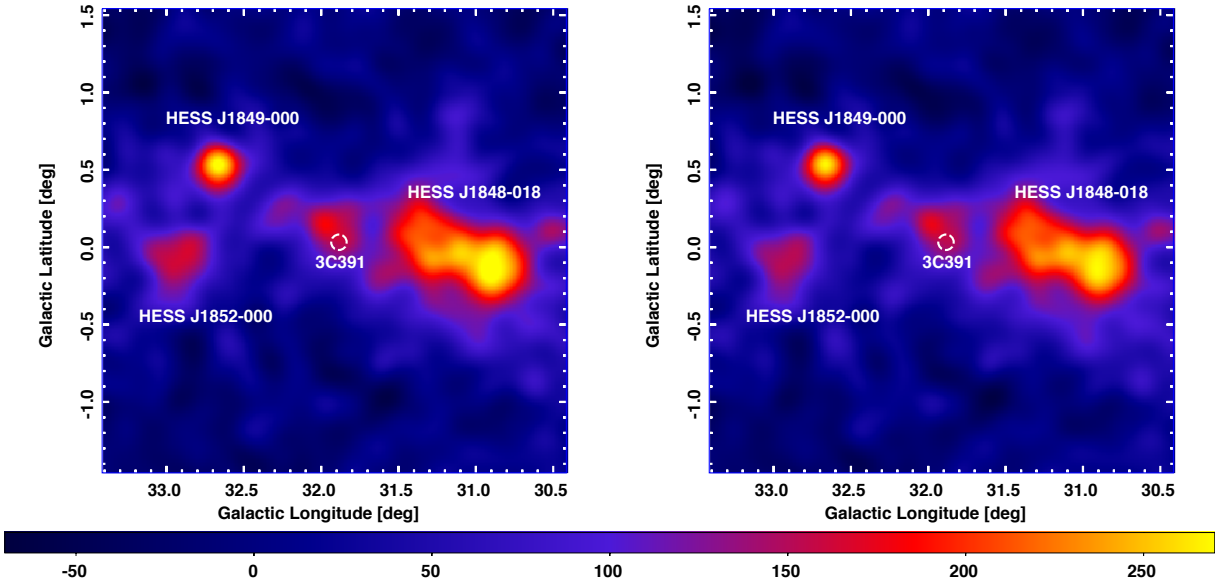


**Figure A.3:** TeV $\gamma$-ray excess map of 3C391 region produced with different exclusion regions. The sky maps are smoothed with a gaussian function with width 0.079°. Nearby H.E.S.S. sources and the radio position of the supernova remnant 3C391 are indicated in white.
*Left*: TeV $\gamma$-ray excess map generated using the default exclusion regions.
*Right*: TeV $\gamma$-ray excess map with application of the exclusion regions generated using the iterative method and an applied threshold of 4.5 $\sigma$.

# List of Figures

# List of Tables

# Bibliography


Abdo, A. A., Ackermann, M., Ajello, M., et al. *Fermi Large Area Telescope Observations of the Supernova Remnant W28 (G6.4-0.1)*. ApJ, 718:348–356, July 2010. doi:10.1088/0004-637X/718/1/348.

Abramowski, A., Acero, F., Aharonian, F., et al. *Very-high-energy gamma-ray emission from the direction of the Galactic globular cluster Terzan 5*. A&A, 531:L18, July 2011. arXiv:1106.4069. doi:10.1051/0004-6361/201117171.

Abramowski, A., Acero, F., Aharonian, F., et al. *Discovery of extended VHE $\gamma$-ray emission from the vicinity of the young massive stellar cluster Westerlund 1*. A&A, 537:A114, Jan. 2012. arXiv:1111.2043. doi:10.1051/0004-6361/201117928.

Ackermann, M., Ajello, M., Allafort, A., et al. *Detection of the Characteristic Pion-Decay Signature in Supernova Remnants*. Science, 339:807–811, Feb. 2013. arXiv:1302.3307. doi:10.1126/science.1231160.

Actis, M., Agnetta, G., Aharonian, F., et al. *Design concepts for the Cherenkov Telescope Array CTA: an advanced facility for ground-based high-energy gamma-ray astronomy*. Exp. Astron., 32:193–316, Dec. 2011. arXiv:1008.3703. doi:10.1007/s10686-011-9247-0.

Aharonian, F., Akhperjanian, A. G., Aye, K.-M., et al. *A New Population of Very High Energy Gamma-Ray Sources in the Milky Way*. Science, 307:1938–1942, Mar. 2005a. arXiv:astro-ph/0504380. doi:10.1126/science.1108643.

Aharonian, F., Akhperjanian, A. G., Barres de Almeida, U., et al. *Exploring a SNR/molecular cloud association within HESS J1745-303*. A&A, 483:509–517, May 2008a. arXiv:0803.2844. doi:10.1051/0004-6361:20079230.

Aharonian, F., Akhperjanian, A. G., Bazer-Bachi, A. R., et al. *Discovery of very high energy gamma-ray emission coincident with molecular clouds in the W 28 (G6.4-0.1) field*. A&A, 481:401–410, Apr. 2008b. arXiv:0801.3555. doi:10.1051/0004-6361:20077765.

Aharonian, F., Buckley, J., Kifune, T., & Sinnis, G. *High energy astrophysics with ground-based gamma ray detectors*. Rep. Prog. Phys, 71:096901, 2008.

Aharonian, F. et al. *Calibration of cameras of the H.E.S.S. detector*. Astropart. Phys., 22: 109–125, 2004. arXiv:astro-ph/0406658. doi:10.1016/j.astropartphys.2004.06.006.

Aharonian, F. et al. *Observations of the Crab Nebula with H.E.S.S.* Astron. Astrophys., 457: 899–915, 2006. arXiv:astro-ph/0607333. doi:10.1051/0004-6361:20065351.

Aharonian, F. A. *Very high and ultra-high-energy gamma-rays from giant molecular clouds*. Ap&SS, 180:305–320, June 1991. doi:10.1007/BF00648185.

Aharonian, F. A. *Gamma rays from supernova remnants*. Astropart. Phys., 43:71 – 80, 2013. ISSN 0927-6505. doi:http://dx.doi.org/10.1016/j.astropartphys.2012.08.007.

Aharonian, F. A., Drury, L. O., & Voelk, H. J. *GeV/TeV gamma-ray emission from dense molecular clouds overtaken by supernova shells*. A&A, 285:645–647, May 1994.

Aharonian, F. A., Akhperjanian, A. G., Bazer-Bachi, A. R., et al. *A possible association of the new VHE $\gamma$-ray source HESS J1825 137 with the pulsar wind nebula G 18.0 0.7*. A&A, 442: L25–L29, Nov. 2005b. arXiv:astro-ph/0510394. doi:10.1051/0004-6361:200500180.

Aloisio, R. & Blasi, P. *Propagation of galactic cosmic rays in the presence of self-generated turbulence*. JCAP, 7:001, July 2013. arXiv:1306.2018. doi:10.1088/1475-7516/2013/07/001.

Amano, T. & Hoshino, M. *Recent Progress in the Theory of Electron Injection in Collisionless Shocks*. In *Multi-scale Dynamical Processes in Space and Astrophysical Plasmas*, page 143, 2012. doi:10.1007/978-3-642-30442-2 16.

Anderson, C. D. *The Positive Electron*. Phys. Rev., 43:491–494, Mar 1933. doi:10.1103/PhysRev.43.491.

Anderson, C. D. & Neddermeyer, S. H. *Cloud Chamber Observations of Cosmic Rays at 4300 Meters Elevation and Near Sea-Level*. Phys. Rev., 50:263–271, Aug 1936. doi:10.1103/PhysRev.50.263.

Axford, W. I., Leer, E., & Skadron, G. *The Acceleration of Cosmic Rays by Shock Waves*. In *International Cosmic Ray Conference*, volume 11, page 132, 1977.

Baade, W. & Zwicky, F. *Cosmic Rays from Super-novae*. Proceedings of the National Academy of Science, 20:259–263, May 1934. doi:10.1073/pnas.20.5.259.

Barlow, R. *Statistics - A Guide to the Use of Statistical Methods in the Physical Sciences*. John Wiley and Sons, 1989. ISBN 0-471-92295-1.

Bell, A. R. *The acceleration of cosmic rays in shock fronts. I*. MNRAS, 182:147–156, 1978a.

Bell, A. R. *The acceleration of cosmic rays in shock fronts. II*. MNRAS, 182:443–455, 1978b.

Berge, D., Funk, S., & Hinton, J. *Background modelling in very-high-energy $\gamma$-ray astronomy*. A&A, 466:1219–1229, May 2007. arXiv:astro-ph/0610959. doi:10.1051/0004-6361:20066674.

Beringer, J. et al. *Review of Particle Physics (RPP)*. Phys.Rev.D, 86:010001, 2012. doi:10.1103/PhysRevD.86.010001.

Bernloehr, K. et al. *The optical system of the H.E.S.S. imaging atmospheric Cherenkov telescopes, Part I: layout and components of the system*. Astropart. Phys., 20:111–128, 2003. arXiv:astro-ph/0308246. doi:10.1016/S0927-6505(03)00171-3.

Bernlöhr, K., Barnacka, A., Becherini, Y., et al. *Monte Carlo design studies for the Cherenkov Telescope Array*. Astropart. Phys., 43:171–188, Mar. 2013. arXiv:1210.3503. doi:10.1016/j.astropartphys.2012.10.002.

Blandford, R. D. & Ostriker, J. P. *Particle acceleration by astrophysical shocks*. ApJ, 221: L29–L32, Apr. 1978. doi:10.1086/182658.

Blitz, L. & Thaddeus, P. *Giant molecular complexes and OB associations. I - The Rosette molecular complex*. ApJ, 241:676–696, Oct. 1980. doi:10.1086/158379.

Blumenthal, G. R. & Gould, R. J. *Bremsstrahlung, Synchrotron Radiation, and Compton Scattering of High-Energy Electrons Traversing Dilute Gases*. Rev. Mod. Phys, 42:237–271, 1970. doi:10.1103/RevModPhys.42.237.

Bolatto, A. D., Wolfire, M., & Leroy, A. K. *The CO-to-$H_2$ Conversion Factor*. ARA&A, 51: 207–268, Aug. 2013. arXiv:1301.3498. doi:10.1146/annurev-astro-082812-140944.

Bolz, S. *Absolute Energiekalibration der abbildenden Cherenkov-Teleskope des H.E.S.S. Experiments und Ergebnisse erster Beobachtungen des Supernova-Überrests RX J1713.7-3946*. PhD thesis, Ruprecht-Karls-Universität Heidelberg, 2004.

Brand, J. & Blitz, L. *The Velocity Field of the Outer Galaxy*. A&A, 275:67, Aug. 1993.

Burton, M. G., Braiding, C., Glueck, C., et al. *The Mopra Southern Galactic Plane CO Survey*. PASA, 30:e044, Aug. 2013. arXiv:1307.1027. doi:10.1017/pasa.2013.22.

Butkevich, A. G., Berdyugin, A. V., & Teerikorpi, P. *Statistical biases in stellar astronomy: the Malmquist bias revisited*. MNRAS, 362:321–330, Sept. 2005. doi:10.1111/j.1365-2966.2005.09306.x.

Caprioli, D., Kang, H., Vladimirov, A. E., & Jones, T. W. *Comparison of different methods for non-linear diffusive shock acceleration*. MNRAS, 407:1773–1783, Sept. 2010. arXiv:1005.2127. doi:10.1111/j.1365-2966.2010.17013.x.

Cardillo, M., Tavani, M., Giuliani, A., et al. *The supernova remnant W44: Confirmations and challenges for cosmic-ray acceleration*. A&A, 565:A74, May 2014. arXiv:1403.1250. doi:10.1051/0004-6361/201322685.

Carrigan, S., Hinton, J. A., Hofmann, W., & et al. *Establishing a connection between high-power pulsars and very-high-energy gamma-ray sources*. International Cosmic Ray Conference, 2: 659–662, 2008. arXiv:0709.4094.

Carrigan, S., Deil, C., & Gast, H. *New methods implemented in hap for the Galactic Plane Survey: Adaptive ring background method, Automatically generated exclusion maps, Flux maps*. H.E.S.S internal note, 2012.

Carrigan, S., Brun, F., Chaves, R. C. G., et al. *The H.E.S.S. Galactic Plane Survey - maps, source catalog and source population*. In Proceedings of the 33rd International Cosmic Ray Conference, July 2013. arXiv:1307.4690.

Casanova, S., Aharonian, F. A., Fukui, Y., et al. *Molecular Clouds as Cosmic-Ray Barometers*. PASJ, 62:769–777, June 2010. arXiv:0904.2887. doi:10.1093/pasj/62.3.769.

Castro, D. & Slane, P. *Fermi Large Area Telescope Observations of Supernova Remnants Interacting with Molecular Clouds*. ApJ, 717:372–378, July 2010. arXiv:1002.2738. doi:10.1088/0004-637X/717/1/372.

Chaves, R. C. G., Renaud, M., Lemoine-Goumard, M., & Goret, P. *HESS J1848-018: Discovery Of VHE $\gamma$-ray Emission From The Direction Of W 43*. volume 1085 of *American Institute of Physics Conference Series*, pages 372–375, Dec. 2008. doi:10.1063/1.3076684.

Chen, Y. & Slane, P. O. *ASCA Observations of the Thermal Composite Supernova Remnant 3C 391*. ApJ, 563:202–208, Dec. 2001. arXiv:astro-ph/0108502. doi:10.1086/323886.

Chen, Y., Su, Y., Slane, P. O., & Wang, Q. D. *A Chandra ACIS View of the Thermal Composite Supernova Remnant 3C 391*. ApJ, 616:885–894, Dec. 2004. arXiv:astro-ph/0408355. doi:10.1086/425152.

Clopper, C. J. & Pearson, E. S. *The use of confidecne or fiducial limits illustrated in the case of the binomial*. Biometrica, 26:404–413, Apr. 1934. doi:10.1093/biomet/26.4.404.

Combes, F., Encrenaz, P. J., Lucas, R., & Weliachew, L. *Observation of the CO Molecule in the Spiral Arms of External Galaxies*. A&A, 55:311, Mar. 1977.

Cornils, R. et al. *The optical system of the H.E.S.S. imaging atmospheric Cherenkov telescopes, Part II: mirror alignment and point spread function*. Astropart. Phys., 20:129–143, 2003. arXiv:astro-ph/0308247. doi:10.1016/S0927-6505(03)00172-5.

Crutcher, R. M. *Magnetic Fields in Molecular Clouds*. ARA&A, 50:29–63, Sept. 2012. doi:10.1146/annurev-astro-081811-125514.

Dame, T. M., Ungerechts, H., Cohen, R. S., et al. *A composite CO survey of the entire Milky Way*. ApJ, 322:706–720, Nov. 1987. doi:10.1086/165766.

Dame, T. M., Hartmann, D., & Thaddeus, P. *The Milky Way in Molecular Clouds: A New Complete CO Survey*. ApJ, 547:792–813, Feb. 2001. arXiv:astro-ph/0009217. doi:10.1086/318388.

Davies, J. & Cotton, E. *Design of the Quartermaster Solar Furnace*. Journal of Solar Energy Science and Engineering, 1:16–22, 1957.

de Naurois, M. H.E.S.S internal documentation, 2014.

de Naurois, M. & Rolland, L. *A stereoscopic semi-analytical model reconstruction of gamma-rays for Imaging Atmospheric Cherenkov Telescopes*. Astropart. Phys., 32:231, 2009. arXiv:0907.2610.

Deil, C., Stycz, K., Brun, F., et al. *HESS PSF and Morphology*. H.E.S.S internal documentation, 2014.

Dermer, C. D. *Secondary production of neutral pi-mesons and the diffuse galactic gamma radiation*. A&A, 157:223–229, Mar. 1986.

Drury, L. O. *An introduction to the theory of diffusive shock acceleration of energetic particles in tenuous plasmas*. Rep. Prog. Phys., 46:973–1027, Aug. 1983. doi:10.1088/0034-4885/46/8/002.

Dubus, G. *Gamma-ray binaries and related systems*. A&A Rev., 21:64, Aug. 2013. arXiv:1307.7083. doi:10.1007/s00159-013-0064-5.

Eddington, A. S. *On a formula for correcting statistics for the effects of a known error of observation*. MNRAS, 73:359–360, Mar. 1913.

Falgarone, E., Pety, J., & Hily-Blant, P. *Intermittency of interstellar turbulence: extreme velocity-shears and CO emission on milliparsec scale*. A&A, 507:355–368, Nov. 2009. arXiv:0910.1766. doi:10.1051/0004-6361/200810963.

Fermi, E. *On the Origin of the Cosmic Radiation*. Phys. Rev., 75:1169–1174, 1949.

Ferrand, G. & Safi-Harb, S. *A census of high-energy observations of Galactic supernova remnants*. Adv. Space Res., 49:1313–1319, May 2012. arXiv:1202.0245. doi:10.1016/j.asr.2012.02.004.

Frail, D. A., Goss, W. M., Reynoso, E. M., et al. *A Survey for OH (1720 MHz) Maser Emission Toward Supernova Remnants*. Astron. J, 111:1651, Apr. 1996. doi:10.1086/117904.

Freudenreich, H. T. *A COBE Model of the Galactic Bar and Disk*. ApJ, 492:495–510, Jan. 1998. arXiv:astro-ph/9707340. doi:10.1086/305065.

Fukui, Y. & Kawamura, A. *Molecular Clouds in Nearby Galaxies*. ARA&A, 48:547–580, Sept. 2010. doi:10.1146/annurev-astro-081309-130854.

Funk, S. et al. *The trigger system of the H.E.S.S. telescope array*. Astropart. Phys., 22:285–296, 2004. arXiv:astro-ph/0408375. doi:10.1016/j.astropartphys.2004.08.001.

Gabici, S., Aharonian, F. A., & Blasi, P. *Gamma rays from molecular clouds*. Ap&SS, 309: 365–371, June 2007. arXiv:astro-ph/0610032. doi:10.1007/s10509-007-9427-6.

Gabici, S., Aharonian, F. A., & Casanova, S. *Broad-band non-thermal emission from molecular clouds illuminated by cosmic rays from nearby supernova remnants*. MNRAS, 396:1629–1639, July 2009. arXiv:0901.4549. doi:10.1111/j.1365-2966.2009.14832.x.

Gabici, S., Casanova, S., Aharonian, F. A., & Rowell, G. *Constraints on the cosmic ray diffusion coefficient in the W28 region from gamma-ray observations*. In *SF2A-2010: Proceedings of the Annual meeting of the French Society of Astronomy and Astrophysics*, page 313, Dec. 2010.

Gaensler, B. M. & Slane, P. O. *The Evolution and Structure of Pulsar Wind Nebulae*. ARA&A, 44:17–47, Sept. 2006. arXiv:astro-ph/0601081. doi:10.1146/annurev.astro.44.051905.092528.

Giacinti, G., Kachelrieß, M., & Semikoz, D. V. *Filamentary Diffusion of Cosmic Rays on Small Scales*. Phys. Rev. Lett., 108(26):261101, June 2012. arXiv:1204.1271. doi:10.1103/PhysRevLett.108.261101.

Giuliani, A., Cardillo, M., Tavani, M., et al. *Neutral Pion Emission from Accelerated Protons in the Supernova Remnant W44*. ApJ, 742:L30, Dec. 2011. arXiv:1111.4868. doi:10.1088/2041-8205/742/2/L30.

Green, D. A. *A revised Galactic supernova remnant catalogue*. Bulletin of the Astronomical Society of India, 37:45–61, Mar. 2009. arXiv:0905.3699.

Green, D. A. *The distribution of SNRs with galactocentric radius*. volume 1505 of *American Institute of Physics Conference Series*, pages 5–12, Dec. 2012. doi:10.1063/1.4772214.

Häffner, S., Jung, I., & Stegmann, C. *Systematic search for gamma-ray emitting molecular clouds in the vicinity of supernova remnants*. In Proceedings of the 33rd International Cosmic Ray Conference, July 2013. arXiv:1307.5659.

Hahn, J. *Supernova Remnants with H.E.S.S.: Systematic analysis and population synthesis*. PhD thesis, Ruprecht-Karls-Universität Heidelberg, Germany, Jan. 2014.

Hanabata, Y., Katagiri, H., Hewitt, J. W., et al. *Detailed Investigation of the Gamma-Ray Emission in the Vicinity of SNR W28 with FERMI-LAT*. ApJ, 786:145, May 2014. arXiv:1403.6878. doi:10.1088/0004-637X/786/2/145.

Heitler, W. *Quantum Theory of Radiation*. Dover Press, third edition, 1954.

Helder, E. A., Vink, J., Bykov, A. M., et al. *Observational Signatures of Particle Acceleration in Supernova Remnants*. Space Sci. Rev., 173:369–431, Nov. 2012. arXiv:1206.1593. doi:10.1007/s11214-012-9919-8.

Hess, V. *Über Beobachtungen der durchdringenden Strahlung bei sieben Freiballonfahrten*. Physikalische Zeitschrift, 13:1084–1091, 1912.

H.E.S.S. collaboration. *Gamma Rays from W28 - an Old Supernova Remnant and Molecular Clouds*, Apr. 2007. URL `https://www.mpi-hd.mpg.de/hfm/HESS/pages/home/som/2007/04/`. visited on 10.07.2014.

H.E.S.S. collaboration. *At last - Supernova 1006*, Aug. 2008. URL `https://www.mpi-hd.mpg.de/hfm/HESS/pages/home/som/2008/08/`. visited on 10.07.2014.

H.E.S.S. Collaboration: A. Abramowski et al. *Diffuse gamma-Ray Emission From H.E.S.S. Galactic Plane Survey Observations*. n.a., 2014. to be published.

H.E.S.S. Collaboration et al. *Pulsar wind nebula population study*. n.a., 2014a. to be published.

H.E.S.S. Collaboration et al. *Supernova remnant population study*. n.a., 2014b. to be published.

H.E.S.S. Collaboration et al. *The H.E.S.S. source catalog*. n.a., 2014c. to be published.

Hewitt, J. W., Yusef-Zadeh, F., & Wardle, M. *A Survey of Hydroxyl toward Supernova Remnants: Evidence for Extended 1720 MHz Maser Emission*. ApJ, 683:189–206, Aug. 2008. arXiv:0802.3878. doi:10.1086/588652.

Hillas, A. M. *Cerenkov light images of EAS produced by primary gamma*. In F. C. Jones, editor, *International Cosmic Ray Conference*, volume 3, pages 445–448, 1985.

Hinton, J. A. & Hofmann, W. *Teraelectronvolt Astronomy*. ARA&A, 47:523–565, Sept. 2009. arXiv:1006.5210. doi:10.1146/annurev-astro-082708-101816.

Hofmann, W. *The H.E.S.S. Telescopes*, July 2012. URL `http://www.mpi-hd.mpg.de/hfm/HESS/pages/about/telescopes/`. visited on 14.01.2014.

Issa, M. R. & Wolfendale, A. W. *Gamma rays from the cosmic ray irradiation of local molecular clouds*. Nature, 292:430–433, Aug. 1981. doi:10.1038/292430a0.

Jackson, J. M., Rathborne, J. M., Shah, R. Y., et al. *The Boston University-Five College Radio Astronomy Observatory Galactic Ring Survey*. ApJS, 163:145–159, Mar. 2006. arXiv:astro-ph/0602160. doi:10.1086/500091.

Jiang, B., Chen, Y., Wang, J., et al. *Cavity of Molecular Gas Associated with Supernova Remnant 3C 397*. ApJ, 712:1147–1156, Apr. 2010. arXiv:1001.2204. doi:10.1088/0004-637X/712/2/1147.

Kelner, S. R., Aharonian, F. A., & Bugayov, V. V. *Energy spectra of gamma rays, electrons, and neutrinos produced at proton-proton interactions in the very high energy regime*. Phys. Rev. D, 74(3):034018, Aug. 2006. arXiv:astro-ph/0606058. doi:10.1103/PhysRevD.74.034018.

Kosack, K. & the H.E.S.S. Collaboration. *HESS J1852-000 near the supernova remnant Kes 78*, 2011. URL `http://www.mpi-hd.mpg.de/hfm/HESS/pages/home/som/2011/02/`. visited on 23.10.2013.

Krymskii, G. F. *A regular mechanism for accelerating charged particles at the shock front*. Akademiia Nauk SSSR Doklady, 234:1306–1308, 1977.

Kulsrud, R. M. *Plasma Physics for Astro Physics*. Princenton University Press, 2005.

Li, H. & Chen, Y. *$\gamma$-rays from molecular clouds illuminated by accumulated diffusive protons from supernova remnant W28*. MNRAS, 409:L35–L38, Nov. 2010. arXiv:1009.0894. doi:10.1111/j.1745-3933.2010.00944.x.

Li, T.-P. & Ma, Y.-Q. *Analysis methods for results in gamma-ray astronomy*. ApJ, 272:317–324, Sept. 1983. doi:10.1086/161295.

Li, W., Chornock, R., Leaman, J., et al. *Nearby supernova rates from the Lick Observatory Supernova Search - III. The rate-size relation, and the rates as a function of galaxy Hubble type and colour*. MNRAS, 412:1473–1507, Apr. 2011. arXiv:1006.4613. doi:10.1111/j.1365-2966.2011.18162.x.

Longair, M. S. *High Energy Astrophysics Vol. I*. Cambridge University Press, second edition, 1992.

Longair, M. S. *High Energy Astrophysics*. Cambridge University Press, third edition, 2011. ISBN 9780521756181.

Malkov, M. A. & O'C Drury, L. *Nonlinear theory of diffusive acceleration of particles by shock waves*. Rep. Prog. Phys., 64:429–481, Apr. 2001. doi:10.1088/0034-4885/64/4/201.

Manchester, R. N., Hobbs, G. B., Teoh, A., & Hobbs, M. *The Australia Telescope National Facility Pulsar Catalogue*. Astron. J, 129:1993–2006, Apr. 2005. arXiv:astro-ph/0412641. doi:10.1086/428488.

Montmerle, T. *On gamma-ray sources, supernova remnants, OB associations, and the origin of cosmic rays*. ApJ, 231:95–110, July 1979. doi:10.1086/157166.

Nava, L. & Gabici, S. *Anisotropic cosmic ray diffusion and gamma-ray production close to supernova remnants, with an application to W28*. MNRAS, 429:1643–1651, Feb. 2013. arXiv:1211.1668. doi:10.1093/mnras/sts450.

Nolan, P. L., Abdo, A. A., Ackermann, M., et al. *Fermi Large Area Telescope Second Source Catalog*. ApJS, 199:31, Apr. 2012. arXiv:1108.1435. doi:10.1088/0067-0049/199/2/31.

Obergaulinger, M., Iyudin, A. F., Müller, E., & Smoot, G. F. *Hydrodynamic simulations of the interaction of supernova shock waves with a clumpy environment: the case of the RX J0852.0-4622 (Vela Jr) supernova remnant*. MNRAS, 437:976–993, Jan. 2014. doi:10.1093/mnras/stt1966.

Ohira, Y., Murase, K., & Yamazaki, R. *Gamma-rays from molecular clouds illuminated by cosmic rays escaping from interacting supernova remnants*. MNRAS, 410:1577–1582, Jan. 2011. arXiv:1007.4869. doi:10.1111/j.1365-2966.2010.17539.x.

Ohm, S., van Eldik, C., & Egberts, K. *Gamma-Hadron Separation in Very-High-Energy gamma-ray astronomy using a multivariate analysis method*. Astropart. Phys., 31:383–391, 2009. arXiv:0904.1136. doi:10.1016/j.astropartphys.2009.04.001.

Padmanabhan, T. *Theoretical Astrophysics - Volume II: Stars and Stellar Systems*. Cambridge University Press, Camebridge, 2001.

Parzen, E. *On Estimation of a Probability Density Function and Mode*. The Annals of Mathematical Statistics, 33(3):1065–1076, 09 1962. doi:10.1214/aoms/1177704472.

Pedaletti, G., Torres, D. F., Gabici, S., et al. *On the potential of the Cherenkov Telescope Array for the study of cosmic-ray diffusion in molecular clouds*. A&A, 550:A123, Feb. 2013. arXiv:1301.5240. doi:10.1051/0004-6361/201220583.

Piron, F., Djannati-Atai, A., Punch, M., et al. *Temporal and spectral gamma-ray properties of <ASTROBJ>Mkn 421</ASTROBJ> above 250 GeV from CAT observations between 1996 and 2000*. A&A, 374:895–906, Aug. 2001. arXiv:astro-ph/0106196. doi:10.1051/0004-6361:20010798.

Ptuskin, V. *Propagation of galactic cosmic rays*. Astropart. Phys., 39:44–51, Dec. 2012. doi:10.1016/j.astropartphys.2011.11.004.

Radhakrishnan, V., Goss, W. M., Murray, J. D., & Brooks, J. W. *The Parkes Survey of 21-CENTIMETER Absorption in Discrete-Source Spectra. III. 21- Centimeter Absorption Measurements on 41 Galactic Sources North of Declination -48 degrees*. ApJS, 24:49, Jan. 1972. doi:10.1086/190249.

Rathborne, J. M., Johnson, A. M., Jackson, J. M., Shah, R. Y., & Simon, R. *Molecular Clouds and Clumps in the Boston University-Five College Radio Astronomy Observatory Galactic Ring Survey*. ApJS, 182(1):131, 2009.

Reach, W. T. & Rho, J. *Excitation and Disruption of a Giant Molecular Cloud by the Supernova Remnant 3C 391*. ApJ, 511:836–846, Feb. 1999. arXiv:astro-ph/9804142. doi:10.1086/306703.

Reimer, A. & Böttcher, M. *Studies of active galactic nuclei with CTA*. Astropart. Phys., 43: 103–111, Mar. 2013. arXiv:1208.5926. doi:10.1016/j.astropartphys.2012.05.011.

Reynolds, S. P. *Supernova Remnants at High Energy*. ARA&A, 46:89–126, Sept. 2008. doi:10.1146/annurev.astro.46.060407.145237.

Rho, J. & Petre, R. *Mixed-Morphology Supernova Remnants*. ApJ, 503:L167, Aug. 1998. doi:10.1086/311538.

Rho, J.-H. & Petre, R. *ROSAT PSPC Observation of the Supernova Remnant 3C 391*. ApJ, 467: 698, Aug. 1996. doi:10.1086/177645.

Rochester, G. D. & Butler, C. C. *Evidence for the Existence of New Unstable Elementary Particles*. Nature, 160:855–857, Dec. 1947. doi:10.1038/160855a0.

Roman-Duval, J., Jackson, J. M., Heyer, M., et al. *Kinematic Distances to Molecular Clouds Identified in the Galactic Ring Survey*. ApJ, 699:1153–1170, July 2009. arXiv:0905.0723. doi:10.1088/0004-637X/699/2/1153.

Roman-Duval, J., Jackson, J. M., Heyer, M., Rathborne, J., & Simon, R. *Physical Properties and Galactic Distribution of Molecular Clouds Identified in the Galactic Ring Survey*. ApJ, 723:492–507, Nov. 2010. arXiv:1010.2798. doi:10.1088/0004-637X/723/1/492.

Rosenblatt, M. *Remarks on Some Nonparametric Estimates of a Density Function*. The Annals of Mathematical Statistics, 27(3):832–837, 09 1956. doi:10.1214/aoms/1177728190.

Schure, K. M., Bell, A. R., O'C Drury, L., & Bykov, A. M. *Diffusive Shock Acceleration and Magnetic Field Amplification*. Space Sci. Rev., 173:491–519, Nov. 2012. arXiv:1203.1637. doi:10.1007/s11214-012-9871-7.

Seta, M., Hasegawa, T., Sakamoto, S., et al. *Detection of Shocked Molecular Gas by Full-Extent Mapping of the Supernova Remnant W44*. Astron. J, 127:1098–1116, Feb. 2004. doi:10.1086/381058.

Seward, F. D. *Einstein Observations of Galactic supernova remnants*. ApJS, 73:781–819, Aug. 1990. doi:10.1086/191489.

Skilling, J. *Cosmic ray streaming. I - Effect of Alfven waves on particles*. MNRAS, 172:557–566, Sept. 1975.

Strong, A. W., Moskalenko, I. V., & Reimer, O. *Diffuse Continuum Gamma Rays from the Galaxy*. ApJ, 537:763–784, July 2000. arXiv:astro-ph/9811296. doi:10.1086/309038.

Strong, A. W., Moskalenko, I. V., & Ptuskin, V. S. *Cosmic-Ray Propagation and Interactions in the Galaxy*. Annual Review of Nuclear and Particle Science, 57:285–327, Nov. 2007. arXiv:astro-ph/0701517. doi:10.1146/annurev.nucl.57.090506.123011.

Sturner, S. J. & Dermer, C. D. *Association of unidentified, low latitude EGRET sources with supernova remnants.* A&A, 293:L17–L20, Jan. 1995. arXiv:astro-ph/9409047.

Terrier, R. *HGPS Paper - Large-scale emission*. H.E.S.S internal documentation, 2014.

Terrier, R., Mattana, F., Djannati-Atai, A., et al. *Discovery of a pulsar wind nebula associated with IGR J18490-0000*. volume 1085 of *American Institute of Physics Conference Series*, pages 312–315, Dec. 2008. doi:10.1063/1.3076669.

Thompson, D. J., Baldini, L., & Uchiyama, Y. *Cosmic ray studies with the Fermi Gamma-ray Space Telescope Large Area Telescope*. Astroparticle Physics, 39:22–32, Dec. 2012. arXiv:1201.0988. doi:10.1016/j.astropartphys.2011.10.009.

Truelove, J. K. & McKee, C. F. *Evolution of Nonradiative Supernova Remnants*. ApJS, 120: 299–326, Feb. 1999. doi:10.1086/313176.

Uchiyama, Y., Funk, S., Katagiri, H., et al. *Fermi Large Area Telescope Discovery of GeV Gamma-Ray Emission from the Vicinity of SNR W44*. ApJ, 749:L35, Apr. 2012. arXiv:1203.3234. doi:10.1088/2041-8205/749/2/L35.

Vallée, J. P. *The Spiral Arms and Interarm Separation of the Milky Way: An Updated Statistical Study*. Astron. J, 130:569–575, Aug. 2005. doi:10.1086/431744.

Voelk, H. J. & Bernloehr, K. *Imaging Very High Energy Gamma-Ray Telescopes*. Exp. Astron., 25:173–191, 2009. arXiv:0812.4198.

Wang, Z. R. & Seward, F. D. *X-rays from the SNR 3C 391*. ApJ, 279:705–707, Apr. 1984. doi:10.1086/161935.

Weekes, T. C., Cawley, M. F., Fegan, D. J., et al. *Observation of TeV gamma rays from the Crab nebula using the atmospheric Cerenkov imaging technique*. ApJ, 342:379–395, July 1989. doi:10.1086/167599.

Welford, W. & Winston, R. *The Optics of Nonimaging Concentrators*. Academic Press, New York, 1978.

White, R. L., Becker, R. H., & Helfand, D. J. *New Catalogs of Compact Radio Sources in the Galactic Plane*. Astron. J, 130:586–596, Aug. 2005. arXiv:astro-ph/0501607. doi:10.1086/431249.

Williams, J. P., de Geus, E. J., & Blitz, L. *Determining structure in molecular clouds*. ApJ, 428: 693–712, June 1994. doi:10.1086/174279.

Wilner, D. J., Reynolds, S. P., & Moffett, D. A. *CO observations toward the supernova remnant 3C 391*. Astron. J, 115:247, Jan. 1998. doi:10.1086/300190.

Wilson, R. W., Jefferts, K. B., & Penzias, A. A. *Carbon Monoxide in the Orion Nebula*. ApJ, 161:L43, July 1970. doi:10.1086/180567.

Woltjer, L. *Supernova remnants*. ARA&A, 10:129 – 158, 1972.

Yan, H., Lazarian, A., & Schlickeiser, R. *Cosmic-Ray Streaming from Supernova Remnants and Gamma-Ray Emission from nearby Molecular Clouds*. ApJ, 745:140, Feb. 2012. arXiv:1111.2410. doi:10.1088/0004-637X/745/2/140.

# Danksagung

Ich möchte mich bei vielen Menschen bedanken, die insgesamt zu dem Gelingen meiner Doktorarbeit auf verschiedenste Weise beigetragen haben.

Zuallererst möchte ich mich bei meinem Doktorvater Prof. Dr. Christian Stegmann bedanken, ohne den die Arbeit in dieser Form nicht entstanden wäre. An dieser Stelle vielen Dank auch für die Möglichkeit meine Dissertation in der H.E.S.S. Gruppe Erlangen anzufertigen und ebenfalls hier in Erlangen fertig zu stellen, außerdem für die Freiheiten mit der ich die Schwerpunkte meiner Forschung setzen konnte.
Vielen Dank an Ira für die vielen Diskussionen, die tolle Zusammenarbeit, die vielen Telefongespäche und Treffen auch während ihrer Elternzeit. Vielen Dank auch für das Korrekturlesen meiner Arbeit.
Ein großes Danke geht an Kathrin für die wunderbare Zeit als Zimmerkolleginen, die vielen Gespräche über Arbeitszeug, aber auch über alles Mögliche und ihre Anmerkungen und Korrekturen zu meiner Arbeit und ihr immer offenes Ohr.
Herzlichen Dank an Susanne. Ohne sie wäre ich teilweise hoffnungslos an vielen LaTex Eigenheiten verzweifelt. Sie hattest irgendwie für jedes Problem immer sofort eine Lösung parat. Vielen Dank für die tolle Zeit als Zimmerkolleginen, die vielen Gespräche, wir beide jeweils hinter dem eignen Bildschirm hervorguckend, und das Korrekturlesen meiner Arbeit.
Vielen Dank an Prof. Dr. Christopher van Eldik, für die immer offene Tür für Fragen aller Art, meist der Ansprechpartner, wenn ich mal wieder wegen statistischer Methoden einen Knoten im Kopf hatte.
Vielen Dank an Anton für das schnelle Antworten zu jeglichen Problemen technnischer und programmier-technischer Natur und die Gespräche zwischen durch, vor allem in unserer Endphase.
Außderdem noch vielen Dank an Fidi, Philipp, Johannes und André für die zahlreichen Gespräche und Diskussionen jeglicher Art am Kaffetisch und jenseits davon. Ihr habt viel zu meiner Allgemeinbildung beigetragen.
Vielen Dank an Gabi für das umkomplizierte Lösen aller verwaltungtechnischen und bürokratischen Dinge.
Insgesamt einen herzlichen Dank an die gesamte H.E.S.S. Gruppe Erlangen und das ECAP für die tolle Atmosphäre.
An dieser Stelle auch ein großes Danke an meine ehemaligen Kollegen in Erlangen für die vielen Gespräche und Lösungen verschiedenster Probleme: Fabian, Bernhard, Peter (Danke für die Anmerkungen zu dem Molekülwolken-Kapitel), Sebastian, Daniel, Julia und Constanze.
Ein lieber Gruß geht auch an meine Kollegen, die von Erlangen nach Zeuthen gewechselt waren. Vor allem vielen Dank an Arnim und Anneli.

Das größte Dankeschön geht an meine Famile. Vielen Dank für euere Unterstützung und euer Vertrauen in mich.
Danke für Alles und viel mehr an meinen Lebensgefährten.